ION-INDUCED DAMAGE IN SI: A FUNDAMENTAL STUDY OF BASIC MECHANISMS OVER A WIDE RANGE OF IMPLANTATION CONDITIONS

Elaine Grannan Roth, B.S., M.S.

Dissertation Prepared for the Degree of

DOCTOR OF PHILOSOPHY

UNIVERSITY OF NORTH TEXAS

May 2006

APPROVED:

J. L. Duggan, Major Professor
F. D. McDaniel, Committee Member and Chair of the Department of Physics
D. Weathers, Committee Member and Graduate Program Coordinator
S. Matteson, Committee Member
Sandra L. Terrell, Dean of the Robert B. Toulouse School of Graduate Studies

Roth, Elaine Grannan, Ion-Induced Damage in Si: A Fundamental Study of Basic Mechanisms over a Wide Range of Implantation Conditions. Doctor of Philosophy (Physics), May 2006, 186 pp, 5 tables, 58 illustrations, references, 142 titles.

A new understanding of the damage formation mechanisms in Si is developed and investigated over an extended range of ion energy, dose, and irradiation temperature. A simple model for dealing with ion-induced damage is proposed, which is shown to be applicable over the range of implantation conditions. In particular the concept of defect "excesses" will be discussed. An excess exists in the lattice when there is a local surplus of one particular type of defect, such as an interstitial, over its complimentary defect (i.e., a vacancy). Mechanisms for producing such excesses by implantation will be discussed. The basis of this model specifies that accumulation of stable lattice damage during implantation depends upon the excess defects and not the total number of defects.

The excess defect model is validated by fundamental damage studies involving ion implantation over a range of conditions. Confirmation of the model is provided by comparing damage profiles after implantation with computer simulation results. It will be shown that transport of ions in matter (TRIM) can be used effectively to model the ion-induced damage profile, i.e. excess defect distributions, by a simple subtraction process in which the spatially correlated defects are removed, thereby simulating recombination. Classic defect studies illuminate defect interactions from concomitant implantation of high- and medium-energy Si^+-self ions.

Also, the predictive quality of the excess defect model was tested by applying the model to develop several experiments to engineer excess defect concentrations to substantially change the nature and distribution of the defects. Not only are the excess defects shown to play a

dominant role in defect-related processing issues, but their manipulation is demonstrated to be a powerful tool in tailoring the implantation process to achieve design goals. Pre-amorphization and dual implantation of different energetic ions are two primary investigative tools used in this work. Various analyses, including XTEM, RBS/channeling, PAS, and SIMS, provided experimental verification of the excess defect model disseminated within this thesis.

Copyright 2006

by

Elaine Grannan Roth

TABLE OF CONTENTS

Page

LIST OF TABLES vi

LIST OF ILLUSTRATIONS vii

LIST OF ACRONYMS xi

Chapters

1. INTRODUCTION 1

2. EXPERIMENTAL METHODS 6

   Equipment

   Analysis Techniques

      RBS

      SIMS

      XTEM

      PAS

3. HISTORICAL PERSPECTIVE 17

   History of Stopping in Solids

   Defect Models

4. NEW DAMAGE MODEL: THE ROLE OF EXCESS DEFECTS IN DEFECT-MEDIATED PROCESSES IN SI 30

   Introduction

   Use of TRIM to Determine Excess Defects

      Regions of Excess Defects

      Separation Mechanism

5. VALIDATION 48

   Damage Profiles versus Implant Temperature

   Co-implantation of High- and Medium-Energy Si^+-Self Ions below the Amorphization Threshold

      Discussion

      Co-implantation of MeV and keV Si^+-Ions into Cz-Si (100)

Fluence of 200 keV Si+-Ion Implants

Implant Temperature

Order of Implantation

Synergistic Response of Co-Implantation of MeV and keV Si^+-Ions

Defect Interactions

Reverse Order of Implants

Summation: Excess Defect Model Supported

6. PREDICTIVE NATURE OF MODEL: DEFECT ENGINEERING 87

Introduction

Experiment I: Suppression of TED of Implanted B^+

Discussion

Experiment

Results

Model Predicts EOR Interstitials–Consistent with B+ Diffusion

Implant Temperature: -50°C versus RT

Dual Implantation in SOI

Experiment II: "Front" Amorphization - Eliminating the End-of-Range Defects associated with Amorphization

Discussion

Development through Excess Defect Model

SOI versus Bulk Si

Experiment

Results

Experiment III: High-Energy Ion Implantation - Dual Implants with keV Si^+-Self Ions above the Amorphization Threshold

Background

Experiment

Results

Removal of EOR Defect Band

TED of Boron: Defect Probe

Synopsis

7. CONCLUSIONS.. 153

Appendices

A. DAMAGE EXTRACTION ROUTINE FOR RBS/CHANNELING 160

B. PHYSICS OF STOPPING CROSS SECTIONS FOR PARTICLES TRAVERSING A SOLID.. 169

REFERENCES 179

LIST OF TABLES

Page

I. Density of defects separated and converted to range in Angstroms for the final energies provided ... 42

II. Separation (SP) (Angstroms) and change in SP with respect to the final energy ... 45

III. Excess damage beyond the amorphous-crystal (a-c) interface at the respective implant temperature ... 59

IV. Implant matrix for dual implants of experiment II: co-implantation of high (1.25 MeV)- and medium (200 keV)-energy Si+-self ions below the amorphization threshold ... 64

V. Damage visible following dual implantation ... 142

LIST OF ILLUSTRATIONS

Page

1. Schematic of the Rutherford backscattering (RBS) and MeV implant beamlines in the surface modification and characterization (SMAC) research facility at Oak Ridge National Laboratory (ORNL) at the time of this research 9

2. (a) Typical RBS aligned spectrum of implanted Czochralski (Cz-) Si (100) shown with the virgin spectrum. The linear approximation and estimated curves are shown for reference (a). The hachured area in (a) denotes the damage extracted reported in (b)... 12

3. Diagram detailing the 511 keV annihilation peak from positron annihilation spectroscopy (PAS) measurements of open volume defects within implanted material and the equation used to determine the S-parameter 16

4. Total defect and implant profiles following a transport of ions in matter (TRIM) simulation of 200 keV, 10^{16} Si^{+}/cm^{2} implanted into Si 34

5. TRIM simulation of 200 keV, 10^{16} Si^{+}/cm^{2} implanted into Si detailing sources of excess defect concentrations 36

6. Dependence of energy transferred during collisions on impact parameter for TRIM simulations of 500 keV Si^{+} on Si and 5.0 MeV Ge^{+} on Si 40

7. TRIM simulations of Si^{+}(200 keV, $10^{17}/cm^{2}$) incident on Si where the final energy E_f was varied for each simulation 41

8. The separation (SP) in the Frenkel pairs was plotted versus final energy, E_f, and the data fit with a decaying exponential relationship 43

9. The change in the separation versus the final energy (E_f), $d(SP)/dE_f$, was measured versus the final energy 46

10. RBS/channeling spectra of Si implanted with 150 keV Si^{+}-ions to a fluence of $10^{14}/cm^{2}$ at liquid nitrogen (LN_2) and $10^{16}/cm^{2}$ at 300° C 50

11. TRIM simulation of 150 keV Si^{+} on Si illustrates the uncorrelated Frenkel defects and implanted Si or plus-one profiles 51

12. Damage extracted from aligned RBS profiles compared with TRIM simulations for 150 keV, 10^{14} Si^{+}/cm^{2} (a) and 10^{16} Si^{+}/cm^{2} (b) implanted at LN_2 temperature and 300° C, respectively 53

13. PAS profiles of 2 MeV, 10^{17} Si^{+}/cm^{2} implanted into silicon-on-insulator (SOI) 56

14. RBS <100> aligned spectra of end-of-range (EOR) damage following solid-phase-epitaxial-regrowth (SPER) of amorphous layers generated from implantation of As^+ into Si at LN_2, RT, 100° C, and 150° C ... 58

15. Damage from As^+ (120 keV, $5\times10^{15}/cm^2$) implanted in Si versus implant temperature compared to disorder from TRIM simulations of the implant ... 60

16. Co-implantation of 1.25 MeV and 200 keV Si^+-ions investigated to determine any dependence on the fluence of 200 keV Si^+-ions, implant temperature, and order of implantation ... 62

17. RBS/channeling spectra of Si co-implanted with 1.25 MeV and 200 keV Si^+-ions at 250° and 450° C with fluences of $5\times10^{15}/cm^2$ (a) and $1\times10^{15}/cm^2$ (b) 200 keV ions ... 67

18. RBS/channeling of 1.25 MeV, $5\times10^{16}/cm^2$ Si^+-ions implanted at 250° and 450° C ... 69

19. Damage versus implant fluence of 200 keV, Si^+-ions for the control samples with only the 200 keV implant ... 71

20. RBS/channeling spectra of samples implanted with various fluences of 200 keV Si^+-ions only at (a) 450° C and (b) 250° C ... 72

21. RBS/channeling spectra of 1.25 MeV Si^+-ions implanted with 200 keV Si^+-ions ranging in fluence from 10^{15} to $1.5\times10^{16}/cm^2$ at 450° C for different orders of implantation ... 73

22. RBS/channeling spectra of 1.25 MeV Si^+-ions implanted with 200 keV Si^+-ions ranging in fluence from 10^{14} to $10^{16}/cm^2$ at 250° C for different orders of implantation ... 74

23. Damage for the MeV/keV and control implants versus fluence of 200 keV Si^+-ions at 450° C (a) and 250° C (b) ... 75

24. Recombination mechanism for dual implanted samples with 1.25 MeV and 200 keV Si^+-ions ... 77

25. TRIM simulation of 1.25 MeV, $5\times10^{16}/cm^2$ Si^+-ions implanted into Si displaying resultant excess defect regions ... 78

26. Damage for the MeV/keV, keV/MeV, and control implants versus implanted fluence of 200 keV Si^+-ions at 450° C ... 80

27. Damage for the MeV/keV, keV/MeV, and control implants versus implanted fluence of 200 keV Si^+-ions at 250° C ... 81

28. RBS/channeling spectra of MeV ions implanted with 5 and 8×10^{15} and 1.2×10^{16} Si^+-ions/cm^2, displayed in order of decreasing fluence. Both implants were performed at 450° C ... 82

29. RBS/channeling spectra of MeV ions implanted with 3, 5, and 9×10^{15} Si^{+}- ions/cm^2, displayed in order of decreasing fluence. Both implants were performed at 250° C 83

30. TRIM simulation of 1.25 MeV, 1.4×10^{15} Si^{+}/cm^2 implanted into Si 91

31. Secondary ion mass spectrometry (SIMS) analysis of the initial profile of B^{+} (40 keV, $10^{14}/cm^2$, room temperature (RT)) implanted in crystalline and pre-amorphized Si...... 93

32. SIMS of B+ (40 keV, $10^{14}/cm^2$, RT) implanted in crystalline and preamorphized Si both prior to and following an 800° C/15 minute anneal.. 97

33. <100> channeled spectra of B^{+}-implanted into Si pre-amorphized at RT and -50° C . 101

34. SIMS profiles of B^{+}-implanted into Si preamorphized at both -50° C and RT and annealed at 800° C for 15 minutes.. 103

35. SIMS profiles of B^{+}-implanted into Si preamorphized at both -50° C and RT and annealed at 1000° C for 15 minutes.. 107

36. B^{+}-ions implanted into SOI implanted first with 2 MeV Si^{+}-ions at RT to influence B^{+}-induced interstitials to recombine with vacancy defects in the near-surface layer from the MeV implant 109

37. SIMS profiles of B^{+}-implanted into SOI following implantation of 2 MeV, 1×10^{15} Si^{+}/cm^2 and annealed at 800° C for 15 minutes.. 111

38. SIMS profiles of B^{+}-implanted into SOI following implantation of 2 MeV, 5×10^{15} Si^{+}/cm^2 and annealed at 800° C for 15 minutes.. 112

39. "Front Amorphization" experiment: preamorphize crystalline Si layer of SOI material to just below the surface.. 116

40. PAS of 2 MeV, $10^{17}/cm^2$ Si^{+} implanted into Si and annealed at 800°, 900°, and 1000° C 118

41. Pictorial representation of implants supporting front-amorphization experiment........ 121

42. RBS, <100> channeled data of the amorphous layer generated with an Si^{+}(1.25 MeV, $1.4\times10^{15}/cm^2$, LN_2) implant in SOI 122

43. SIMS analysis of 40 keV B^{+} implanted within amorphous layer where regrowth was intended from the surface. Both initial and annealed profiles are included................. 124

44. SIMS analysis of 150 keV B^{+}-ions implanted into the buried amorphous layer that regrows from the surface 126

45. Measuring synergism of dual implantation and amorphization following processing steps: 1-1.25 MeV Si^{+}-ions implanted into Si substrate; 2-amorphization of surface layer to a

depth of approximately 2500 Å; 3-introduction of dopant species encompassed within the amorphous layer; and 4-regrowth of the amorphous layer 128

46. RBS/channeling results of both the initial and 800° C annealed spectra of Si amorphized-only. The virgin and random added for reference... 131

47. RBS/channeling spectra of the initial and annealed profiles of the amorphized-only sample and dual implanted material. The random and virgin spectra added for reference 132

48. RBS/channeled spectra of 1.25 MeV, 5 and 6×10^{16} Si^+/cm^2 implanted at 100° C prior to amorphization of the surface layer with 70 and 140 keV, 1×10^{15} Si^+/cm^2 implanted at RT 134

49. Cross-sectional transmission electron microscopy (XTEM) images of Si amorphized-only and dual implanted material with 1.25 MeV, 5 and 6×10^{16} Si^+/cm^2 followed by amorphization. Samples were annealed at 800° C for 20 minutes 135

50. RBS/channeling spectra of Si implanted with 1.25 MeV Si^+-ions over a range of fluence 1 to $6\times10^{16}/cm^2$ at 100° C and amorphized 138

51. RBS/channeling spectra of Si implanted with 1.25 MeV Si^+-ions over a range of fluence 1 to $6\times10^{16}/cm^2$ at 250° C and amorphized 139

52. RBS/channeling spectra of Si implanted with 1.25 MeV Si^+-ions over a range of fluence 1 to $6\times10^{16}/cm^2$ at 450° C and amorphized 140

53. Damage from dual implants at 100°, 250°, and 450° C versus fluence of 1.25 MeV Si^+-ion implant 141

54. RBS/channeling spectra showing samples dual implanted at 100°, 250°, and 450° C with 1.25 MeV Si^+-ions to a fluence of $4\times10^{16}/cm^2$ and amorphized.................................. 143

55. PAS data of dual-implanted Cz-Si; both initial and annealed at 600° and 800° C for 20 minutes profiles.. 145

56. SIMS data of B^+ implanted into dual-implanted material 149

57. RBS/channeling spectra illustrating the different profiles generated throughout the damage extraction routine... 167

58. Damage profile extracted from RBS/channeling curve 168

LIST OF ACRONYMS

a-c...................amorphous-crystalline

B^+ ....boron ion

CM ....center-of-mass

CVD ....chemical vapor deposition

Cz-Si ....Czochralski-silicon

E_f ....final energy

EOR................end-of-range

fz-Si................float-zone silicon

IBDE ....ion beam defect engineering

IBIA ....ion beam induced annealing

IC....................integrated circuits

keV.................kilo-electron volts

LN_2.................liquid nitrogen

MeV ....million electron volts

MCA ....multi-channel analyzer

ORNL.............Oak Ridge National Laboratory

PAS ....positron annihilation spectroscopy

PTEM.............plan-view transmission electron microscopy

RBS ....Rutherford backscattering spectroscopy

R_p....................projected range

RT ....room temperature

RTA................rapid thermal annealer

Sb ....antimony

SIMOX...........separation by implantation of oxygen

SIMS ....secondary ion mass spectroscopy

SMAC ....surface modification and characterization

SNICS ....source of negative ions by cesium sputtering

SOI ....silicon-on-insulator

SOS ....silicon-on-sapphire

SP ....separation

SPEG..............solid phase epitaxial growth

SPER ....solid phase epitaxial regrowth

SRIM..............stopping and range of ions in matter

Si^+...................silicon ion

TED................transient-enhanced diffusion

TEM ....transmission electron microscopy

TRIM..............transport of ions in matter

UHV ....ultra-high vacuum

VBA ....visual basic for applications

VLSI...............very large scale integration

XTEM ....cross-sectional transmission electron microscopy

CHAPTER 1

INTRODUCTION

Ion implantation is a simple process for injecting energetic ions into a sample with energy sufficient to penetrate below the surface. As such, implantation can be used to introduce controlled amounts of impurities in the sample's near-surface. The ion beam is normally magnetically analyzed to ensure mass and energy selectivity.[1] In addition, the beam is raster-scanned over the implanted area to provide a uniform or homogeneous irradiation of the sample. Since the charge of the ions allows accurate integration of the implanted current, the areal fluence (i.e., the number of ions implanted within a unit of area) can be determined and reproduced with great accuracy. The ability to accurately control the number of implanted ions within a selected area makes ion implantation an indispensable tool in the field of microelectronics[2] where it is used almost exclusively in the fabrication of integrated circuits (IC's) to form electrical junctions.

When ion implantation processing was initially implemented in the microelectronics industry, the depth of the electrical junctions was sufficiently large that the residual damage near the ions' end-of-range (EOR) did not adversely affect device operation.[3] The EOR is where the ions ultimately come to rest after being implanted. Hence, the EOR is slightly deeper than the projected range, R_p, of the implanted dopant. Since the implanted dopants were driven deep within the samples by long thermal diffusion cycles, junction depths formed well beyond the EOR depth. However, the evolution of design rules has resulted in substantial shrinking of device parameters so that little or no drive-in of the as-implanted dopant profile can now be tolerated. Thus, thermal activation of the implanted dopants and annealing of the ion-induced damage

must now be achieved with little or no movement of the as-implanted profile. This challenge has met with substantial difficulty due to a phenomenon known as transient enhanced diffusion (TED).[4] A broadening of the implanted and annealed dopant profile can result during the early stages of annealing, where the depth of the profiles can not be explained by range theory or equilibrium diffusion processes. This enhanced broadening diminishes over time, returning the rate of diffusion to thermal equilibrium values, and thus it was labeled as transient diffusion. The diffusivity of dopants such as boron can be greatly enhanced by orders of magnitude due to the presence of ion-induced defects within the irradiated volume. These defects participate in the diffusion process until their numbers are reduced to equilibrium values. Under equilibrium or non-equilibrium conditions, the diffusion coefficient D consists of the sum of contributions of the form

$$D_i = \frac{C_i d_i}{C_X} \qquad [1.1.1]$$

where C_i is the concentration of the defect i with corresponding diffusivity d_i, and C_X is the total concentration of impurities.[5] After a sufficient time interval, dynamical local equilibrium results between the actual point defect concentrations, C_I (interstitial-defect concentration) and C_V (vacancy-defect concentration), and their thermal equilibrium concentrations.[6] Thus, it has become necessary to identify and control ion-induced defects and their interactions during the implantation process as well as the subsequent, thermal activation cycle to eliminate or suppress TED effects. This requires a more detailed understanding of these phenomena as well as engineering techniques to control their effects.[3]

It is well known that irradiating a material with energetic ions results in the

formation of lattice defects.[7] Subsequent thermal treatment is necessary both to activate the implanted dopants and to anneal the ion-induced defects.[7] Thermal annealing of defects is not perfect and can lead to the formation of many metastable defect structures as a result of point defect migration and clustering.[7,8] Extended defects, e.g., threading dislocations and/or loops can be formed by this process and are stable to higher temperatures.[8] The nature of the ion-solid interactions depends upon a variety of parameters, e.g., the incident energy of the ion; the temperature at which the ions are introduced into the lattice; the flux or dose-rate; the atomic number and mass of the incident ion; and, finally, the implanted fluence.[2,9] All of these implant parameters will influence the as-implanted dopant and defect profile as well as the defect structure. Understanding the mechanisms by which these ions interact with the atoms in the solid and/or other defects as a function of the various implantation conditions is essential in developing techniques to manage defect processes to control or eliminate their adverse effects on electrical properties within the active device regions.

Decades of research have been devoted to the study of defects in Si resulting from ion bombardment and the mechanisms by which the ions interact with other defects and impurities.[10,11,12,8,13,14,15,16,17,18,19,20,21,22] A number of models have emerged which attempt to provide explanations as to what occurs during and directly following the implant process.[12,13,17,18,23] Simulation codes such as transport of ions in matter (TRIM)[24] are available that provide very accurate treatment of the various interactions that occur during the stopping of energetic ions in solids. This routine provides a detailed accounting of the ion-atom interaction including nuclear and electronic energy loss, as well as the partitioning of nuclear loss into phonon and defect creation. Despite the

accuracy of such routines, they are limited in that they only treat the immediate process associated with the passage of the ion in the solid and not the subsequent thermal relaxation process involving the interaction of the ion-induced defects with the lattice. These interactions can include loss of defects at sinks such as the surface, recombination, and defect clustering to form metastable damage.[7] All of these processes depend upon the material properties as well as the implantation parameters. While it is obvious that the ion mass and energy will substantially affect these processes, it has also been demonstrated that the implantation temperature and flux [i.e., the ion current] can also have a large effect upon the amount of residual damage.[25,26,27]

Despite the complexity of the ion-induced defects and their interactions, an attempt is made, in the present work, to simplify the treatment of damage formation by identifying a limited number of basic defect processes that are dominant. This not only will help in understanding ion-induced damage formation but also in devising defect engineering approaches for moderating the deleterious effects of defects. To this end, ion implantation was investigated under extreme conditions, i.e., of high-temperature, -energy, and -dose. While certain applications such as ion beam synthesis and ion cutting provide a motivation to study such extreme irradiation conditions, it will be shown that such a study provides much insight into basic mechanisms of damage formation over a much wider range of conditions. Existing damage models will be identified and discussed, in particular the limitations of these models in anticipating ion interactions at these extreme implant conditions.

A “new” model to account for damage formation during ion implantation under extreme irradiation conditions will be presented. This new model is investigated and its

range of application is examined. Successful modeling for the purpose of predicting resulting implant damage is both necessary and useful for researchers and manufacturers. This information enables engineers, researchers, and others to better predict the outcome of ion processes, as well as develop novel techniques such as defect engineering, or the practice of altering or adapting implant schedules to generate a desired result.[28] Several different defect-engineering solutions based upon this 'new' model are presented. These engineered solutions not only provide validation of the model but clearly demonstrate the ability to circumvent problems such as TED by proper management of the ion-induced defects and their interactions.

CHAPTER 2

EXPERIMENTAL METHODS

Equipment

This work was performed in the surface modification and characterization (SMAC) research center at Oak Ridge National Laboratory (ORNL) in Oak Ridge, Tennessee. At the time of this study, the SMAC research center was a user facility that supported research on university, industrial, and government levels. The SMAC facility contained four accelerators: A 2.5 MeV van de Graaff, an Eaton Nova implanter, a 1.7 MeV Tandetron Tandem accelerator, and a Varian Extrion implanter. The 2.5 MeV van de Graaff accelerator is a single ended machine. It produces He^+ and H^+ beams and has two beam ports. One was devoted entirely to Rutherford backscattering spectrometry (RBS)/channeling analyses and the second was used for surface analysis techniques. The 1.7 MeV Tandetron tandem had two functioning beam lines. Two sources were available on the tandem accelerator, the Alphatross and SNICS [source of negative ions by cesium sputtering]. The Alphatross creates plasmas from any gaseous source, but is primarily used for producing a He^--ion beam, which is stripped to He^+ or He^{++} for RBS/channeling measurements. The SNICS ion source may produce a variety of ion beams. The cesium ion, Cs^+, beam bombards a pellet containing the desired element to generate negative ions accelerated, stripped to positive charge states, and delivered to the appropriate end chamber.

I performed low-energy implants with either the Extrion or Eaton Nova. The Extrion operated at voltages between 30 kV and 180 kV. The Eaton Nova was capable of a broader energy range: 5-700 kV. Both implant machines were reliable, reproducible,

and accurate, producing multiple ion beams at different charge states and energies. Both machines utilized magnetic mass analysis to select the desired beam prior to the beam focusing elements. The beam was then raster scanned to ensure uniform coverage of the beam over the target area.

Annealing was done in standard quartz-tube furnaces. A variety of implanted material was annealed within these furnaces. Concern for contamination of the samples in the general-use furnace drove the development of a furnace intended for Si samples only, identified as the Si-only furnace. The Si-only furnace was assembled by a fellow graduate student and me. This Si-only furnace was also a quartz-tube furnace that connected to a cross. Both roughing and turbo pumps were attached to the Si-only furnace making vacuum as well as ambient anneals possible. The maximum possible temperature was 1200° C for both quartz-tube furnaces, imposed by the limitations of the quartz tube. The annealing temperature was kept at 1000° C and below, so there was no concern of impurities from the quartz tube contaminating the implanted material during the annealing process.

Analysis Techniques

I used many analysis techniques including RBS/channeling, positron annihilation spectroscopy (PAS), secondary ion mass spectrometry (SIMS), and cross-sectional transmission electron microscopy (XTEM), to characterize and quantify the implant damage.

Rutherford backscattering (RBS)/channeling

RBS analysis is a powerful, non-destructive analytical tool. Although it is both quick and simple, it yields a multitude of information including the composition and

structure of materials. The minimum equipment necessary to accomplish RBS/channeling measurements includes an accelerator to produce the energetic ion beam; transport beam line; and a target chamber with a sample manipulator, detector, and signal processor. The beam used for analysis consists primarily of protons or helium ions. Throughout this thesis, 2.3 MeV He^{++}-ions were used for RBS/channeling analyses. These RBS measurements were done on the Tandetron accelerator's 30° beamline. See Figure 1, described below.

The analytical capability of RBS is enhanced by utilizing ion channeling during the measurement. In ion channeling measurements, the ions are directed upon a single crystal along a major crystallographic direction as compared to a random direction during standard RBS measurements. Prior to being backscattered, incident ions are steered preferentially into the interstices of the lattice by a series of correlated small-angle collisions with the target atoms. Therefore, the channeled ions preferentially probe the interstices of the crystal and are sensitive to the location of impurity atoms. Furthermore, the redistribution of the ion flux provides RBS with structure-sensitive capabilities useful for probing defects and lattice strain. The technique of ion channeling has been widely adopted by material scientists for the exploration of damage resulting from ion implantation.

The only hardware needed to perform channeled-ion measurements is the addition of a sample manipulator at the target chamber so the sample can be accurately positioned. The sample manipulator or goniometer utilized in these experiments provided two-dimensional manipulation of the sample in the axial and azimuth directions. The system in figure 1 displays the system within the SMAC research facility utilized, for RBS

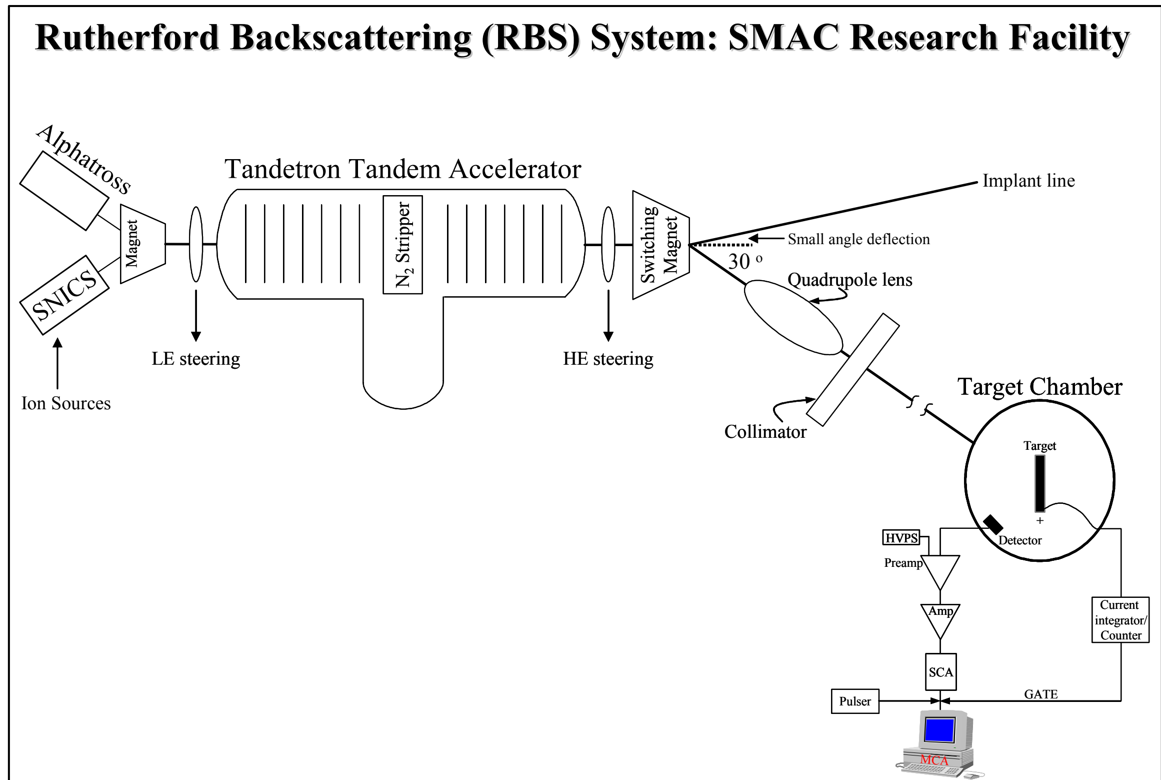

Figure 1. RBS system consisted of a 1.75 MV Tandetron tandem accelerator, a switching magnet, and an Alphatross ion source. A transport line positioned following the switching magnet contains steering elements and delivers the beam to an end target chamber. RBS analysis was performed within the target chamber with the electronic components shown.

measurements and is a typical setup of components necessary to perform RBS/channeling analyses.

Incident ions backscattered from the target surface or some depth below the surface are intercepted by a surface barrier detector and, the resultant signals were sent to a multi-channel analyzer (MCA). The spectrum is calibrated and the yield or counts in specific channels are correlated to backscattered energy and depth. A rise in the backscattered yield above the level in a virgin or unimplanted Si crystal indicates the presence of displaced atoms, i.e., interstitial-type defects. This increase in the backscattered yield from the damaged regions is due to atoms within the interstices of the crystal interacting with the channeled ions more strongly than those on substitutional lattice sites.[29]

A measurement of the total damage resulting from the implants was extracted from RBS/channeling spectra utilizing a routine that estimates ion-implanted damage by subtracting a calculated, dechanneled fraction from the original RBS profile.[29,30] The normalized scattering yield may be interpreted as

$$\left(1-\chi_R(x)\right)\frac{N_d(x)}{N} \qquad [2.2.1]$$

where $\left(1-\chi_R(x)\right)$ is the channeled fraction and $N_d(x)$ is the damage distribution, and both are measurable parameters.[30] N is the bulk density in atoms/cm^3. The total normalized yield, $\chi_T(x)$, contains two components: incident ions directly scattered by implant damage, $\left(1-\chi_R(x)\right)$, and the scattering from the random component, $\chi_R(x)$. Thus, the total yield may be written as

$$\chi_T(x)=\left(1-\chi_R(x)\right)\frac{N_d(x)}{N}+\chi_R(x) \qquad [2.2.2]$$

The above equation may be solved for either $N_d(x)$ or $\chi_R(x)$, depending on given or known information. The above equation, [2.2.2], has been solved for $N_d(x)$ below,

$$N_d(x) = N\frac{\left(\chi_T(x) - \chi_R(x)\right)}{\left(1 - \chi_R(x)\right)} \qquad [2.2.3]$$

Certain assumptions and limitations have been applied to formulate an extraction routine to provide a better approximation of lattice damage following ion implantation.[29,30] For the purposes of data analysis within this thesis, an adaptation of the extraction routine was developed in Visual Basic for Applications (VBA). This routine is discussed more fully in appendix I. A straight-line was interpolated from the $\chi_{\min}$ to a point just below the damage curve of the implanted sample. An example of the straight-line may be seen in Figure 2a. Recall, $\chi_{\min}$ refers to the lowest yield in the aligned spectrum immediately beyond the surface peak. From this straight line, $N_d(x)$ is calculated. A reiterative cycle of calculations was employed where the calculated $N_d(x)$ from the straight-line approximation was used to generate an improved value for $\chi_R(x)$. This estimated value of $\chi_R(x)$ is then figured from the actual damage distribution. A more accurate value of $N_d(x)$ is calculated and the reiterative process continued until $N_d(x)$ approaches a stationary value.[30] The dechanneled profile is shown in figure 2a as the background trace (•), along with the RBS profile of the implanted Si (-) and the straight-line approximation. The resulting damage profile (hachured area in fig. 2a) was plotted in figure 2b for damage concentration versus depth, and was integrated, yielding an areal density of damage.

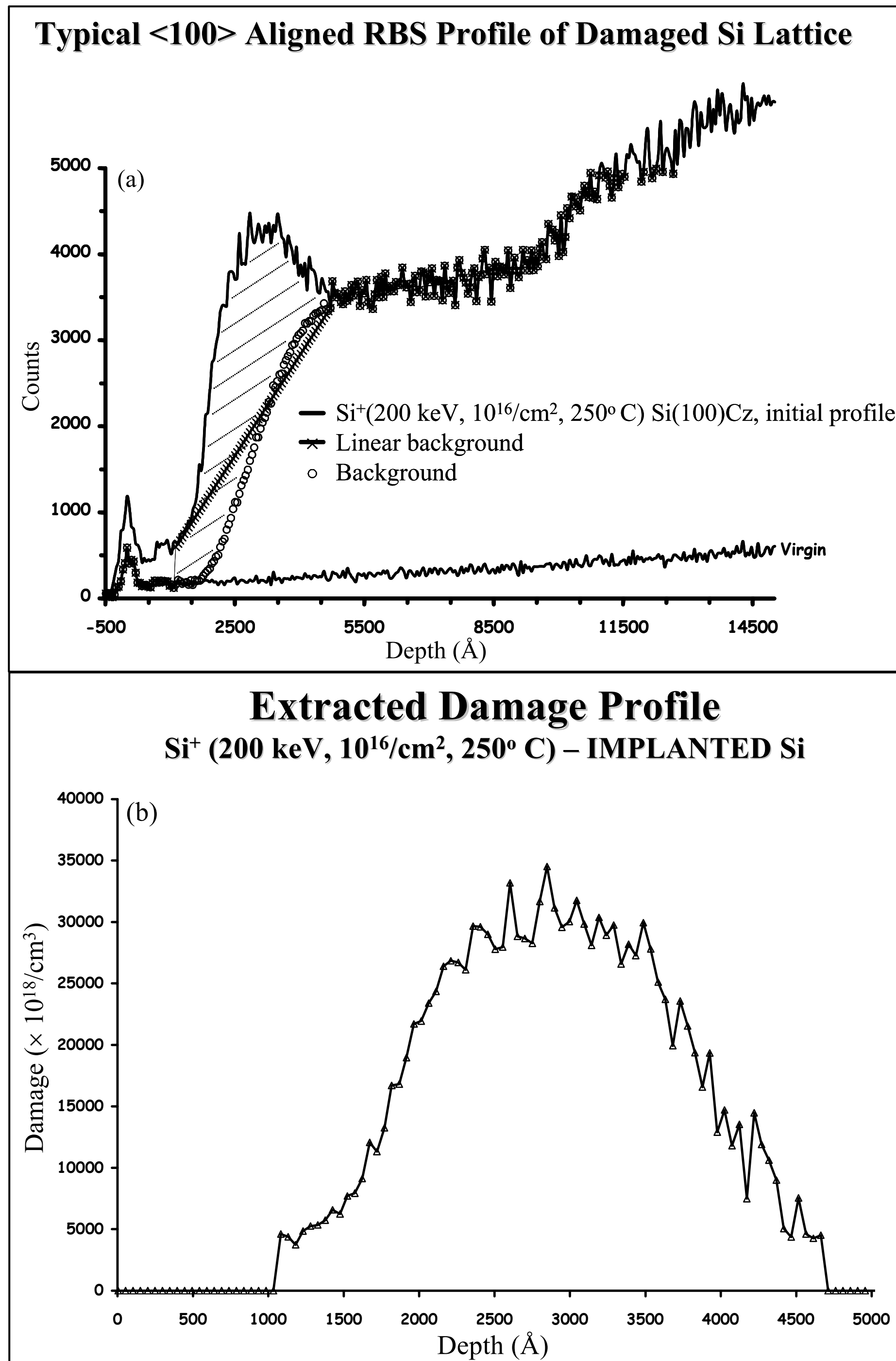

Figure 2. (a) RBS, channeling profile of damage from implantation of 200 keV, $10^{16}/cm^2$ Si^+-ions into Cz-Si(100) at 250° C. The background illustrating the calculated, dechanneled fraction and the original linear background trace are included. (b) The damage profile extracted from the RBS/channeled spectrum (the hachured area).

Secondary ion mass spectrometry (SIMS)

SIMS is an analytical tool for the compositional analysis of a material. The SIMS analysis was contracted to Charles Evans and Associates.[31] The analyses were conducted on a SIMS machine, using an O^+ beam for initial bombardment of the target. While this technique is not sensitive to lattice damage, the determination of the dopant profiles following ion implantation allows an indirect characterization of excess defects. For example, boron implantation is extremely useful as a probe of excess interstitials because boron is an interstitial diffuser.[32,33] Any movement of the boron profile either immediately following the implantation process, or during the first stages of annealing is an indication of the presence of interstitial defects.

Cross-section transmission electron microscopy (XTEM)

XTEM offers three dimensional information, necessary for a complete understanding of various damage forms resultant from ion implantation. Structural characterization of the different forms of extended damage is only possible through transmission electron microscopy (TEM). Defect structures may be investigated by either XTEM or plan-view transmission electron microscopy (PTEM). XTEM determines the depth and morphology of defect layers, while PTEM is used to study defect evolution during different processing stages and extract quantitative information on the number of point defects within extended defects and defect clusters. Studying the evolution of defects provides insight into the source and evolution of excess defects in implanted silicon.

Information from XTEM is obtained from sample regions that have been thinned to transmit electrons. Wafers were diced on a high-speed dicing saw and then glued

together with a polymer adhesive so the surfaces of interest were in contact with each other. The samples were mechanically polished on both sides by a succession of numbered sandpaper. Samples were then attached to a copper ring and ion milled to produce a hole in the middle of the sample. This procedure thins the sample sufficiently to render the defects visible within the implant volume. The samples were subsequently examined in cross section using a Phillips EM400T transmission electron microscope operated at 100 kV.

Positron annihilation spectroscopy (PAS)

PAS provides a direct measure of open volume or vacancy-type defects in ion implanted material. No other analysis methods are currently able to unambiguously identify these open volume defects. Voids can be detected by XTEM, but they must consist of >10 vacancies before they can be imaged.[8] RBS or XTEM techniques are traditionally employed to detect interstitial-type defects and damage. PAS greatly extends these capabilities not only by providing for the direct detection of open volume defects, but also by measuring their size and chemical environment.[34]

A positron measurement system consists of a positron source and energy filter to produce a monoenergetic positron beam[34], which is transported through an ultra-high vacuum (UHV) beamline and into UHV target chamber. The samples are mounted on a target holder for irradiation with the positron beam.

In PAS, incident positrons bombard the sample, where they are thermalized and then annihilated by electrons. Two gamma rays, each of 511 keV energy, which corresponds to the rest mass of an electron and the positron, are produced upon annihilation and are nearly collinear due to the conservation of momentum. Positrons

annihilating with electrons with nonzero momentum will be Doppler-shifted from 511 keV; hence, annihilations with low-momentum valence electrons produces only a minimal shift in the peak energy. At a vacant lattice site, the overlap of the positron wave function with the more energetic core electrons surrounding this site results in a significant reduction in the Doppler broadening of the annihilation radiation.

Lattice defects are thus revealed by positron analysis through measurement of the Doppler broadening of the 511 keV photon annihilation peak.[34] Specifically, this is done by extracting an S-parameter, which is determined by dividing the area of a fixed region centered on the annihilation peak, I_W, by the total peak area, I_T. Figure 3 pictorially represents the definition of the S-parameter defined in equation [2.2.4] below.

$$S = \frac{I_W}{I_T} \qquad [2.2.4]$$

A narrower annihilation peak results when positrons are trapped in open-volume spaces and prevented from interacting with high-momentum, inner-shell electrons, resulting in a greater S-parameter. The S-parameter is normalized so that its value in defect-free silicon is one (1). Any increase in the S-parameter thus reflects the presence of open volume defects. Note that an S-parameter less than one indicates the presence of oxygen-vacancy (V_nO) complexes, where n is the number of vacancies within the oxygen-vacancy cluster. O is known to cluster with vacancy defects and lead to a decrease in the S-parameter.[35]

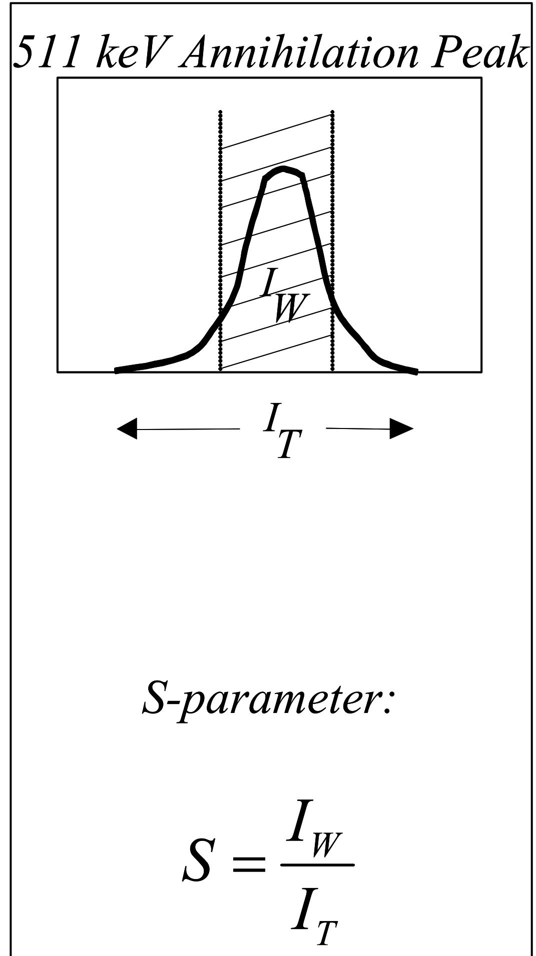

Figure 3. Diagram of the 511 keV annihilation peak from PAS analysis of open volume defects and the equation used to determine the S-parameter.

CHAPTER 3

HISTORICAL PERSPECTIVE

History of stopping in solids

The discovery in the 1890's of particle emission from radioactive material led to a keen interest in how particles were slowed while traversing matter. Significant progress toward an accurate theory of energy-loss was limited without an exact model of the atom. In 1911, Rutherford[36] demonstrated that an accurate model of the atom consisted of a positive core localized within the atom. This was followed by the works of J. J. Thomson[37] and Niels Bohr[38], who both published an analysis of this energy-loss phenomenon within one year of one another, both concluding the particle velocity was of greater importance than its energy. However, J. J. Thomson failed to include Rutherford's discovery of the positive core in his theory. Bohr's work was the first attempt at a unified theory of stopping. Bohr's original report suggested the energy loss of ions in matter can be treated by dividing it into two separate and independent processes: Nuclear stopping arising from interactions of the ions with the positive nucleus of the atom, and electronic stopping or energy loss due to interactions with the target electrons. An accurate calculation of energy loss was, however, not possible due to the limited knowledge of the effective charge of the ion in the target medium.

With the development of quantum mechanics in the 1920's, Bethe[39,40,41] and Bloch[42,43] restated the energy loss problem within a quantum scattering context. They derived fundamental equations for the stopping of very fast particles in a quantized medium using the Born approximation.[44] Their treatment remains the basis for calculating stopping cross-sections for light, fast particles with velocities in the range of

10 MeV/amu to 2 GeV/amu. The velocity range of application is limited since projectiles below this velocity may not be fully stripped of electrons, as assumed by their theory and at greater velocities relativistic corrections are necessary.

The discovery of nuclear fission in the late 1930's brought renewed interest in energy loss of ions in matter. The stopping of fission fragments in matter depended upon the amount of ionization of the fragments. This was referred to as the effective-charge problem for it was thought that, if the degree of ionization for the projectile could be estimated, stopping power theories might be employed. Bohr[45,46] assumed the incident ion would be stripped of all electrons provided the velocity of the electrons was lower than the velocity of the incident particle. Using the Thomas-Fermi model of the atom, Bohr showed the effective charge could be expressed as

$$Z_1^* = Z_1^{1/3} \frac{V}{V_o}, \qquad [3.1.1]$$

where Z_1 is the atomic number of the incident particle, V is the ion velocity, and V_o is the Bohr velocity. Polarization of the target medium by the ionic charge was first suggested by Swann[47], and Fermi reduced the challenging problem to a calculable form. A detailed suggestion for scaling stopping powers by Knipp and Teller[48] followed. The effective charge concept of Bohr[45] and Lamb[49] was employed to scale H stopping values to equivalent He ion stopping powers. Limited success was achieved in treating the stopping of partially stripped heavy ions, such as fission fragments, by these theoretical efforts.

Further progress occurred in the 1950's in the theoretical treatment of both the nuclear and electronic stopping components of the energy loss mechanism. Efforts included the treatment of the electrons in a solid as a free electron gas, in calculating the

energy loss of a particle. The particle's interaction with an electron plasma was extended by Bethe[39,40] and Bloch[42,43] to both a quantized plasma and Thomas-Fermi atoms. Fermi considered the ion-induced polarization of a classical electron medium within a target and its effect on the particle/plasma interaction. Fermi and Teller[50] extended this treatment to a degenerate free electron gas. Fermi and Teller found energy loss to be directly proportional to a particle's velocity, for slow moving particles. A full treatment of a charged particle moving within quantized electron plasma was reported approximately at the same time by Lindhard[51], Neufeld and Ritchie[52], and Fano[53]. However, the Lindhard approach concentrates on only non-relativistic particles interacting with a free-electron gas. At the present time, Lindhard's approach is widely used as the basis for calculating the electronic stopping of ions in matter.[54]

Nuclear stopping or the energy loss a particle experiences during nuclear scattering depends upon the screened Coulombic collisions between two colliding atoms. Bohr summarized much of the early work in ref. 55 which used the Thomas-Fermi model to estimate the screened Coulomb potential between atoms to be

$$V(r) = \left(Z_1 Z_2 \frac{e^2}{r} \right) \exp\left(\frac{-r}{a}\right), \qquad [3.1.2]$$

where Z_1 and Z_2 are atomic numbers for the incident and target atoms, respectively, r is their separation, and a is a "screening parameter". The selection of the screening parameter, and ultimately the screening function is very important for obtaining accurate scattering results. Upon identification of the screening parameter, the classical scattering between two colliding atoms may be determined and the energy transfer calculated. Bohr[55], without derivation, gave an expression for the screening parameter as

$a = \frac{a_o}{(Z_1^{2/3} + Z_2^{2/3})^{1/2}}$, with a_o as the Bohr radius. Firsov[56,57], using numerical techniques, derived the interatomic potentials of two colliding Thomas-Fermi atoms. Fitting these potentials with the Thomas-Fermi screening length, Firsov found the screening parameter that gave the best fit to these results to be $a = \frac{a_o}{(Z_1^{1/3} + Z_2^{1/3})^{2/3}}$.

Northcliffe[58] furthered clarified the effective charge problem by scaling a wide variety of experimental data by dividing the experimental data from each ion/target/energy combination by the stopping power of protons in the same target, at the same velocity. Northcliffe found that a significant amount of data could be accurately described with the relation:

$$\frac{Z^*}{Z} = 1 - a \exp\left[\frac{b}{Z^{2/3}} \cdot \frac{v}{v_o}\right], \qquad [3.1.3]$$

where a and b are fitting constants. By the end of the 1950's, most issues relating to energy loss had been resolved except for a first-principles treatment of effective charge, and the use of a more realistic Hartree-Fock atomic model versus a statistical approach.

As technological applications of ion implantation proliferated in the 1960's and the use of ion beams for material analysis, a more unified energy loss theory of ions in matter was realized. The first complete approach to stopping and range theory was offered by Lindhard, Scharff, and Schiott[59], referred to as the LSS-theory. Stopping and range distributions could be made within a single model. In the 1960's and 1970's, application of numerical methods to traditional theoretical approaches enabled the removal of some approximations used previously. The use of computers allowed more realistic Hartree-Fock atoms to be considered, yielding further improvements. Important

achievements in electronic stopping were made by Rousseau, Chu, and Powers[60], and Wilson, Haggmark, and Biersack[61] contributed significantly to nuclear stopping.

One final theoretical improvement was made by Brandt and Kitagawa[62] in their consideration of the degree of ionization of energetic ions in solids. Recall, Bohr had initially suggested that an ion's electrons would be stripped if the electron's velocity was lower than the velocity of the ion. Brandt and Kitagawa alternatively suggested the stripping criteria be based on the ion's electron velocity in relation to the Fermi velocity of the solid. They developed a complete formalism to validate this concept.

Current calculation of stopping powers shows an accuracy within 6% for heavy ions and better than 2% for high velocity light ions. This allows range distributions in amorphous targets to be calculated to within the same accuracy.[54] Monte Carlo-type simulation methods have emerged for accurately determining the range of heavy ions in solids by incorporating realistic treatments of both elastic and inelastic scattering, even in compound and layered targets. Numerical calculations depend upon tracking and recording the trajectories of many energetic ions. Energy and angular distributions are easily calculated by the Monte Carlo method. Many approximations may be eliminated if Monte Carol calculations are employed, but the limiting factors remain computational considerations: Computing efficiency to acquire adequate statistics and the memory size of the computer. All of the interaction details of the target must be maintained for accurate and complete simulations. Monte Carlo calculations are generally based on LSS theory, and many researchers have investigated ion transport using the Monte Carlo method.[24,63,64,65] Differences among these studies, in general, depend upon their treatment of the structure of the target, i.e., single crystal versus amorphous, and

approximations used in calculating electronic and nuclear scattering.[9]

Very large scale integration (VLSI) simulation codes exist that calculate ion implantation distributions, but employ fitted curves to experimental data, and thus, are only as accurate as the experimental data. For a most complete perspective, a few of those models will be mentioned. Other computation models, MARLOWE[63,65], UT-MARLOWE[66], and CRYSTAL-TRIM[67], model implantation in crystal structures. ATHENA[68] models channeling implantation plus damage accumulation within crystalline Si. The Monte Carlo models were based on PEPPER[69] in ATHENA, however, new models based on CRYSTAL operating with the BCA (binary collision approximation) were implemented. The BCA calculates the deflection of trajectories of moving particles with a strict binary approach between the moving atom and the closest atom in the lattice. MARLOWE[63,65] does contain a rigorous treatment of channeling. However, the performance of these simulations requires a mainframe computer.[70] Unfortunately, discrepancies in depth profiles between different research groups occasionally will result and are primarily due to implant geometry, quality of the target surface, and depth profile measurements.

Transport of ions in matter (TRIM) is a computer simulation routine based on Monte Carlo calculations that emerged from the work of Biersack and Haggmark[24]. Similar to many simulation routines, TRIM tracks a large number of individual ions and their paths or particle histories in a target. The code starts with ions of a particular energy, position and direction. Particles will change direction after binary nuclear collisions. Ions penetrate matter in straight free-flight-paths between collisions. The energy of an incident particle is reduced in early collisions due to nuclear (elastic) and electronic (inelastic)

energy loss. Inelastic energy loss due to nuclear reactions is not treated within TRIM simulations. Nuclear and electronic energy losses are considered independently. This means that incident particles lose energy in discreet amounts within nuclear collisions and continuously through electronic interactions. This separation of the energy loss into two separate components neglects any correlation between nuclear collisions and energy loss attributed to large electronic excitation. It is assumed that when the effects of many collisions are averaged, any correlation becomes negligible.[71] This correlation may become important for single scattering studies[72] and very thin targets.[73,74]

The nuclear component of stopping powers within TRIM is treated with the following transfer of energy and scattering parameters. The energy transferred in the center-of-mass (CM) coordinate system has a $\sin^2\frac{\theta}{2}$ dependence on the scattering angle, θ, and is contained in equation [3.1.4],

$$T = \frac{4M_1M_2}{(M_1+M_2)^2}E_o\sin^2\frac{\theta}{2} = \frac{4E_CM_C}{M_2}\sin^2\frac{\theta}{2} \qquad [3.1.4]$$

where M_1 and M_2 are the masses of atoms and $M_C = \frac{M_1M_2}{(M_1+M_2)}$ is the reduced mass defined in CM coordinates. The right hand side of equation [3.1.4] for the energy transferred follows from the substitution of the initial kinetic energy in the CM coordinate system, given by;

$$E_C = \frac{1}{2}M_Cv_o^2. \qquad [3.1.5]$$

Note that the scattering angle, θ, in CM coordinates is related to the laboratory frame through;

$$\vartheta = \arctan\left[\frac{\sin\theta}{(\cos\theta + \frac{M_1}{M_2})}\right] \quad [3.1.6]$$

Many statistical approaches to the interatomic interaction have been applied to calculate the nuclear stopping. The Sommerfield approximation to the Thomas-Fermi potential[75], the Moliere approximation[76], the Lenz-Jensen[77], and the Bohr potential[55] remain the most well known of these statistical models. The interatomic potential consists of a Coulombic term $\frac{1}{r}$ multiplied by a "screening" function, Φ. For two-atom collisions, the potential is found in equation [3.1.7],

$$V(r) = \left(\frac{Z_1 Z_2 e^2}{r}\right)\Phi \quad [3.1.7]$$

The Coulombic term represents the positive point nucleus and the electronic screening reduces its value for all atomic radii. The search for an accurate interatomic potential has extended over 80 years and is reviewed in ref. 78. A good interatomic potential may be calculated using a universal screening potential, given by;

$$\Phi_{Universal} = .1818e^{-3.2x} + .5099e^{-.9423x} + .2802e^{-.4028x} + .02817e^{-.2016x}, \quad [3.1.8]$$

where $x = \frac{r}{a_u}$ and reduced radial coordinate $a_u = \frac{.8854a_o}{(Z^{2/3} + Z^{2/3})}$.[78] In fact, combining computer efficiencies with the application of the universal screening potential (in equation [3.1.8]) for low energies, maintains the accuracy of MARLOWE[63] and reduces computation time by one order of magnitude.[70] This universal screening potential is an improvement over the Moliere approximation[76] to the Thomas-Fermi potential found by Wilson, et al.[61] in 1977 and to be more suitable for nuclear stopping than treatments by

Bohr[55] or Sommerfield[75]. The original paper for the simulation of ion transport, TRIM, by Biersack and Haggmark[24] applied the Moliere approximation for nuclear stopping and energy loss at low energies.

An accurate universal screening potential has been identified, as defined in equation [3.1.7], with the screening function is found in equation [3.1.8]. In order to assess the scattering angle collectively and independent of ion, target parameters; impact parameter, p; or individual atomic variables, Z_1, Z_2, M_1, and M_2, the equation for the scattering angle, θ, is converted to equation [3.1.9]:

$$\theta = \pi - 2\int_{r_o/a}^{\infty} \frac{b\,dx}{x^2\left[1 - \frac{\Phi(x)}{x\varepsilon} - \left(\frac{b}{x}\right)^2\right]^{1/2}}, \qquad [3.1.9]$$

with substitutions of $x = \frac{r}{a}$, $b = \frac{p}{a}$, $\varepsilon = \frac{E_C}{\left(Z_1 Z_2 e^2 / a\right)}$, and $V(r) = \left(\frac{Z_1 Z_2 e^2}{r}\right)\Phi\left(r/a\right)$.

Biersack and Haggmark[24] employed a fitting procedure to figure the scattering angle, which drastically increased computing efficiency of simulations, while maintaining a high degree of accuracy in determining the range of incident ions, damage distributions, and angular and energy distributions of backscattered and transmitted ions. The value of the scattering integral is obtained by numerical integration, and by fitting an analytic function containing five parameters.[24] This expression, found in equation [3.1.10], for the scattering integral is referred to as the “magic scattering” formula.

$$\cos\frac{\theta}{2} = \frac{B + R_C + \Delta}{R_o + R_C}, \qquad [3.1.10]$$

where $B = \frac{P}{a}$, $R_o = \frac{r_o}{a}$, $R_C = \frac{\rho}{a}$, and $\Delta = \frac{\delta}{a}$. P is the impact parameter, r_o is the

distance of closest approach, ρ is the addition of the radii of curvature, ρ_1 and ρ_2, δ is the addition of two correction terms, δ_1 and δ_2, and finally, $a = \frac{0.8853 a_o}{\left(Z_1^{1/2} + Z_2^{1/2}\right)^{2/3}}$ is Firsov's[79] screening length. The method of evaluating the scattering integral is critically important in enhancing the computer efficiency.

The electronic stopping component is figured for high and low energy regions, then employs an interpolation scheme proposed by Biersack[80,81]

$$S_e = \left(S_L^{-1} + S_B^{-1}\right)^{-1}, \qquad [3.1.11]$$

where S_L is the electronic stopping cross section for low energies and S_B is the modified Bethe-Bloch electronic stopping, for a realistically smooth transition. Other details of the physics of nuclear and electronic stopping may be found in appendix II.

The collision history of an ion is terminated when the ion leaves the surface of the target (as a result of backscattering), transverses the target, or is stopped within the target, i.e. the energy of the recoil drops below a preset lower limit. Any residual energy below this preset limit is partitioned to phonon processes. TRIM[24] considers the position of lattice atoms to be arranged randomly but constrained by the density of the solid. Thus, directional properties associated with the crystalline lattices are ignored. Finally, the applicable energy range of TRIM is .1 keV to 2 GeV/amu. The lower limit is established due to the failure of the binary approximation while the upper limit is established by the neglect of high order relativistic effects.

TRIM[24] has been embraced universally by researchers to obtain accurate stopping and ranges of ions in solids, understand defect distributions following ion bombardment

of a target mandated by the user, and to acquire energy and angular distributions of transmitted and backscattered particles. Other features offered by TRIM include stopping and restarting the ion penetration profile in the middle of a simulation if necessary. TRIM undergoes updates approximately every five years to correct any bugs, and is now referred to as SRIM[82] or the stopping and range of ions in matter due to the incorporation of a stand-alone module that calculates the stopping and range of incident ions producing tables that may be employed in external applications.

Defect models

Many researchers have published models for defect agglomeration in which the entire defect distribution is considered, as well as thermally-activated defect interactions. Defect production during ion bombardment and their subsequent thermal relaxation within the implanted lattice have been investigated by several authors.[10,11,12,13,14,15,16,17,18,83] Such effects are generally treated ad hoc without a first principles approach, and depend upon the strength of the defect-defect interaction and the defect mobility. For instance, the interdiffusion of ion-induced defects is known to result in either recombination with complementary defects, clustering with like defects to form more stable defect configurations; or interactions with impurities leading to impurity diffusion.[7]

Kinchin and Pease[84] provided an extensive review of defect production following bombardment, primarily from radioactive sources. These authors also modeled defect production and showed that the number of defects produced by an ion of energy E could be estimated by the following simple formula:

$$N = \frac{E}{2\varepsilon_d} \qquad [3.1.12]$$

where ε_d is the displacement energy in a solid. This formalism is contained within TRIM[24] for efficient damage calculations. Also, defect profiles can be determined by TRIM operating in the full cascade mode in which all of the energetic knockon ions are followed. In this case, the stable displacements are tracked and recorded to generate a profile or distribution of the defects. Defects include only Frenkel defects, i.e. vacancy/interstitial pairs, separated by a critical distance.

Chadderton[12] reconsiders a homogeneous model of defect aggregation that is reasonably assumed for defect growth and that offers regimes where a heterogeneous model versus a homogeneous model is applicable. Chadderton further explains defect growth dependencies on implant fluence, flux, and temperature and relates these characteristics to the homogeneous versus heterogeneous approach. A square-root dependence of damage on implant fluence is indicative of homogeneous defect generation, while a linear relationship between damage and fluence indicates a transition to a heterogeneous model.

Further damage models have been offered to clarify the transition to a completely disordered or amorphous structure, i.e., no long range order such as found in a vitreous glass. Motooka, et al.[17] clarified the onset of amorphization at cold temperatures by invoking divacancy-mediated amorphization through an increase in the free energy of the lattice. He assumed that the lattice would undergo a spontaneous crystal-to-amorphous phase transition once the free energy of the defective crystal exceeds that of the amorphous phase. A few years after reporting the above results, Matooka showed that a divacancy and di-interstitial (D-D)[18] pair precipitated five- and seven-member rings, which are inherent in the structure of an amorphous lattice. He also noted these simple

defects result in the formation of voids, dislocations, and stacking faults, indicating amorphization to be a competitive process to the formation of these stable extended defects. Temperature-dependent studies revealed that as implant temperatures were increased, defects became more mobile forming larger, more stable clusters. Amorphization still may result if the density of these larger vacancy clusters increases sufficiently to increase the free energy of the lattice, thus inciting a crystal-to-amorphous transition.[17]

CHAPTER 4

NEW DAMAGE MODEL: THE ROLE OF EXCESS DEFECTS IN DEFECT-MEDIATED PROCESSES IN SI

Introduction

Atomic displacements during implantation occur as a result of the ion-atom interaction, i.e. scattering, that results in the transfer of sufficient energy to displace atoms from their lattice site. The displaced atom and the vacant lattice site are collectively known as a Frenkel defect-a vacancy-interstitial pair. As previously discussed, transport of ions in matter (TRIM)[24] calculates the Frenkel defect density either using the Kinchin-Pease approximation[84] as modified by two later authors[85,86] or a full damage cascade calculation in which the trajectories of the ion, as well as the energetic knockons, are tracked within the program. In general, the two techniques yield substantially the same numbers of Frenkel defects but slightly different distributions, as will be discussed later. TRIM requires the input of various parameters including the displacement energy, which is the amount of energy required to produce a stable Frenkel defect. The displacement energy in Si has been estimated to be ~25 eV, which is greater than the covalent bond energy for silicon. The energy must be sufficient, not only to break the bond, but also spatially separate the Frenkel pair to prevent spontaneous recombination. Such recombination will occur within a critical pair separation as a result of the lattice strain energy associated with the defect formation, and electrostatic attraction of the pair (if the defects are charged). TRIM does a very good job in calculating the distribution of the Frenkel defect, since it simply follows from the energy-loss of the ions and the recoiling lattice atoms. In the full-cascade mode, TRIM tracks the

positions of both the interstitials (i.e., knockons), as well as the vacant lattice sites. The absolute defect concentration is also reported by TRIM, which depends critically upon the value of the inputted displacement energy.

As indicated earlier, the amount of damage that remains after ion irradiation depends, in part, on the concentration of Frenkel defects produced during irradiation. A variety of thermally-activated reactions occur at temperatures where the defects are mobile. Interactions between dissimilar point defects (i.e., a vacancy and an interstitial) result in recombination or annihilation of the pair, while clustering of similar defects produce a variety of different outcomes. For example, small interstitial clusters can form prismatic dislocation loops while vacancy clusters can form three-dimensional voids in the lattice. Thus, a myriad of pathways exist for defects as they thermally relax to a metastable configuration. Given the degree to which defects control material properties and, thus, affect the physical and chemical processing of materials, it is vital that there be a reasonable model for predicating the behavior of the ion-induced Frenkel pairs during thermal relaxation. Given the variety of reactions involving the Frenkel defects, it is no surprise that no such model has previously been put forth.

As indicated above, the complexity of the relaxation process seems to preclude development of a comprehensive model to account for the effects of ion-induced defects. However, a model is proposed in this work that simply and elegantly circumvents this problem. While it builds upon existing models, its focus is on processes responsible for generating a defect imbalance within the lattice during implant processing. It is based upon a new insight or perspective into the defect interactions that suggests many of the ion-induced defects do not contribute significantly to processing phenomena. In

particular, it concentrates upon the effects of the spatial separation of Frenkel pairs, which has heretofore been ignored in other damage models. Spatial separation of pairs leads to an excess of one type of defect over the other at locations within the lattice so that the excess defects are either vacancy- or interstitial-type. For example, excess vacancies exist within a vacancy population whenever the average density of vacancies exceeds the density of interstitial defects. The model assumes that relaxation during thermal processing leads to complete recombination of the spatially correlated pairs but not the uncorrelated ones, i.e. the separated pairs. The excess defects persist within the implant volume since their spatial separation makes them resistant to recombination and/or attempts of thermal annealing to reduce their numbers. These defects will be referred to as "excess defects" throughout the remainder of the manuscript.

This defect model follows intuitively from an understanding of the ion implantation process. Much of the damage created along the ion's track, i.e. the spatially correlated defects, recombines promptly during the quenching of the ion collision cascade or during post-implant annealing. Different implant schedules or post implant thermal treatments are intended to rid the implant volume of defects and electrically activate the dopant species. The excess defects, however, persist beyond efforts to remove them from the implant volume. Thus, the majority of ion-induced defects generated within the implant process are annihilated by recombination, and only those defects with concentrations exceeding the average concentration of their complementary defect in a given localized region, (i.e., the excess defects) contribute to the formation of residual ion-induced damage.

A model to account for implant damage earns credibility if it correlates closely

with experimental results and can accurately predict damage in a variety of implant scenarios. Thus, a model must be able to account for the effects within materials following different implant conditions and/or thermal treatments. The present model is semi-quantitative and will be shown to posses these attributes. Of course, a caveat is that the model must be applied only to those conditions where it is relevant and, therefore, would be expected to predict the outcome, for instance, only in cases where recombination of the spatially correlated defects occurs. While this is not a severe constraint, this is almost always met in thermal processing of Si, the model would not be expected to predict the defect profile in Si irradiated at sufficiently low temperatures where thermally-activated recombination does not occur. Appropriately applied, the model can be used to develop techniques of manipulating or controlling the effects of ion-induced defects.

Use of TRIM to Determine Excess Defects

Much of the experimental work presented within this thesis details defect interactions and distributions following implantation at varying temperatures and fluences, as well as subsequent thermal processing. Since ion implantation and annealing processes are dynamic, it seems problematic that TRIM, an athermal model, could be utilized to describe such a dynamic environment. However, the simplicity of the model leads to a simple resolution. Since the model assumes that the only effect of these dynamic processes is recombination of the spatially correlated pairs, the TRIM simulation code is easily adapted to account for this dynamic situation. This is accomplished by simply subtracting the vacancy and interstitial distributions determined

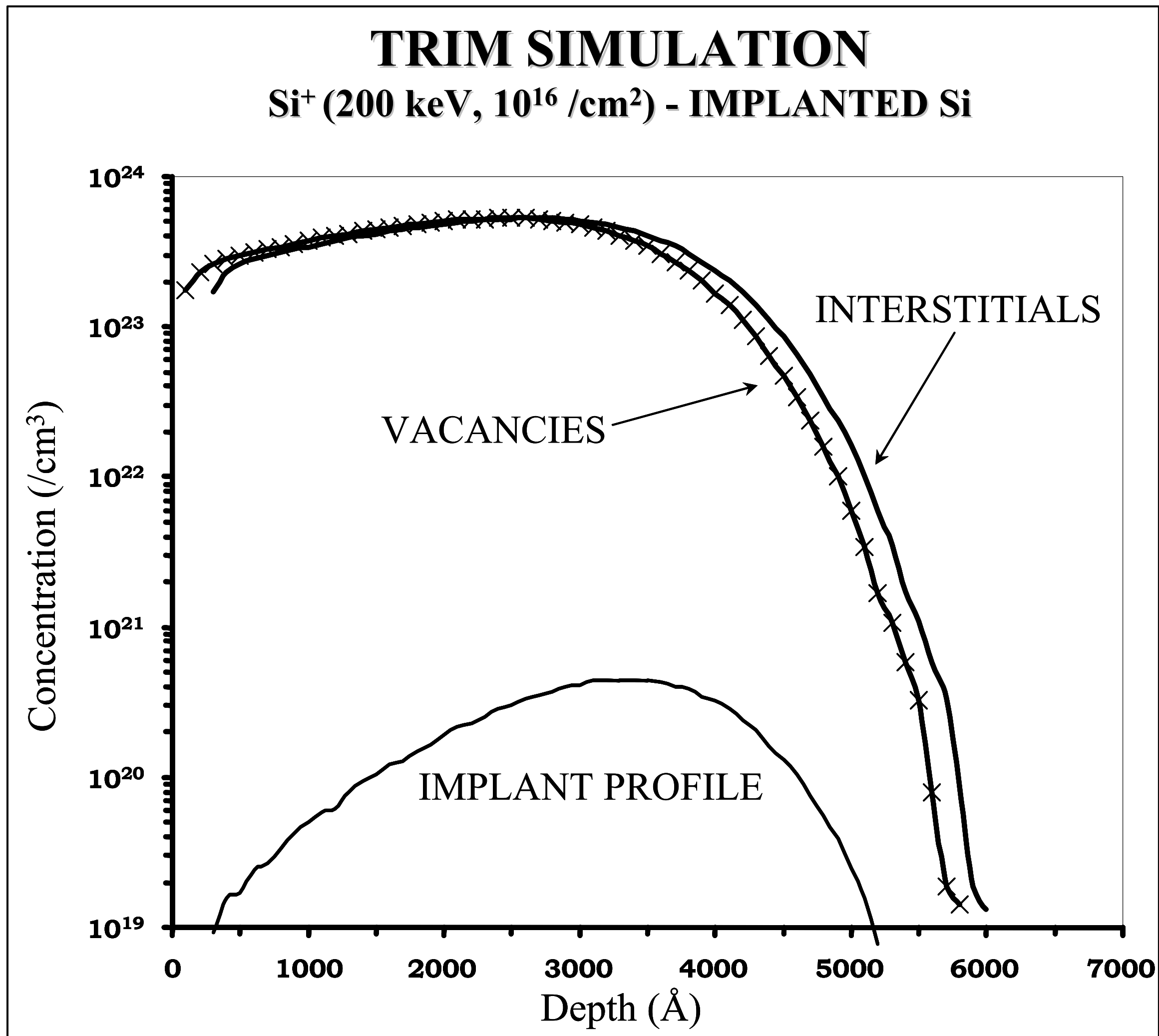

Figure 4. Total defect vacancy and interstitial profiles are portrayed with the implant profile from a TRIM simulation of 200 keV, 10^{16} Si^{+}-ions implanted into Si demonstrating the difference in magnitude between the total defect profiles and the distribution of implanted ions. The excess defect distribution is obtained by subtracting the vacancy from the interstitial profile simulating recombination between the spatially correlated ion-induced defects.

by TRIM and shown in figure 4. Regions of positive and negative concentration in the difference distribution indicate areas of excess interstitials and vacancies, respectively. Thus, the "modification" of the TRIM code just removes the spatially correlated pairs by subtraction, simulating pair recombination that occurs during or immediately following implantation or during the first stage of a post-implant annealing. Hence, the resultant profile yields the distribution of the spatially separated Frenkel pairs or the excess defect concentrations of vacancies and interstitials, i.e., the ones that survive recombination. Figure 5 illustrates the distribution of these respective defects for an implant of 200 keV Si^+-ions to a fluence of $10^{16}/cm^2$. Note the excess vacancy defects are distributed within the near surface while the excess interstitials form beyond. Interestingly, the excess concentration represents only about 1% of the total defects.[87] Given their small numbers, the excess defects have a profound impact on defect-mediated processes within the irradiated volume such as transient enhanced diffusion, TED.[88]

Regions of excess defects

Different processes produce spatially separated Frenkel pairs including the atoms added during implantation (known as the plus-one contribution), and dynamical processes such as sputtering and momentum transfer. Momentum transfer occurs during Frenkel pair formation, which leads to excess defects. Atomic displacements occur when a nonzero component of the ion's momentum is transferred to the lattice atom along the direction coincident with the incident ion. As a result of this displacement, the interstitial comes to rest at a depth greater, on average, than the location of the vacancy left behind. Consequently, the momentum transfer separates the pair resulting in a slight displacement of the interstitial defects from the vacancies. Excess interstitials produced by this

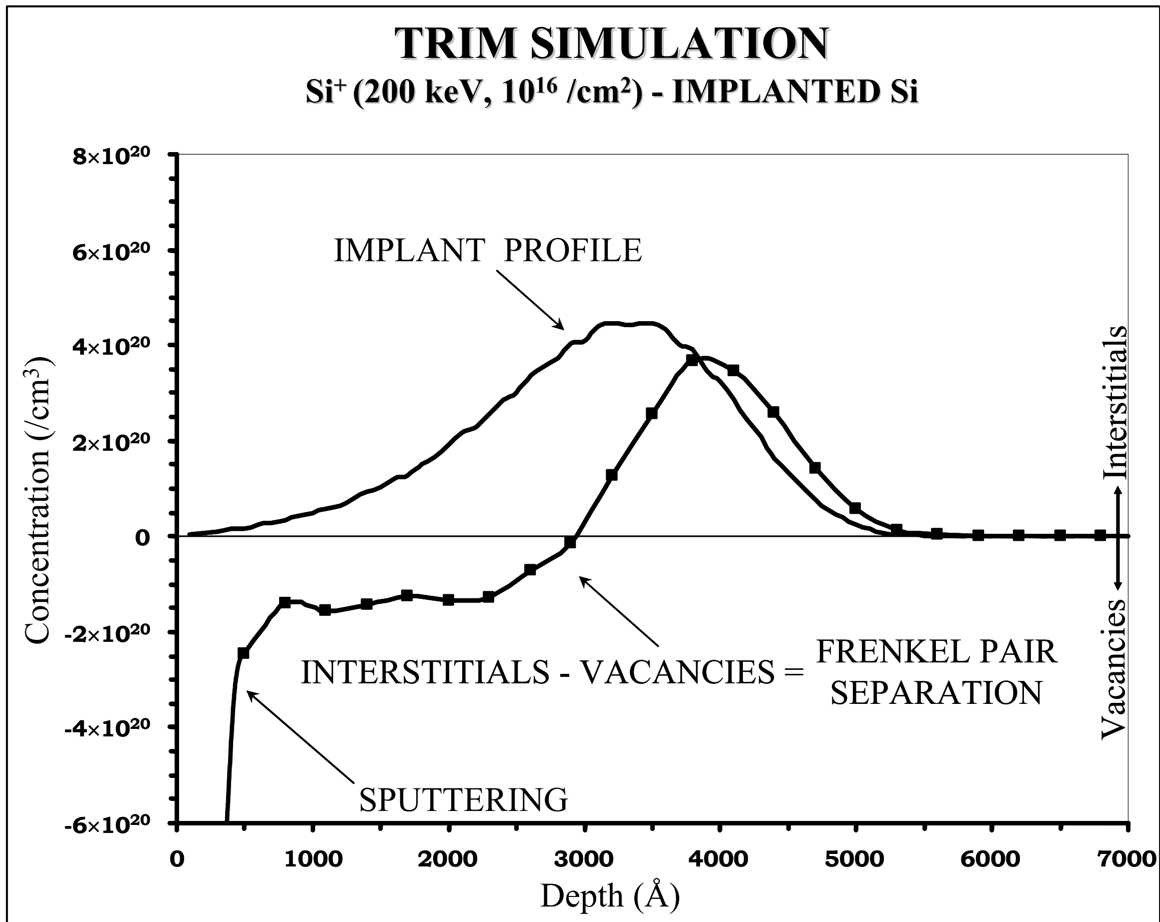

Figure 5. Implant and Frenkel pair separation profiles for a TRIM simulation of 200 keV, $10^{16}/cm^2$ Si^+-ions implanted in Si. The positive concentration reveals an interstitial distribution and the negative concentration a vacancy population. The surface sputtering effect is also identified.

mechanism will be shown to be located slightly beyond R_p, the projected range of the implanted ions.

A second source of excess defects follows from the inability of the lattice to accommodate the extra atoms introduced by implantation of an ion species to some fluence at a specified energy. As was mentioned earlier, this source of defects is referred to as "plus-one".[23] Dopant atoms may only be incorporated onto substitutional sites if an equal number of displaced Si atoms remain interstitially within the lattice. The impurity or host atoms incorporate onto substitutional sites during electrical activation. The concentration of the resultant distribution of interstitial-type defects roughly equals the implanted fluence and therefore is referred to as the plus-one state. Unlike Frenkel defects produced by ion-atom displacement collisions, these interstitials are not formed in conjunction with vacancies, and thus, the entire distribution can be treated as excess within the lattice.

The third and final source of excess defects is due to sputtering of the surface. This phenomenon produces a vacancy-rich layer over a few monolayers beneath the surface. These contributions are illustrated in figure 5 for the TRIM[24] simulation of 200 keV, $1 \times 10^{16}/cm^2$ Si^+, self-ions implanted into Si. Thus, the distribution of excess defects following the implant process consists of the spatially uncorrelated Frenkel pairs, the plus-one interstitials, and the vacancy-rich surface region due to sputtering. The benefit of this model is that these excess defect distributions are relatively static distributions and are accurately predicted by TRIM. Incidentally, the phrase, self-ion implanted, within this work refers to a crystalline substrate implanted with an ion beam of the same species.

Bulk, crystalline Si may be implanted with Si^{+}-ions, as an example of self-ion implantation.

Separation (SP) mechanism

The separation (SP) of the Frenkel pairs is a primary source of the excess vacancy defects. SP is the range of the displaced Si atom. As indicated earlier, the SP occurs as a result of the transfer of momentum to the knockon or interstitial atom along the direction of the incident ion. This component of momentum ensures that the interstitials generated during Frenkel pair formation will be distributed, on average, slightly deeper than the vacancies. It is of interest to explore the types of collisions that contribute to this process. This is accomplished by using a feature within TRIM[24] that allows the user to input a cut-off energy while running the program in the full damage cascade mode. This cut-off energy specifies a lower limit on the knockon atom below which TRIM does not track the knockon. A cut-off energy set at the value of the displacement energy would not provide any discrimination since all knockons would be tracked by the program while a cut-off energy set at the maximum transferred energy would then eliminate tracking of all the energetic knockons. Thus, the determination of the defect excess for intermediate values of the cut-off energy is used to explore the role of the energy transfer process in producing pair SP. Therefore, it will provide information on whether close-impact parameter collisions dominant the SP process, or if it is dominated by the more numerous collisions involving larger impact parameters (and smaller energy transfer). While small impact parameter events provide the most separation, these collisions are far more improbable than scattering at large impact parameters. Thus, calculation of how the SP changes by varying the final energy, E_f, will lead to a better understanding of this

mechanism and hopefully identify the types of scattering events that are most effective in producing the SP of defects.

An inverse relationship exists between the amount of energy transferred and the impact parameter. An illustration of the dependence between these two parameters is provided in figure 6 containing a plot of the energy transfer (eV) versus impact parameter in Angstroms (Å) for TRIM[24] simulations of 5.0 MeV Ge^+ and 500 keV Si^+ both on Si. The values for the impact parameter and energy transfer were extracted from TRIM for these two simulations. These energies were chosen for the different species to give comparable values. At larger impact parameters where the collisions are more numerous, the energy transfer is reduced to the order of a few eV. Alternatively, small impact parameter collisions, which occur less frequently, introduce a large energy transfer.

TRIM[24] simulations of 200 keV Si^+-ions, normalized to a fluence of $1 \times 10^{17}/cm^2$, were calculated for several different final energies. The final energy was varied from 5 eV to 100000 eV (100 keV). The default value for the cut-off energy built into TRIM for ion bombardment of a silicon layer is E_f =2 eV.[89] These simulations for the various cut-off energies are found in figure 7. TRIM simulations with final energies of 100 and 1000 eV are not included within the figure to allow for clarity. In figure 7, only the excess defect profiles resulting from the pair SP mechanism are shown. Increasing E_f will cause the program to terminate tracking the recoils below this energy thus effectively eliminating all scattering events producing energy transfers less than this value. For increasing values of E_f, the peak in the distribution of excess interstitials moves progressively closer to the surface. It is clear that the peak position and area are substantially affected at cut-off energies < 5000 eV. This is evidence of the importance of

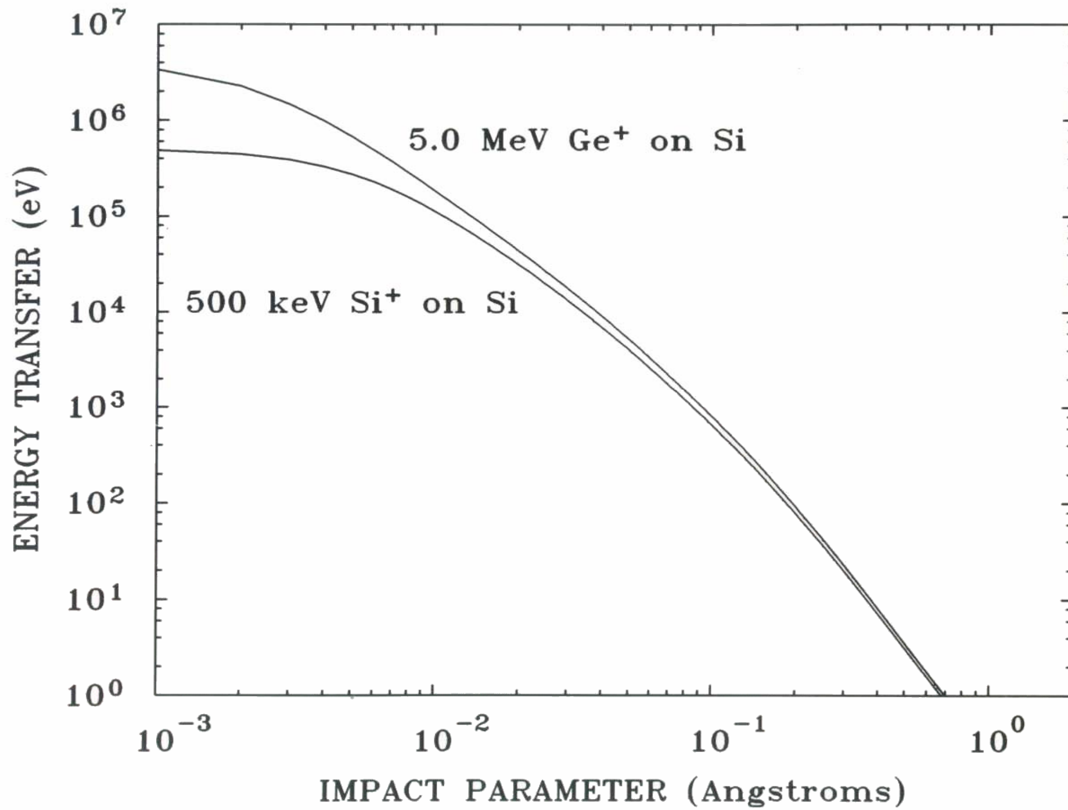

Figure 6. Dependence of energy transferred during collisions on impact parameter for TRIM simulations of 500 keV Si^{+} on Si and 5.0 MeV Ge^{+} on Si. An inverse relationship results; so that, a large energy transfer follows collisions with small impact parameters, and a small energy transfer from large impact parameter collisions.

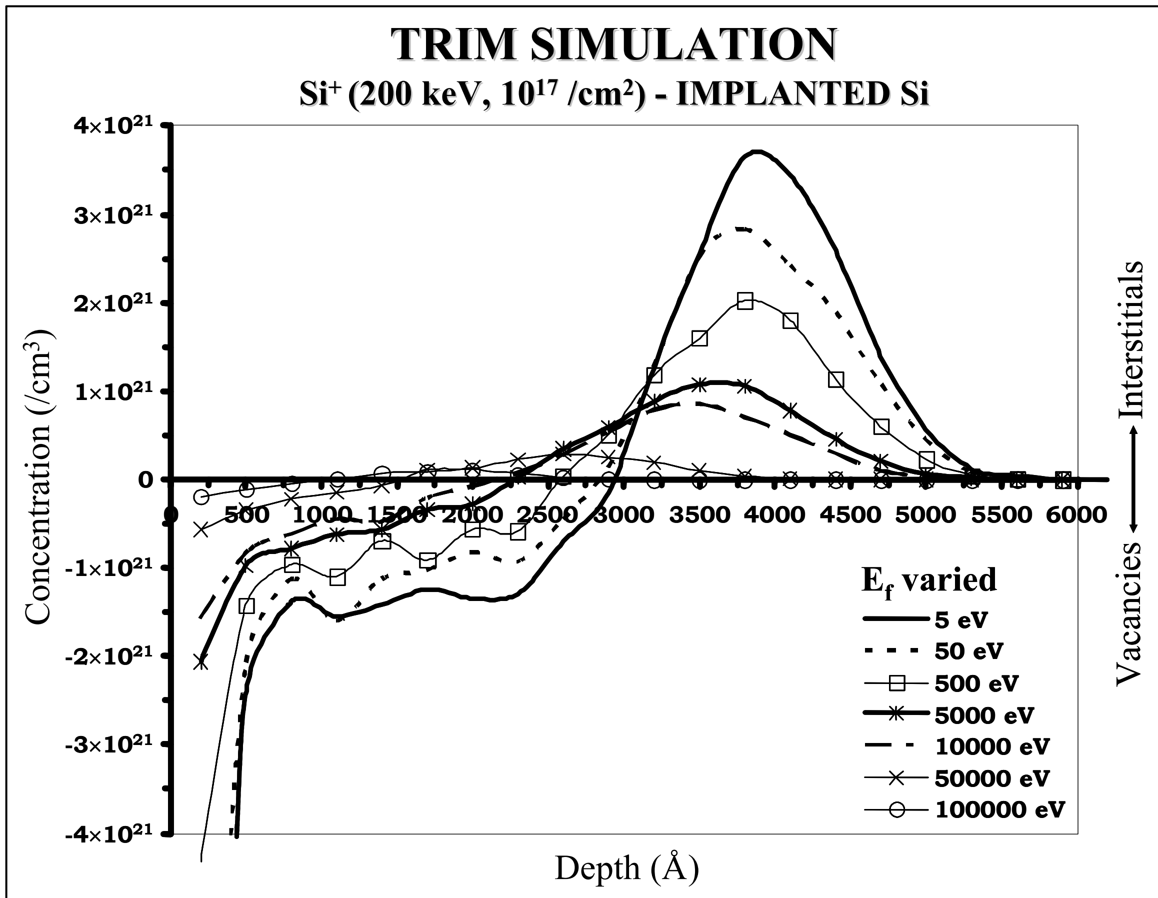

Figure 7. Frenkel pair separation from TRIM simulations of Si^+(200 keV, $10^{17}/cm^2$) incident on Si where the final energy, E_f, was varied for each simulation. The magnitude of the excess defect distribution decreases for higher final energies since fewer ions are tracked.

collisions within this energy range to the pair separation mechanism. The reduction in the total number of excess defects is, in part, due to tracking fewer collisions as a result of the use of the cut-off energy. It is interesting to note the substantial change for even the smallest increase, i.e., 50 eV, in the cut-off energy indicating sensitivity of the concentration of excess defects to this parameter.

The areal density of the interstitial excess peak was integrated. I divided the density of interstitial defects by the bulk Si density, 5×10^{22} atoms/cm^3, to obtain the range of separation. Data for this SP at the intermediate final energies are shown in table I. This range, in Angstroms, was plotted versus the cut-off energy, reported in eV, in order to understand the dependence of the defect SP on the final energy. This relationship is displayed in figure 8. The dependence of the SP on the final energy, E_f, suggests a decaying exponential relationship of the type:

$$SP \propto C_1 \exp\left(-C_2 \cdot E_f\right) \qquad [4.2.1]$$

where C_1 and C_2 are constants. A decaying exponential relationship was identified

Table I
Density of defects separated and converted to range in Angstroms for the final energies provided.

Cutoff energy, E_f (eV)	SP density ($\times 10^{17}$ at/cm^2)	SP (Angstroms)
5	4.19	838
50	3.68	736
100	3.41	682
500	2.75	550
1000	2.42	484
5000	1.72	344
10000	1.36	272
50000	0.422	84.4
100000	0.075	15.0

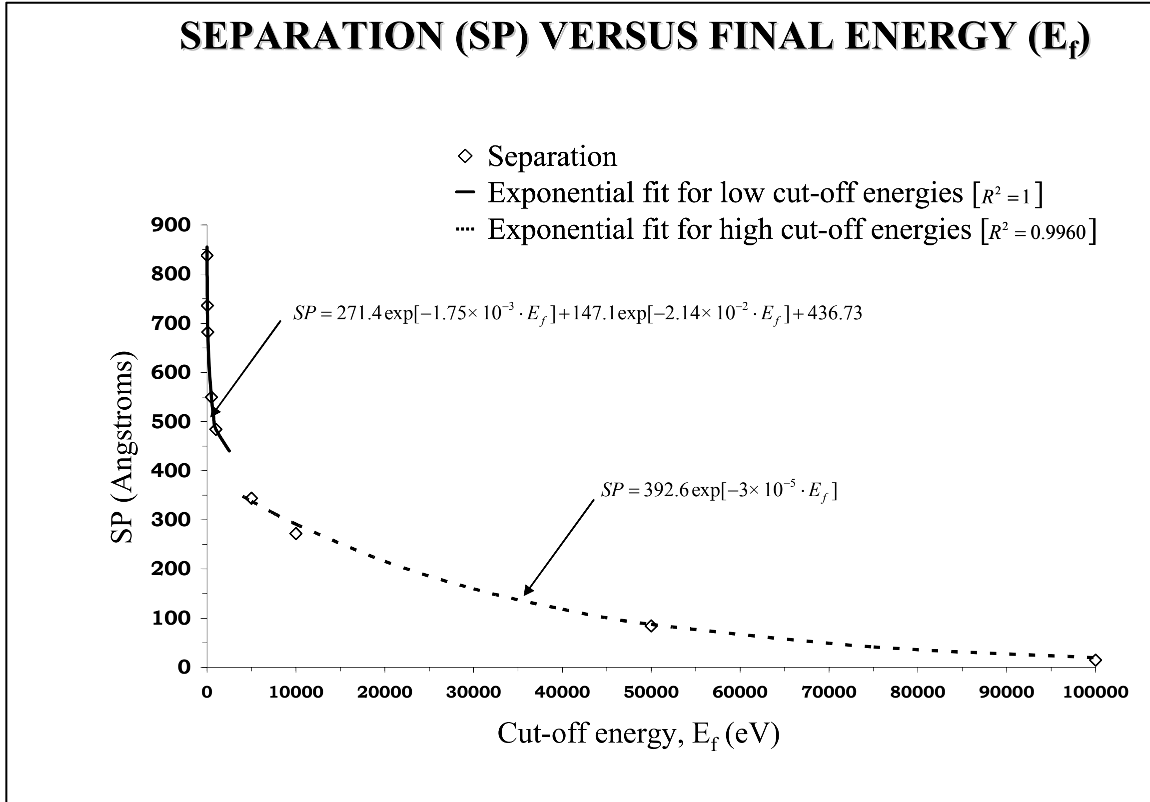

Figure 8. The separation (SP) or range of the separated defects was plotted versus final energy, E_f, and the data were fit with a decaying exponential relationship.

between the SP and E_f through a fitting procedure, and is shown in equations [4.2.2] and [4.2.3] below. The most accurate fit is obtained when the data are split into a high-final energy regime with cut-off energies between 5000 and 100000 eV and a low-final energy range with cut-off energies of 5 to 1000 eV. For high-final energies,

$$SP = 392.6 \exp[-3 \times 10^{-5} \cdot E_f], \qquad [4.2.2]$$

while for low-final energies,

$$SP = 271.4 \exp[-1.75 \times 10^{-3} \cdot E_f] + 147.1 \exp[-2.14 \times 10^{-2} \cdot E_f] + 436.73. \qquad [4.2.3]$$

Reasonable agreement is achieved between experimental data points and their relevant exponential fit. An R^2 value of 0.9960 was reported for the decaying exponential in equation [4.2.2] for higher-final energies (5000 to 100000 eV). The R^2 value is 1 for the second order decaying exponential fit in equation [4.2.3] for final energies below 5000 eV. The closer R^2 is to one (1) the better the fit of the data. Other fits, such as: a polynomial fit, power law, and higher order decaying exponential relationships were considered, but did not produce the same accuracy achieved by considering the SP in two energy regimes. Taking the first derivative of SP as it varies with E_f yields equations [4.2.4] and [4.2.5] for the higher- and lower-final energies, respectively. The first derivative of the SP for the higher energies is given by;

$$\frac{d(SP)}{dE_f} = -1.18 \times 10^{-2} \exp[-3 \times 10^{-5} \cdot E_f]. \qquad [4.2.4]$$

The first derivative for the lower-final energy regime is given by;

$$\frac{d(SP)}{dE_f} = -0.47 \exp[-1.75 \times 10^{-3} \cdot E_f] - 3.14 \exp[-2.14 \times 10^{-2} \cdot E_f]. \qquad [4.2.5]$$

Data from this evaluation of the SP mechanism are collected in table II.

Table II SP (Angstroms) and change in SP with respect to the final energy.		
$SP = 271.4\exp[-1.75\times 10^{-3}\cdot E_f] + 147.1\exp[-2.14\times 10^{-2}\cdot E_f] + 436.73$		
Cut-off energy, E_f (eV)	SP (Angstroms)	$\frac{d(SP)}{dE_f}$
0	855.3	-3.616
5	838.0	-3.294
10	822.3	-3.0040
50	736.0	-1.5148
100	682.0	-0.7696
250	612.8	-0.3215
500	550.0	-0.1980
750	509.9	-0.1279
1000	484.0	-0.0826
2500	440.2	-0.0060
$SP = 392.6\exp[-3\times 10^{-5}\cdot E_f]$		
Cut-off energy, E_f (eV)	SP (Angstroms)	$\frac{d(SP)}{dE_f}$
4000	348.2	-0.0105
5000	337.9	-0.0101
7500	313.5	-0.0094
10000	290.8	-0.0087
20000	215.4	-0.0065
30000	159.6	-0.0048
40000	118.2	-0.0036
50000	87.59	-0.0026
75000	41.38	-0.0012
100000	19.54	-0.0006

The changes in SP as a function of E_f, $\frac{d(SP)}{dE_f}$, or equations [4.2.4] and [4.2.5], are plotted in figure 9, revealing additional information about the dynamics of the SP. The change in SP as a function of E_f increases over several orders of magnitude for cut-off energies below 2500 eV. However, the change in SP per E_f varies more slowly for final energies above 2500 eV and extending over the entire energy range within this

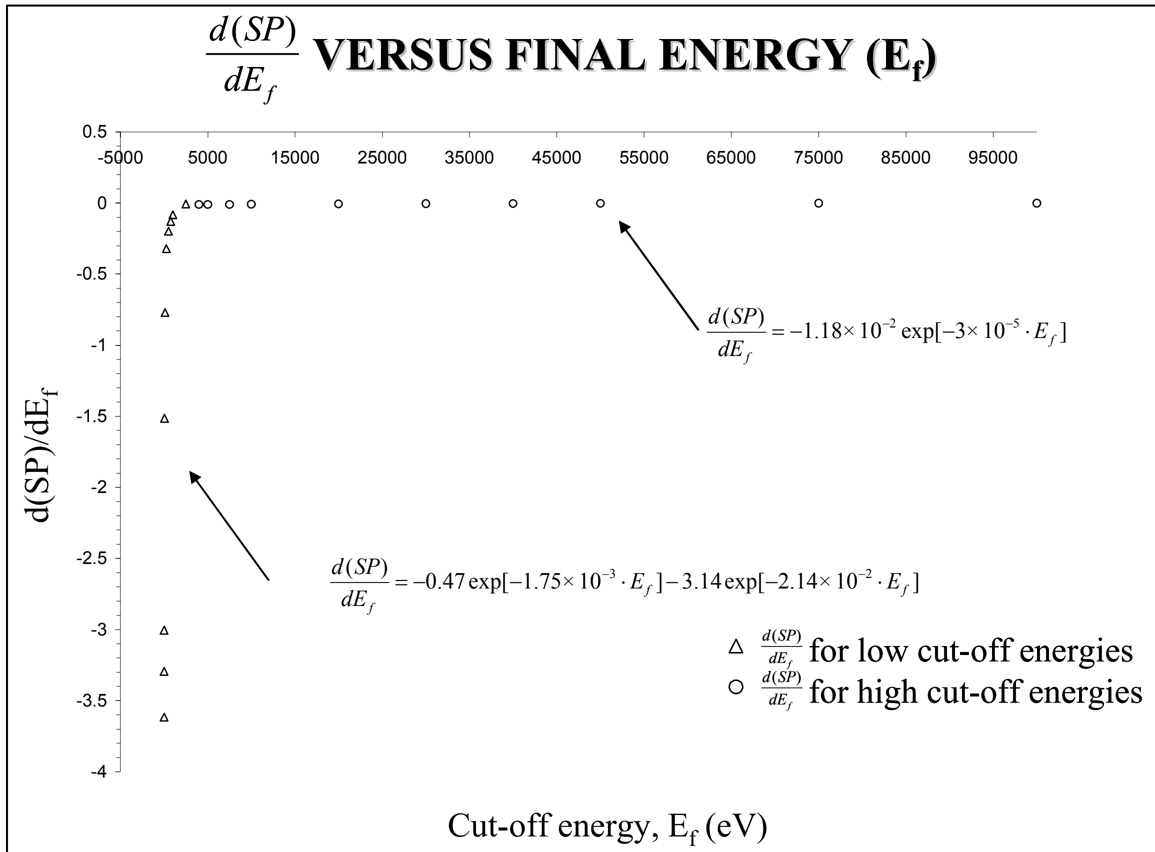

Figure 9. The change in the separation, $d(SP)/dE_f$, versus the final or cut-off energy (E_f), was measured. The change increases significantly for lower cut-off energies, but varies only slightly for higher cut-off energies, indicating large impact parameter collisions with small energy transfer dominate.

investigation. This clearly indicates that large impact parameter events play a dominant role in the pair SP mechanism. However, the higher-energy collisions do produce a small contribution to the effect. Therefore, the collisions responsible for the significant change in the SP for the low final energies are those with large impact parameters that transfer less energy. These collisions are much more probable than small impact parameter collisions that transfer larger amounts of energy. Change in the SP increased over several orders of magnitude for final energies below 2500 eV, but varied more subtly for higher-final energies above 2500 eV and extending over the range of energies considered, reaching 100000 eV.

The selection of energy was determined according to residual excesses within the implanted volume. I wanted to ensure a clear separation was achieved in the Frenkel pairs in order to study this model. For low energies, the separated pairs would be dominated by the implant profile.

Defect or damage accumulation models are generally employed to predict residual defect distributions following ion implantation that produce deleterious effects within the implanted volume. The excess defect model focuses specifically on the defects that persist in the lattice following implantation and post-implant thermal treatments. Implant procedures or engineering techniques, developed according to these defect models, are generally devised to alter the defect distributions in an effort to eliminate or control those defects. This prevents the necessity of higher anneal temperatures and longer thermal processes to remove stable defects, which may have undesirable effects within implanted materials. This model will be verified in the following chapters for a variety of implant conditions.

CHAPTER 5

VALIDITATION OF EXCESS DEFECT MODEL

A defect model must be validated by the accuracy in which observed phenomena can be explained and damage profiles predicted under different implant conditions. The excess defect model described in the previous chapter is based upon the premise that only those defects that survive implantation and subsequent thermal annealing are important for process modeling. Thus, only “excess” defects, at least to first order need to be accounted for in determining the effects of ion-induced defects on various physical phenomena such as diffusion of implanted impurities, as well as the morphology and density of secondary defects.

The validity of the excess defect model will be established in this chapter through a sequence of experiments in which ion-induced damage produced by a variety of ion implantation conditions is compared to transport of ions in matter (TRIM)[24] simulated profiles of the excess defects. The first experiments involve the evaluation of ion-induced damage distributions following implantation at different temperatures. This temperature dependent study is used to explore the scope of the excess defect model. This simple test of the model involves a straightforward comparison of damage distributions in ion-implanted Si to model predictions. It should be mentioned that the experimental damage distributions are determined from Rutherford backscattering spectrometry (RBS)/channeling measurements as detailed in appendix I. Such measurements are predominately sensitive to displaced atoms, i.e. interstitial-type defects. Vacancy-type defects are for the most part invisible to such measurements in that channeled ions predominantly interact with atoms in the interstices of the lattice. Therefore, in a region

of the sample containing only vacancy-type defects, RBS measurement will show little or no evidence of damage.

Damage profiles versus implant temperature

Si(100) samples were implanted with 150 keV Si^+ self-ions at different temperatures. The use of self-ions ensures that only ballistic mechanisms determine the ion-induced damage profile independent of chemical effects. Spectra in figure 10 compare the scattering yield in samples implanted at liquid nitrogen (LN_2) and 300° C. Since substantial dynamic annealing at the higher temperature reduces residual damage profiles at the higher temperature, different implant fluences, 10^{14} Si^+/cm^2 at LN_2 and 10^{16} Si^+/cm^2 at 300° C, were used to ensure that the same order of damage was present in each sample to facilitate comparison. Implantation at LN_2 temperature (•) produced a large scattering yield immediately below the surface peak. The location of this broad peak is somewhat shallower than the projected range, R_p=0.23 μm. The spectrum from the sample implanted at 300° C (+) is substantially different in both the yield and distribution of the damage. It contains a low scattering yield in the near-surface region separated from a high scattering yield well beyond R_p. This provides clear evidence of a bifurcation in the damage morphology in this sample. The damage yield in the 300° C implanted sample and the tail of the damage yield in the LN_2 implanted sample exist at a depth coincident with the end-of-range (EOR) of the implanted ions. These differences provide the basis for validating the excess defect model, as well as determining its range of applicability.

Results of a TRIM[24] simulation of 150 keV Si^+ implantation into Si are shown in figure 11. Only the excess defects generated by the pair separation mechanism, as well as

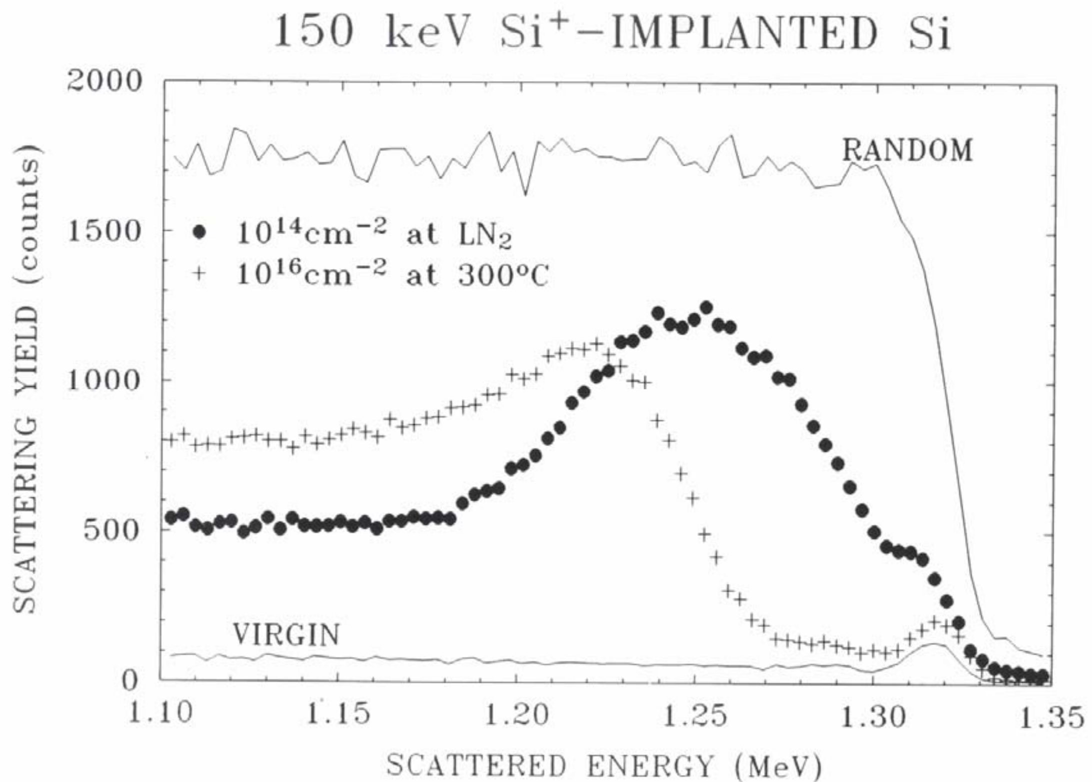

Figure 10. RBS aligned profiles of 150 keV Si^+-ions implanted into Si with $10^{14}/cm^2$ at LN_2 and 10^{16}/cm2 at 300° C. The 300° C implanted sample has a low scattering yield just below the surface that extends to a highly disordered region beyond R_p. The LN_2 sample has no bifurcation in the defect distribution which is expected due to the reduced mobility of the defects. Reprinted from *Mat. Sci. and Eng.* A**253**, O. W. Holland, J. D. Budai, and Bent Nielsen, "The role of defect excesses in damage formation in Si during ion implantation at elevated temperature", p. 240, Copyright 1998, with permission from Elsevier.

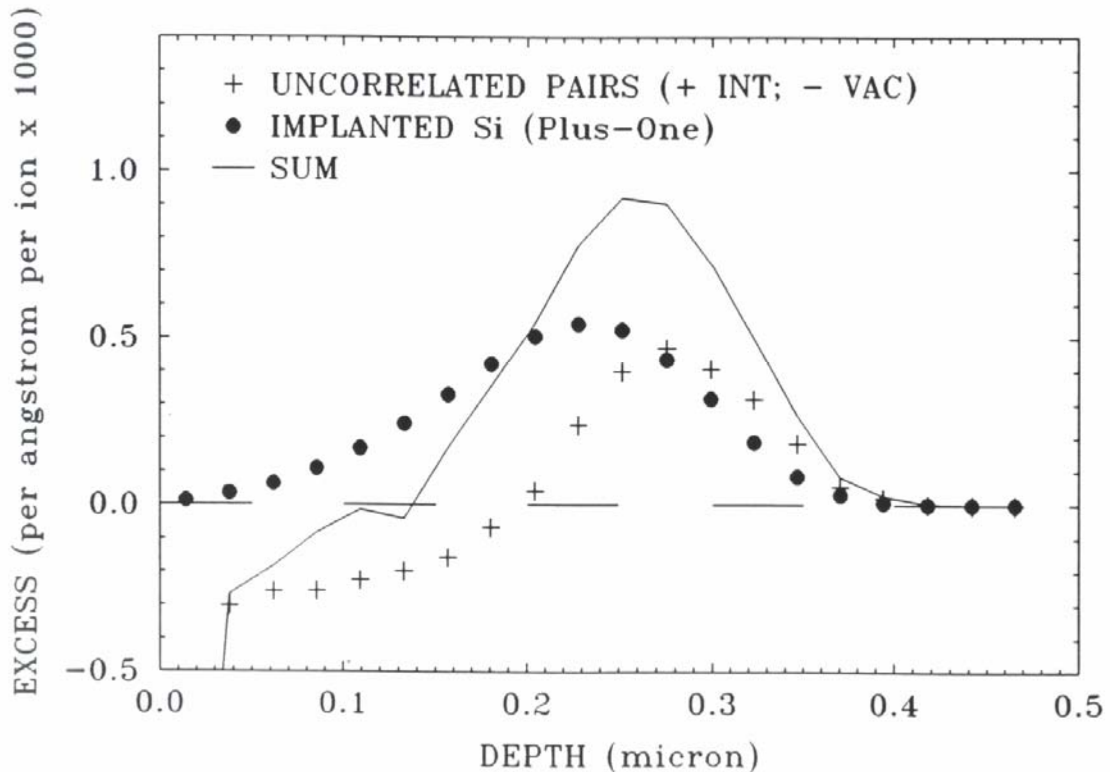

Figure 11. TRIM simulation of 150 keV Si^+ on Si illustrates the uncorrelated Frenkel defects; implanted Si or plus-one profile; and the sum curve, which combines the first two profiles. Reprinted from *Mat. Sci. and Eng.* A**253**, O. W. Holland, J. D. Budai, and Bent Nielsen, “The role of defect excesses in damage formation in Si during ion implantation at elevated temperature”, p. 240, Copyright 1998, with permission from Elsevier.

the implanted atoms are shown. The uncorrelated vacancy and interstitial Frenkel pairs are given by the + symbol, the distribution of implanted ions or plus-one by •, and the sum curve by the solid line, which consists of the algebraic sum of these different contributions. A negative value in the TRIM profile indicates excess vacancy defects and a positive value reports excess interstitials. The TRIM simulation in figure 11 shows excess vacancies near the surface extending to an approximate depth of 0.1 μm and excess interstitials beyond the excess vacancy region, with a peak concentration approximately 0.25 μm below the surface.

The damage produced at different temperatures is compared to the TRIM simulation of 150 keV Si^+-ions implanted into Si in Figure 12, a and b. The damage was extracted from each of the RBS scattering profiles of implants performed at different temperatures and scaled to yield a peak value near the TRIM[24] results. Scaling factors of 0.18 and 0.035 were applied for the LN_2 and 300° C implanted samples, respectively, to bring the measured damage coincident with the TRIM values. The location and the shape of the extracted damage were compared with TRIM results. It should be noted that, in figure 12a, the measured damage distribution at LN_2 is compared to the total number of displacements predicted by TRIM (rather than the excess defects). It is well known that at cryogenic temperatures, ion-induced defects are substantially immobile and will cluster to yield stable complexes and/or amorphous zones. Therefore, the substantial amount of dynamic recombination of complimentary defects, assumed in the excess defect model, is not expected at cryogenic temperatures. Thus, good agreement is anticipated between the total number of displacements and disorder measured with RBS channeling of 10^{14} Si^+/cm^2 implanted at LN_2 temperature but not at the higher temperature. It is clear in

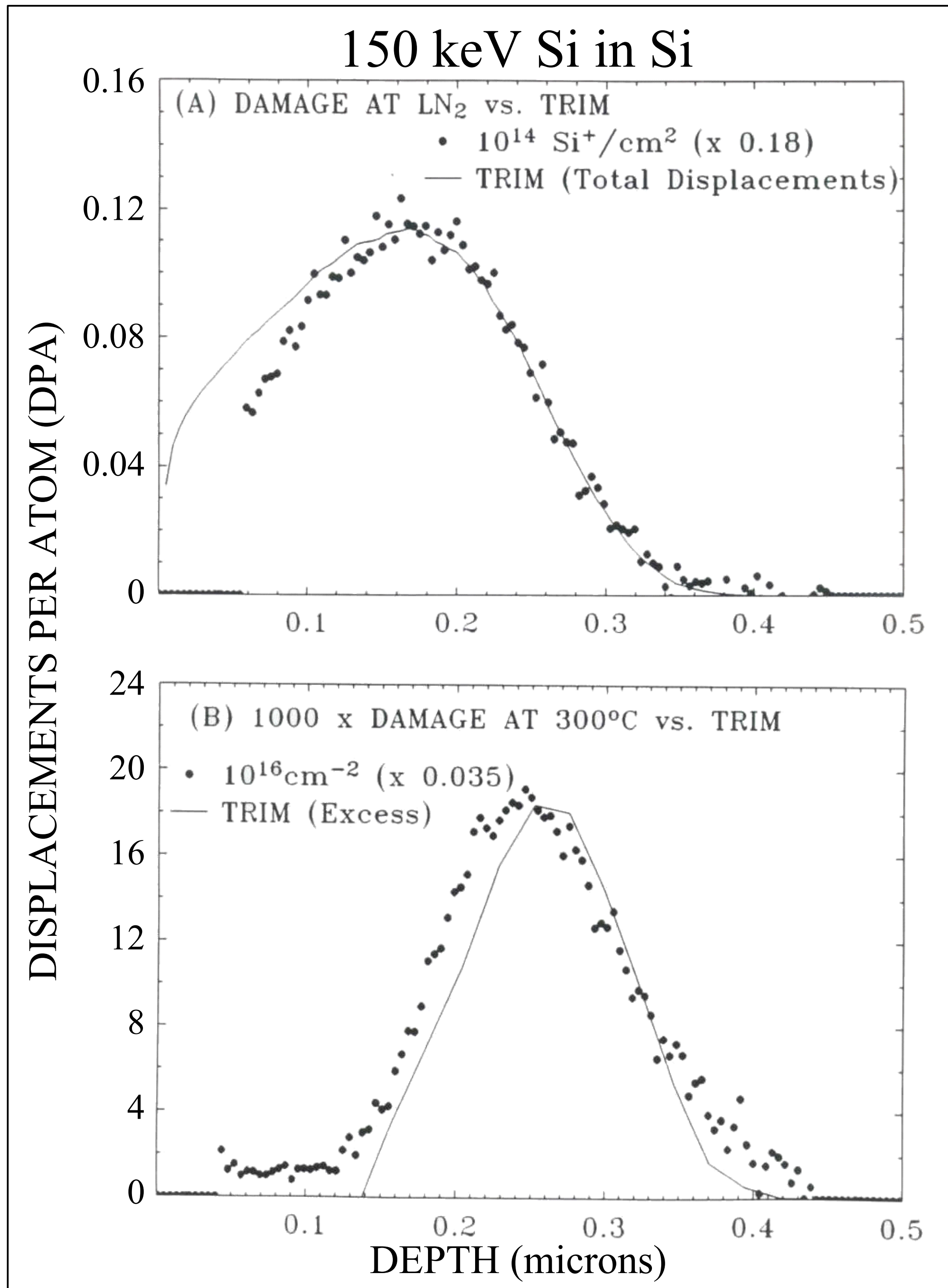

Figure 12. Damage extracted from RBS profiles is compared with TRIM simulations for 150 keV, 10^{14} Si^+/cm^2 (a) and 10^{16} Si^+/cm^2 (b) implanted at LN_2 temperature and 300° C, respectively. Damage at LN_2 resembles the total defect profile due to reduced defect mobility. The excess defect profile compares with the damage from the 300° C profile, confirming recombination of spatially correlated defects. Reprinted from *Mat. Sci. and Eng.* A**253**, O. W. Holland, J. D. Budai, and Bent Nielsen, “The role of defect excesses in damage formation in Si during ion implantation at elevated temperature”, p. 240, Copyright 1998, with permission from Elsevier.

figure 12b that the damage distribution at 300° C is not correlated to the TRIM results for the total displacements. Rather, comparison with the total excess defects (i.e., the 'SUM' curve (—) in figure 11) yields good agreement with the damage profile from the 300° C implant. In figure 12b, the depth of the peaks of the damage curve and the excess curve from TRIM are offset only slightly. Therefore, the damage within the lattice observed from the 300° C implanted sample [fig. 12b] is well predicted by only considering the excess defects. The good agreement in figure 12b, therefore, strongly suggests the spatially correlated pairs quickly annihilate by recombination during annealing and are of no consequence to defect-mediated processes. It is apparent that the low mobility of the ion-induced defects during cryogenic implantation results in little or no recombination but rather influences defect clustering to form stable defect complexes.[8,89] Thus, the damage distribution from the LN_2 implanted sample (see •-profile in figure 11) correlates well with the total numbers of defects rather than the excess defect distribution. However, for elevated implant temperatures of room temperature (RT)[8,90] and above, higher defect mobility enhances recombination of the spatially-correlated defects resulting in a damage distribution primarily determined by the excess defects.

Further evidence of the excess defect population was provided by positron analysis. Recall, the positron annihilation spectroscopy (PAS) analysis technique is sensitive to only vacancy-type or open-volume defects. A measurement of an S-parameter greater than one indicates the presence of open-volume defects. Silicon-on-insulator (SOI) material implanted with 2 MeV Si^+-self ions to a fluence of $1 \times 10^{17}/cm^2$ was analyzed. The higher energy ions have a range that is well beyond the buried oxide and, therefore, separated from the superficial Si layer. As one moves towards the surface

from the Si/SiO_2 interface at 12 keV in figure 13, the S-parameter is seen to increase, indicating a significant presence of vacancy-type defects in the superficial region at the surface. These results support the prediction from the excess-defect model of an excess vacancy concentration within the near-surface.[19,91] The persistence of the vacancy-type defects within the superficial Si layer at higher temperatures indicates the buried oxide is an effective barrier to defect diffusion (at the implantation temperature), thus, inhibiting recombination between vacancies in the near-surface region and the interstitials beneath the buried oxide at R_p of the MeV implant.[32]

Next, residual ion-induced damage is compared to TRIM[24] simulated damage profiles under conditions involving ion fluences sufficient to produce a crystal to amorphous transition. In particular, ion implant conditions were used to form a continuous amorphous layer within the implanted volume in Si. Of particular interest in these samples was the residual ion-induced damage within the crystal, beneath the amorphous layer near the phase interface. Various implant temperatures were used to control or manipulate the morphology/amount of this damage at the amorphous-crystal (a-c) interface. It is well known that the thickness of the amorphous layer formed by implantation decreases as the implant temperature is increased. Since the mobility of the ion-induced defects is increased at higher temperatures local recombination is promoted resulting in movement of the interface towards the surface or decreasing the width of the amorphous layer. Hence, a greater concentration of crystalline defects is anticipated below the interface with increasing implant temperature. As^+-ions were implanted into Si (100) to a fluence of $5 \times 10^{15}/cm^2$ at an energy of 120 keV and at temperatures of either LN_2, RT, 100° C, or 150° C. In addition, post-implantation annealing at 600° C for 15

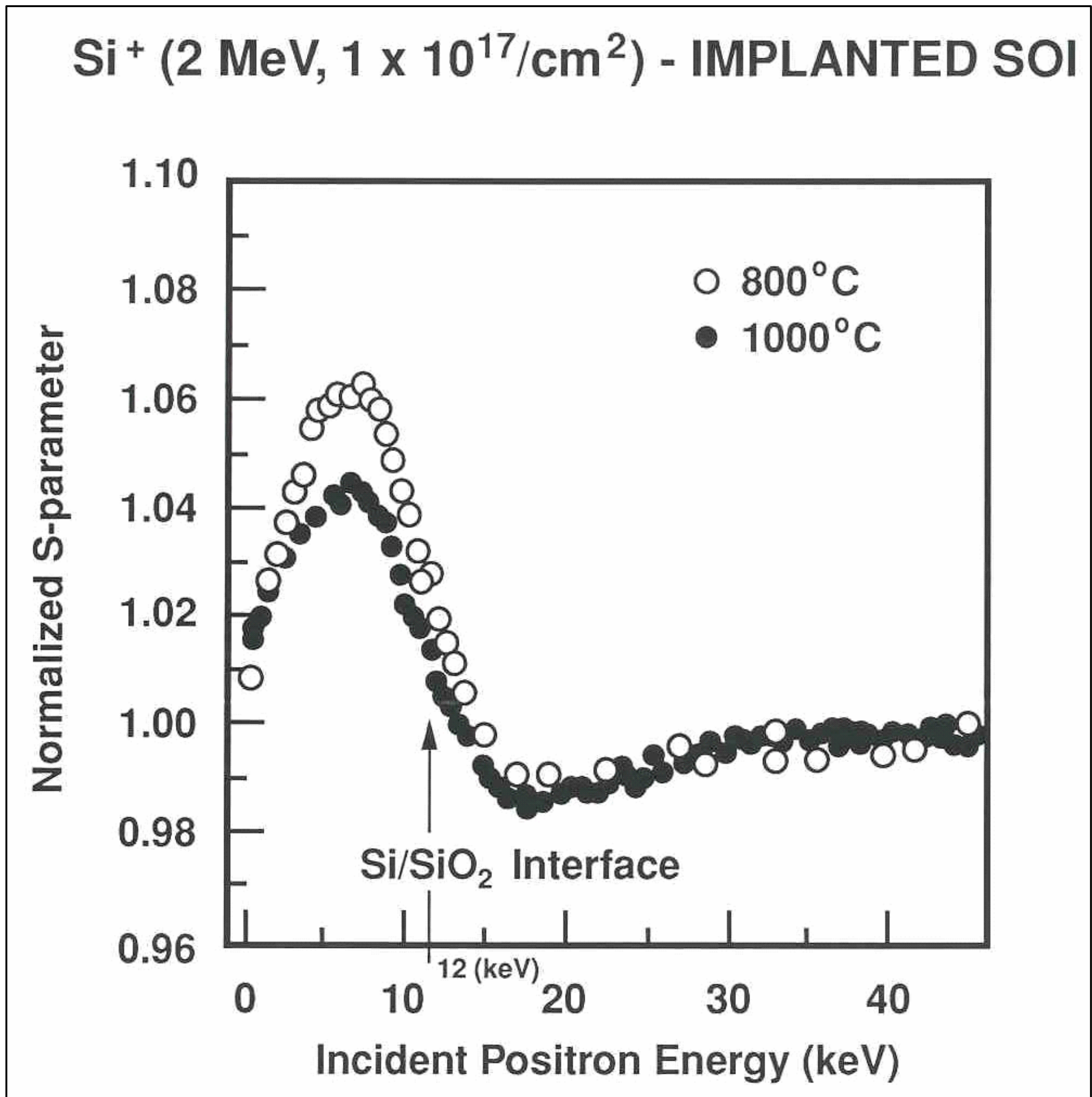

Figure 13. PAS was performed on SOI implanted with 2 MeV, 10^{17} Si^{+}/cm^{2} and annealed at 800 and 1000° C. Moving towards the surface from the Si/SiO_2 interface, located at 12 keV as indicated by the arrow, the vacancy defects survive in the near surface layer. The S-parameter remains above one (1) even at the higher annealing temperatures. Reprinted from *J. Electron. Mater.* **26**(11), E. G. Roth, O. W. Holland, V. C. Venezia, and Bent Nielsen, "Methods of Defect-Engineering Shallow Junctions Formed by B^{+}-Implantation in Si", p. 1349, Copyright 1997, with permission from TMS (The Minerals, Metals & Materials Society).

minutes was performed to crystallize the amorphous layer.[92] Crystallization occurs as a result of solid-phase-epitaxial-growth (SPEG), which eliminates the amorphous layer but leaves crystalline defects below the original (as-implanted) a-c interface. The removal of the amorphous layer by SPEG is important because it permits the residual defects at the initial a-c interface to be probed by RBS/channeling measurements. Inherent in these measurements is the assumption that these crystalline defects are stable at 600° C, the SPEG temperature. The residual defects at the a-c interface of the implanted material were compared to the number of excess defects within this region calculated by TRIM.

RBS/channeling analysis performed on these four samples shows the amorphous layer to be completely recrystallized, following SPEG at 600° C for 15 minutes in figure 14. The scattering yield from the implanted samples is identical to that from a virgin or unimplanted sample within the near-surface region [fig. 14]. However, significant damage remained below the original a-c interface. It is clear that the damage below the a-c interface increases with implant temperature. This is the only damage that survives the anneal at 600° C; all other lattice disorder is eliminated following regrowth of the amorphous layer, as expected.[92] This residual damage was integrated using the damage extraction routine, as described in appendix I, and then compared to TRIM simulations. Only the TRIM-simulated excess defects found beyond the depth of the a-c interface (as determined by RBS) were used in the comparison. The defects found below or deeper than the a-c interface coincide with the end of the implanted ions' track, and include portions of both the separated Frenkel interstitials and the plus-one contribution, which is also interstitial in nature.[93,94] The integrated damage (atoms/cm^2) in the regrown samples at each implant temperature is given in table III. The respective depth of the a-c interface

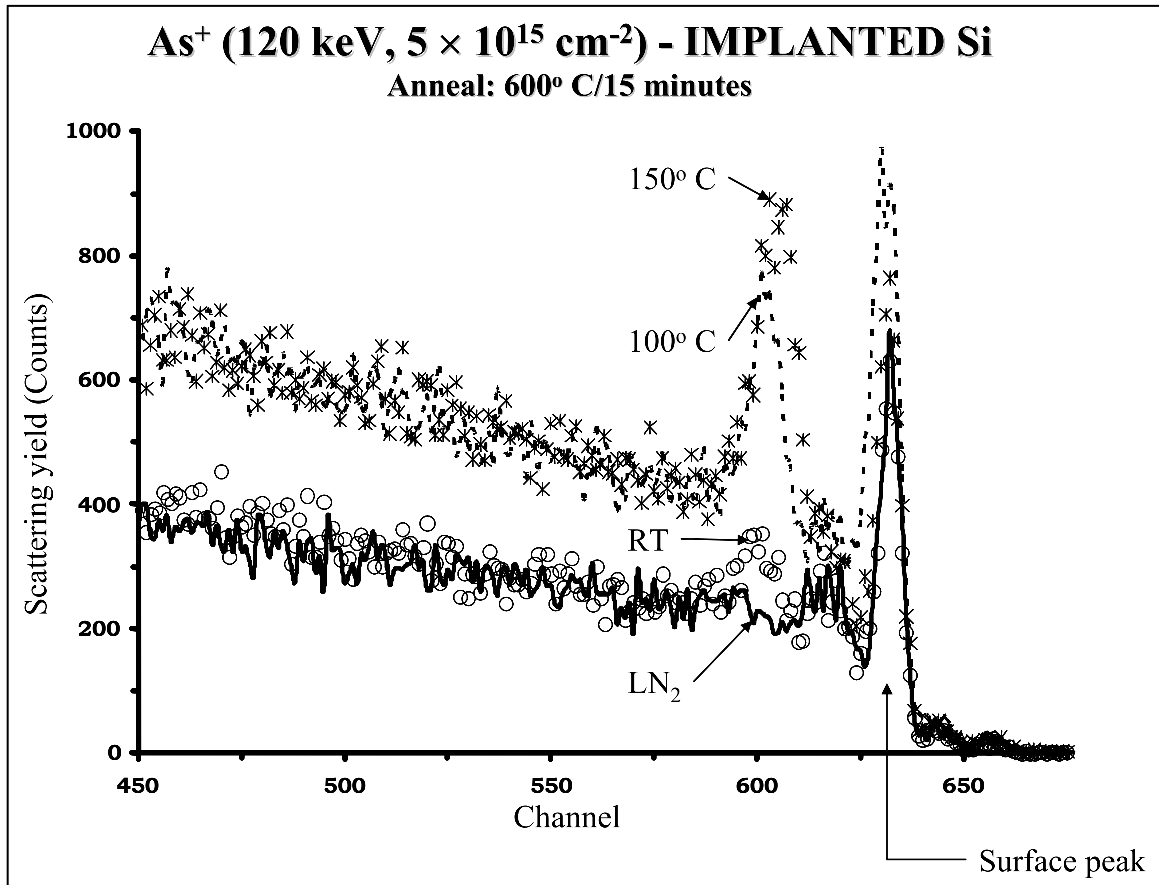

Figure 14. RBS <100> aligned spectra of As^{+}(120 keV, 5 × 10^{15}/cm^2) implanted into Si at 150° C, 100° C, RT, and LN_2 and annealed at 600° C for 15 minutes to regrow the amorphous layer created by the implant. The disorder in the sample implanted at 150° C is greater considering the deeper amorphous layer following implantation at lower temperatures encompasses more ion-induced defects within the amorphous layer. Defects within the amorphous layer are eliminated upon regrowth.

Table III
Excess damage beyond the a-c interface at various implant temperatures.

Implant Temperature	Depth of a-c Interface (Å)	Damage ($\times 10^{14}$ atoms/cm^2)
150° C	933	295
100° C	1213	146
Room Temperature (RT)	1325	42
Liquid Nitrogen (LN_2)	1633	0

is also listed in the table for each temperature.

Two numbers were extracted from TRIM; the integrated number of excess interstitials, which includes contributions from both the plus-one and the pair separation mechanism, and the plus-one only. As illustrated in figure 15, the excess defects as determined by TRIM closely matched (to within a scaling factor of 2) the experimental values of the residual damage below the a-c interface. It is clear that the damage from the plus-one contribution (also shown in the figure), with the same scaling factor, yielded damage far below that observed in the experimental spectra. This indicates the importance of the pair separation mechanism in contributing to the excess defects for the present implantation conditions. These results confirm that when, “all” sources of excess defects, i.e. both the spatially separated interstitials from the Frenkel defects (or recoils) and the plus-one, are considered, the interstitial damage located at the original a-c interface may be modeled effectively with the excess defect model. Thus, the examples have shown that the excess defect model can reasonably predict both the vacancy-excess in the near-surface, as well as the interstitial type excesses near the end-of-range.

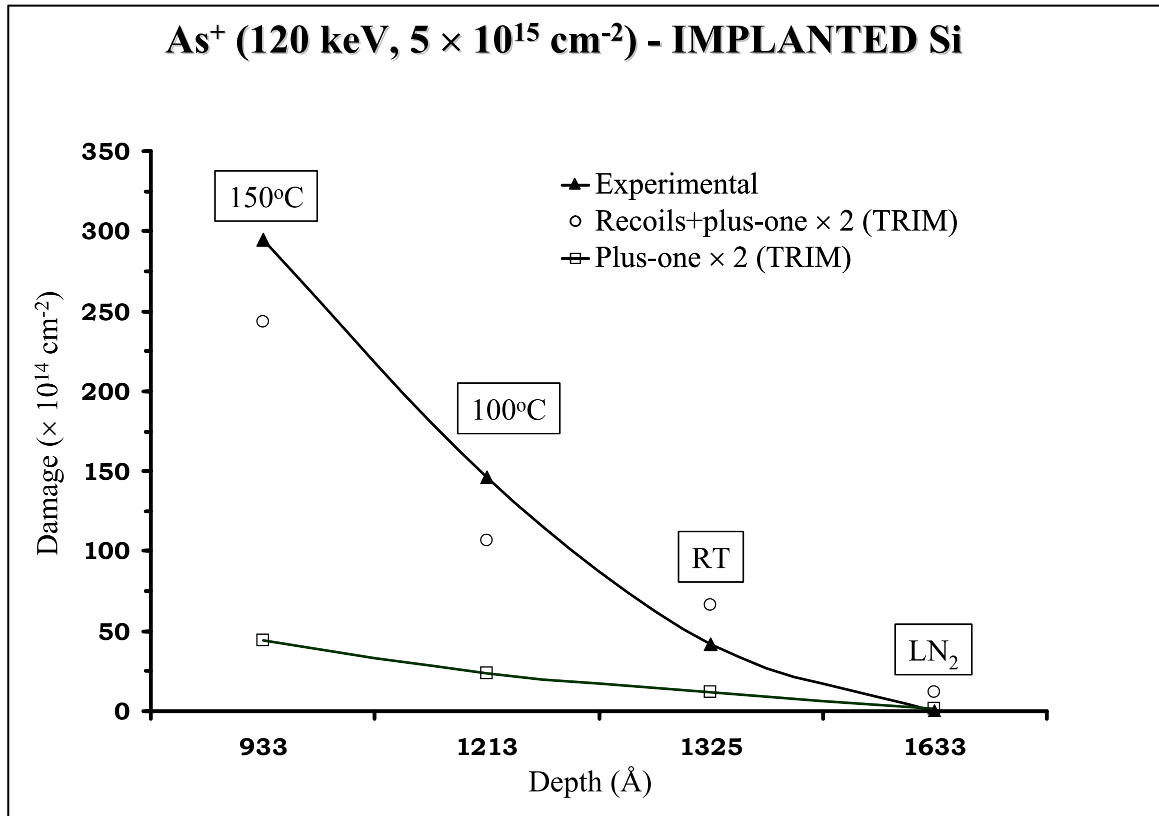

Figure 15. Damage from 120 keV, 5×10^{15} As^+/cm^2 implanted at LN_2, RT, 100° C, and 150° C compared with damage estimated from TRIM simulations of the As^+ implant. The plus-one from TRIM alone was far below the implant damage, however, the portion of the separated Frenkel pairs and the plus-one together from TRIM coincide with the measured implant damage. Reproduced from E. G. Roth, O. W. Holland, and A. Meldrum in *Silicon Materials Science and Technology 1998*, Proceedings of the Eighth International Symposium on Silicon Materials Science and Technology, PV 98-1, edited by H. R. Huff, H. Tsuya, and U. Gösele (NJ: Pennington, 1998), p. 938 by permission of The Electrochemical Society, Inc.

Co-implantation of high- and medium-energy Si^+-self ions below the amorphization threshold

Discussion

This study was performed incorporating ion implantation processing with both high- and medium-energy ions. This dual implantation scheme was used both to provide additional validation of the excess defect model and to explore an engineering technique for manipulating ion-induced damage. A combinatory approach, presented in figure 16, was used to determine whether or not the excess defect model could be engineered to manage ion-induced damage. Samples were self-ion implanted at different energies and analyzed to study the synergistic effects resulting from this dual implant scheme. This dual implantation procedure created situations where defect excesses of one type produced by a second implant were made to overlap regions containing complementary defect excesses from an initial implant. The presumption in the technique is that such complementary defects would spontaneously recombine and thus annihilate each other. The excess interstitials from the high-energy implant are located several thousand Angstroms beyond the region of interest and are not anticipated to influence the interaction in the near-surface, i.e. the excess vacancies from the high-energy implant and the interstitials at the EOR of the medium-energy implant. Some researchers, Venezia and coworkers[95] and Ranieri and coworkers[96], for example, suggest interstitials from R_p of a MeV implant may traverse the denuded region between the interstitials and vacancies and hence promote recombination. While such a mechanism is possible, a high-density dislocation network is formed near R_p, which effectively traps most of the

Co-Implantation of High- and Medium-Energy Si^+-ions

High-energy implant: Si^+ (1.25 MeV, 5 × 10^{16} /cm^2, 250°C)

Medium-energy implant: Si^+ (200 keV, 10^{15} - 10^{16} /cm^2, 250°C)

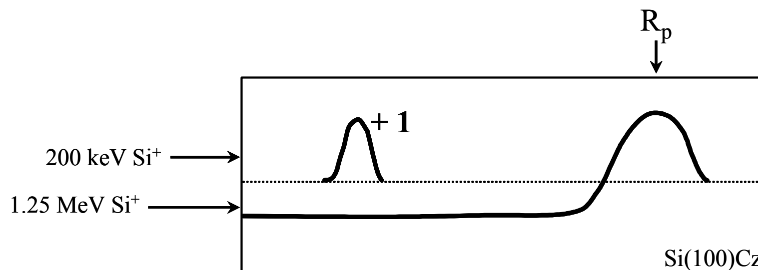

Investigate the dependence of the damage that follows ion irradiation on:

1. Order of implantation
   Order 1: MeV Si^+-ions + Si^+(200 keV, 10^{14} - 10^{16} /cm^2)
   Order 2: Si^+(200 keV, 10^{14} - 10^{16} /cm^2) + MeV Si^+-ions
   *MeV implant fixed (above parameters)
2. Fluence of 200 keV Si^+-ion implant
3. Implant temperature: 150, 250, and 450° C

Figure 16. Dual implants of 1.25 MeV, 5×10^{16} Si^+-ions/cm^2 and 200 keV Si^+ to different fluences at implant temperatures of 250 and 450° C are used to investigate the dependence of the ion induced damage on implant temperature and fluence of the 200 keV Si^+-ions, and the order of the MeV and keV implants.

interstitials generated within it. Thus, recombination of the complementary excesses in these spatially separated regions will be ignored in the present discussion.

The results in this section will illuminate aspects of the defect interactions; specifically, highlighting the role of excess vacancies left by an initial high-energy implant in affecting damage accumulation of a lower energy Si^+-ion implant. In this dual-implant experiment, synergistic effects of ion-induced damage were considered without reduction through thermal annealing.

Co-implantation of MeV and keV Si^+-ions into Cz-Si (100)

Fluence of 200 keV Si^+-ion implants

Czochralski (Cz)-Si (100) material (p-type, resistivity: 1-10 Ωcm) was implanted with $5 \times 10^{16}/cm^2$, 1.25 MeV Si^+-ions at temperatures of 450 and 250° C. The energy and fluence of the self-ion, MeV implant were fixed (1.25 MeV, $5 \times 10^{16}/cm^2$ Si^+). Only the implant temperature was altered. The MeV implants were performed on a 1.7 MV General Ionex tandem accelerator. The use of a tandem accelerator to implant 28 amu Si^+-ions ensures the beam was free of contaminants with the same mass-to-charge ratios that are potentially present when using a single-ended machine. In addition, implants were done with a raster-scanned beam to generate uniformly implanted areas.

Following MeV implantation, 200 keV Si^+-ions were implanted with a range in fluence extending over two orders of magnitude, from 10^{14} to $10^{16}/cm^2$ at the same implant temperatures, 450 and 250° C, as the MeV implant. The energy 200 keV was chosen to place the 200 keV implanted ions near the peak of the excess vacancy defects from the high-energy implant. Thus, the experimental conditions were chosen to locate the peak of the interstitial distribution of the lower-energy self-ions within the vacancy

excess formed by the MeV ions. The fluence of the 200 keV Si^+ implants varied depending upon the implant temperature. At 450° C, the fluence was varied by two orders of magnitude, ranging from 7×10^{14} to $1.5 \times 10^{16}/cm^2$. Fluences ranging from 10^{14} to $10^{16}/cm^2$ were implanted at 250° C. The implant matrix is summarized in table IV. For these medium-energy implants, the use of a 30 amu Si^+-ion beam minimized the probability of beam contamination, especially from N_2^+ or CO^+. Si was chosen for this study following dual implantation so the interaction of defects would not be convoluted with chemical effects.

Table IV
Implant matrix for dual implants of experiment II: Co-implantation of high (1.25 MeV)- and medium (200 keV)-energy Si^+-self ions below the amorphization threshold.

Implant Temperature	Fluence of 200 keV Si^+-ions ($\times 10^{14}/cm^2$)															
450° C				7		10		30	50		80		100	120	140	150
250° C	1	3	5	7	9	10	20	30	50	70		90	100			
MeV implant of Si^+(1.25 MeV, $5 \times 10^{16}/cm^2$), remains fixed.																
MeV/kev order: 1.25 MeV Si^+-ions implanted prior to 200 keV Si^+-ions.																
keV/MeV order: 200 keV Si^+-ions implanted prior to 1.25 MeV Si^+-ions.																

Implant temperature

As was mentioned above, implants were done at two different temperatures, 450 and 250° C. The implant temperature was varied to investigate how temperature impacts the dynamics of the defect interactions and alters the ion-induced defect distributions. The implant temperature of both implants was maintained consistently at elevated temperatures to promote local recombination during the implant process and prevent amorphization of the lattice. The temperature was monitored with a thermocouple attached to the column of the implant platform. Once the desired implant temperature was reached, the samples were allowed to stand at the specified temperature for approximately 15 minutes to achieve thermal equilibrium prior to implantation. The implant current was kept sufficiently low, that is, less than 2 μAmps on average, to ensure beam heating were kept to a minimum.

Order of implantation

Finally, the synergism of the dual implant process was observed as a function of the order of implantation. Following dual implantation of 1.25 MeV, $5 \times 10^{16}/cm^2$ Si^+-ions and 200 keV Si^+-ions, the order of the implants was altered, such that, the 200 keV ions were implanted prior to the 1.25 MeV Si^+-ions. The energy of the respective high (1.25 MeV)- and medium (200 keV)-energy implants was maintained. The combinations of implants are labeled MeV/keV or keV/MeV to indicate the ordering of the ion energies.

Synergistic response of co-implantation of MeV and keV Si^+-ions

Defect interactions

Fluence of the medium-energy, 200 keV implant, implant temperature, and the order of implantation, were altered to investigate the dynamics of the dual implant process and the interactions driving the final distributions of ion-induced defects. Following high-energy implantation, vacancy defects left in the near surface according to the excess defect model are of interest because of their proximity to R_p of the medium-energy implant. The total damage resulting from the implants was extracted from RBS/channeling spectra utilizing a routine that subtracts a calculated, dechanneled fraction from the original RBS profile to understand the damage from the dual-implant process. This damage extraction routine is detailed in appendix I. The resulting damage profile was integrated yielding an areal density of damage.

The efficacy of recombination of spatially correlated defects is greater at high temperatures due to the increased mobility of the point defects.[97] In addition, thermally-activated coalescence of point defects into clusters or extended defects is also increased at high temperatures. Defect complexes produce a more energetically favorable or stable configuration, thereby reducing the overall lattice energy. Therefore, the synergistic effects explored by the dual implantation experiments involve the kinetic competition between the recombination of complementary defects and self-clustering of the excess defects both of which leave the lattice in a lower energy state. RBS, <100> aligned spectra of samples implanted with 1.25 MeV Si^+-ions and then with 200 keV Si^+-ions to fluences of 1×10^{15} Si^+/cm^2 in figure 17a and 5×10^{15} Si^+/cm^2 in figure 17b at both implant temperatures, 450 and 250° C, are shown. Random and virgin spectra are added

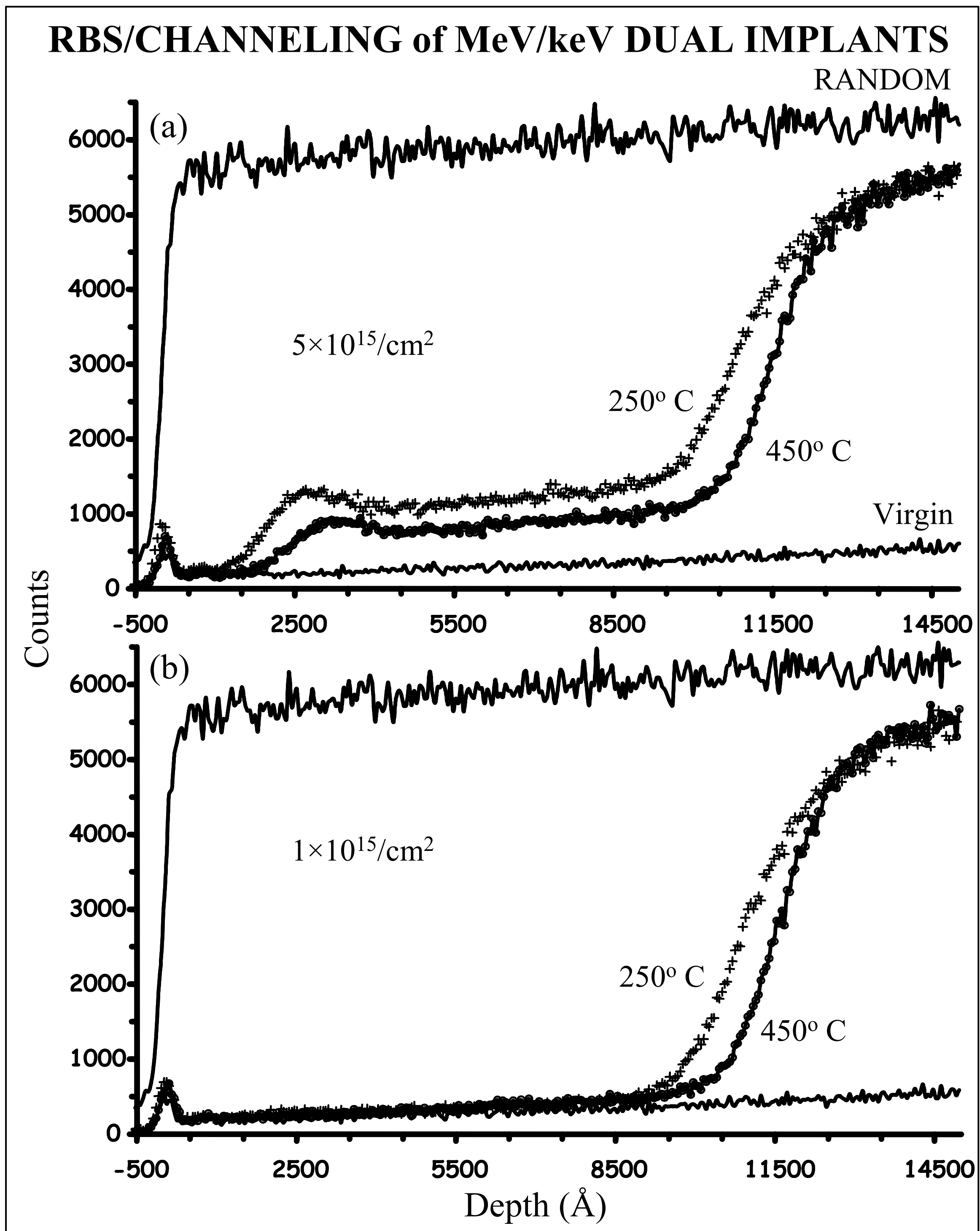

Figure 17. RBS/channeling spectra of Si co-implanted with 1.25 MeV and 200 keV Si^{+}-ions at 250 and 450° C with fluences of (a) $5\times10^{15}/cm^2$ and (b) $1\times10^{15}/cm^2$ of 200 keV ions.

for reference. The random spectrum is an RBS spectrum of a sample that has been rotated continuously to simulate a randomly oriented sample. The virgin spectrum exhibits the RBS/channeling result from unimplanted Si and provides a baseline for identifying implant damage. RBS/channeling analysis of samples implanted with two different fluences of the 200 keV Si^+-ions provided in figure 17 confirms that as the implant temperature is increased, the disorder resultant within the implanted volume is decreased.

A bifurcation of the residual implant damage occurs during the initial high-energy implantation at 1.25 MeV[98], similar to that previously seen from lower energy implants. The separation of the interstitials and vacancies, anticipated from the excess defect model, is clear in both RBS/channeled spectra of samples implanted with 1.25 MeV, $5 \times 10^{16}/cm^2$ Si^+-ions at 450 and 250° C shown in figure 18. The backscattered yield in the near surface of the samples implanted with MeV ions at either 250 or 450° C is similar to the virgin yield. Interstitial damage from the MeV implant is seen in the spectra by the marked increase in the channeled yield in the region centered on the projected range of the MeV ions. The interstitial defect band from MeV implantation is deeper for samples implanted at 450 versus 250° C, possibly due to loss of interstitials at the higher temperature by interdiffusion between the bifurcated regions, i.e. recombination of the complementary excesses.

Reference or control values of the ion-induced damage, following implantation of each fluence were generated. The control represents the disorder present in samples implanted with only 200 keV or 1.25 MeV ions at temperatures similar to those used in the dual-energy implants. A sample with only the MeV implant and individual samples implanted with 200 keV Si^+-ions at each fluence at both implant temperatures, 450 and

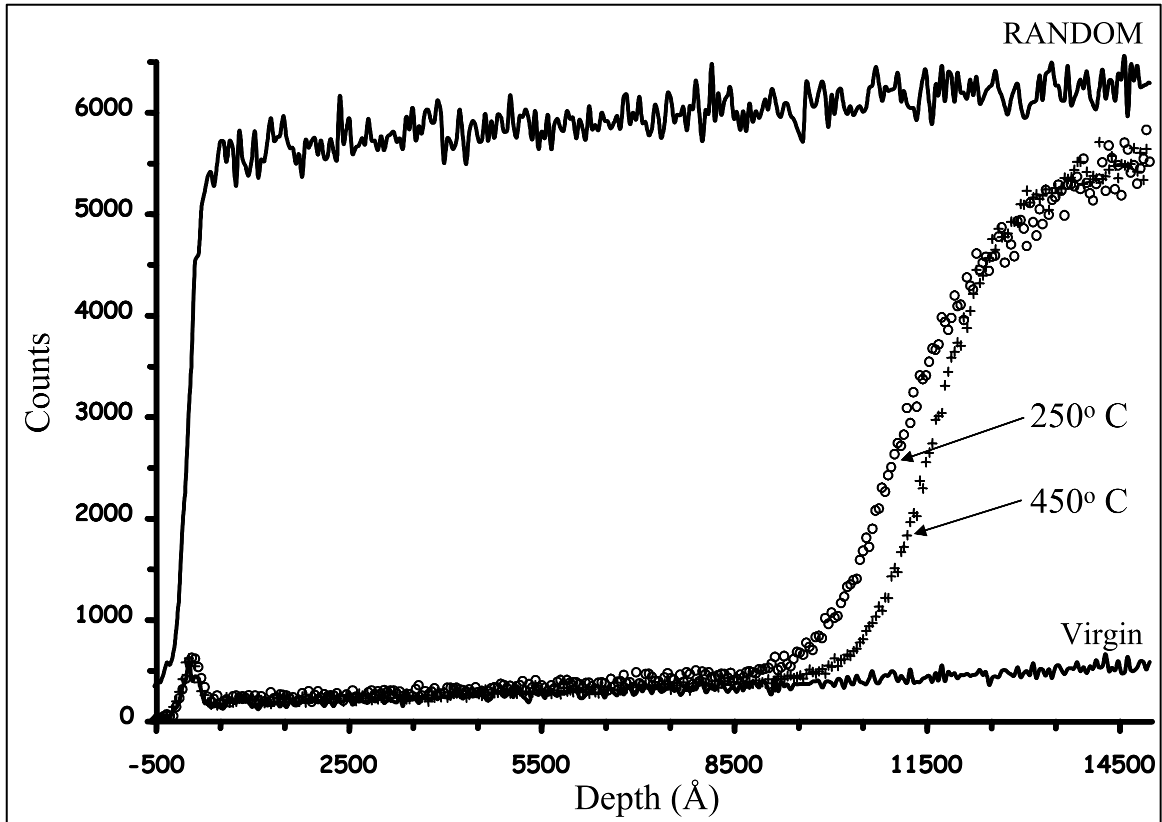

Figure 18. MeV (1.25 MeV, 5×10^{16} Si^{+}/cm^{2}) implanted at 250 and 450° C; respective profiles are indicated by arrows. The 250 and 450° C implanted samples exhibit a clear bifurcation in damage distributions indicating no yield above the virgin level in the near surface region, but a significant rise in disorder at R_p of the MeV implant. The deeper EOR in the 450° C sample versus the 250° C sample is likely due to coarsening of the EOR defects in higher order clusters.

250° C, were analyzed with RBS/channeling. A control curve is established by extracting the damage, which appears in a band near R_p around 2500 Å [see fig. 17]. The damage for each of the 200 keV implants was extracted from <100> aligned spectra and plotted versus fluence in figure 19 for both 250 and 450° C irradiations. Thus, the damage extracted and included in the control curve includes only the damage formed by 200 keV Si implantation. An example of the RBS/channeling spectra for different fluences of 200 keV Si^{+}-ions implanted at each temperature is provided in figure 20. Figure 20a and 20b report RBS channeled spectra containing the disorder versus depth for a few implanted fluences at 450 and 250° C, respectively. All fluences of 200 keV Si^{+}-ions implanted at each temperature are not included in figure 20 for clarity within the figure. The damage obtained from the MeV/keV implants is compared to the control to understand the defect interactions resultant from dual implantation.

Channeled spectra in figure 21, a-h, detail damage distributions for 200 keV Si^{+}-ions implanted at 450° C at each fluence ranging from 1×10^{15} to $1.5 \times 10^{16}/cm^2$ following implantation at 1.25 MeV with 5×10^{16} Si^{+}/cm^2 at 450° C. Figure 22, a-j, shows aligned RBS spectra for all fluences of 200 keV Si^{+}-ions ranging from 10^{14} to $10^{16}/cm^2$ implanted following a similar MeV implant (1.25 MeV, $5 \times 10^{16}/cm^2$ Si^{+}) at 250° C. This implant damage was extracted from RBS/channeling spectra of MeV/keV implants and plotted in figure 23, a and b, versus the fluence of the 200 keV Si^{+}-ions for implants performed at 450 and 250° C, respectively. The second curves in figure 23a (▲) and 23b (△) are the control curves at each implant temperature, seen previously in figure 19.

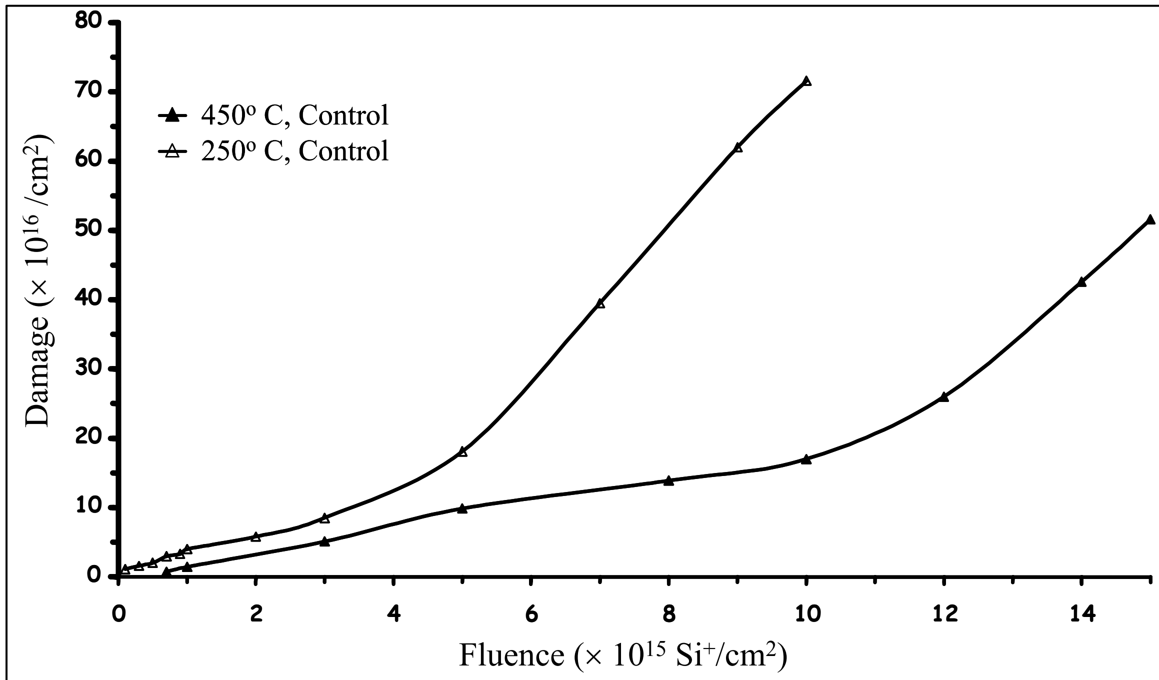

Figure 19. Damage versus implant fluence of 200 keV, Si^{+}-ions for the control samples with only the 200 keV Si^{+}-ion implant.

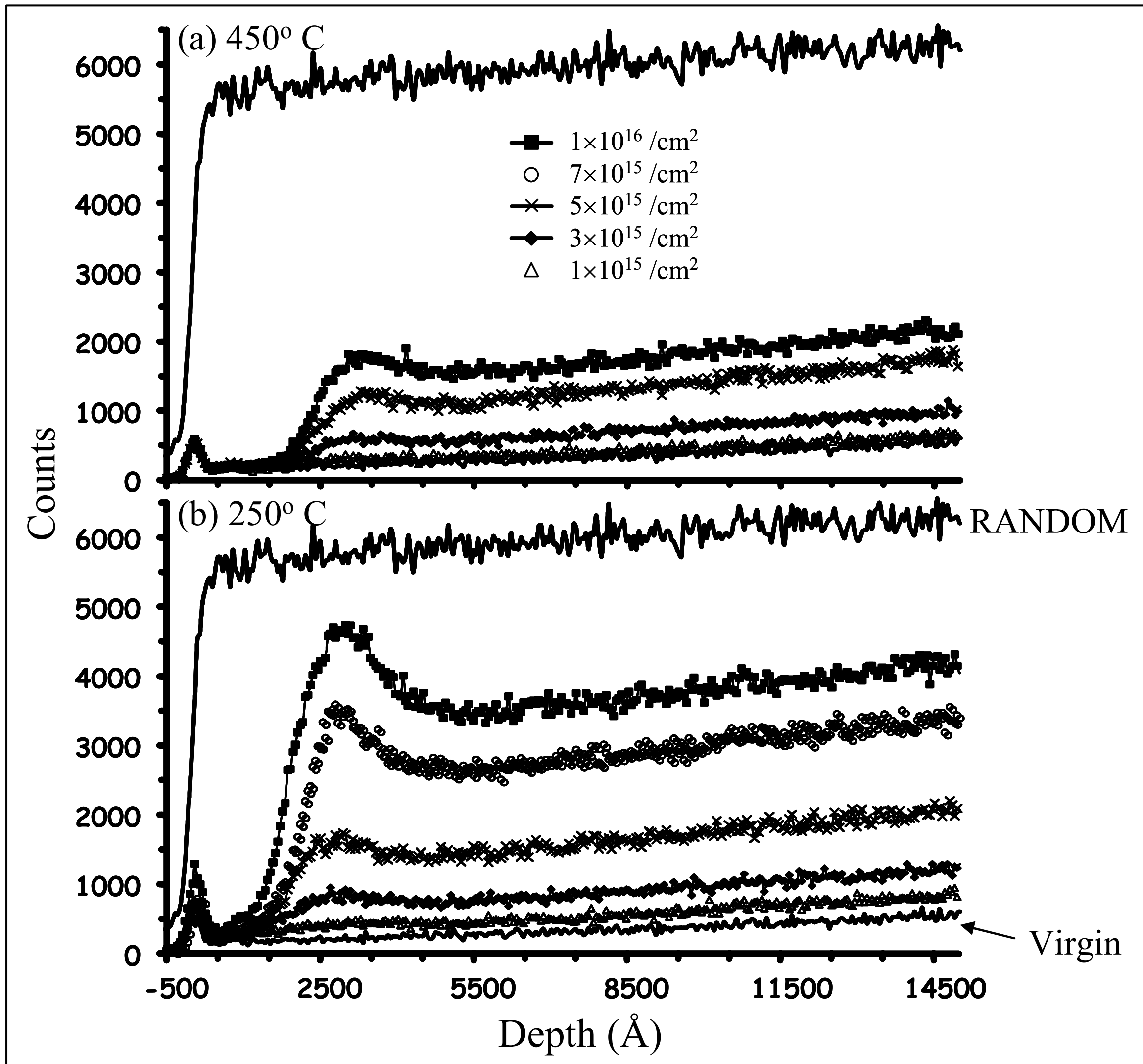

Figure 20. Typical RBS/channeling spectra of samples implanted with 200 keV Si^{+}-ions only at (a) 450° C and (b) 250° C. The damage is decreasing with implant fluence, but the position of the damage peak remains the same.

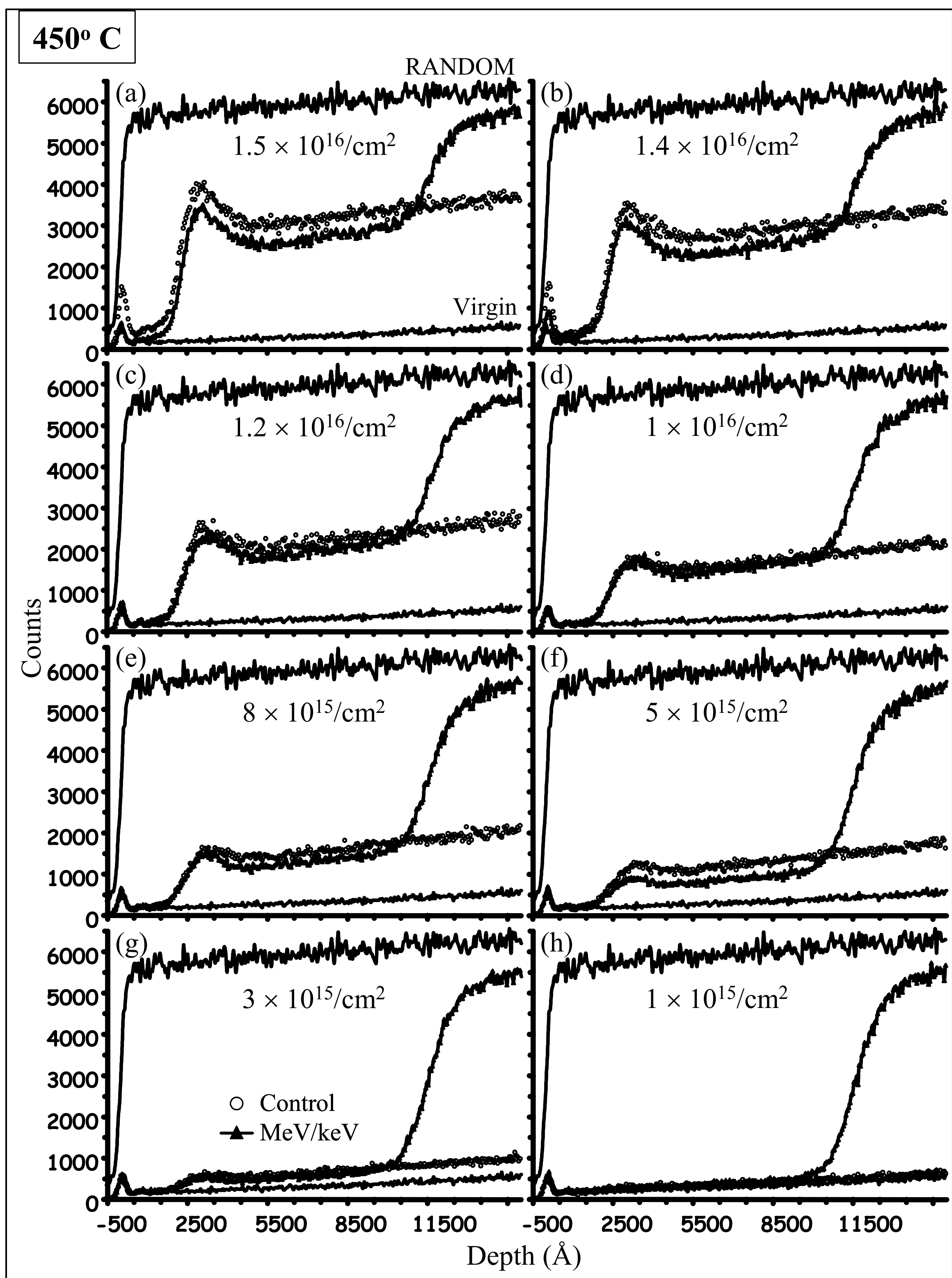

Figure 21. RBS/channeling spectra of 1.25 MeV Si^+-ions implanted with 200 keV Si^+-ions ranging in fluence from 10^{15} to $1.5\times10^{16}/cm^2$ and 200 keV Si^+-ions alone (control curve) at 450° C.

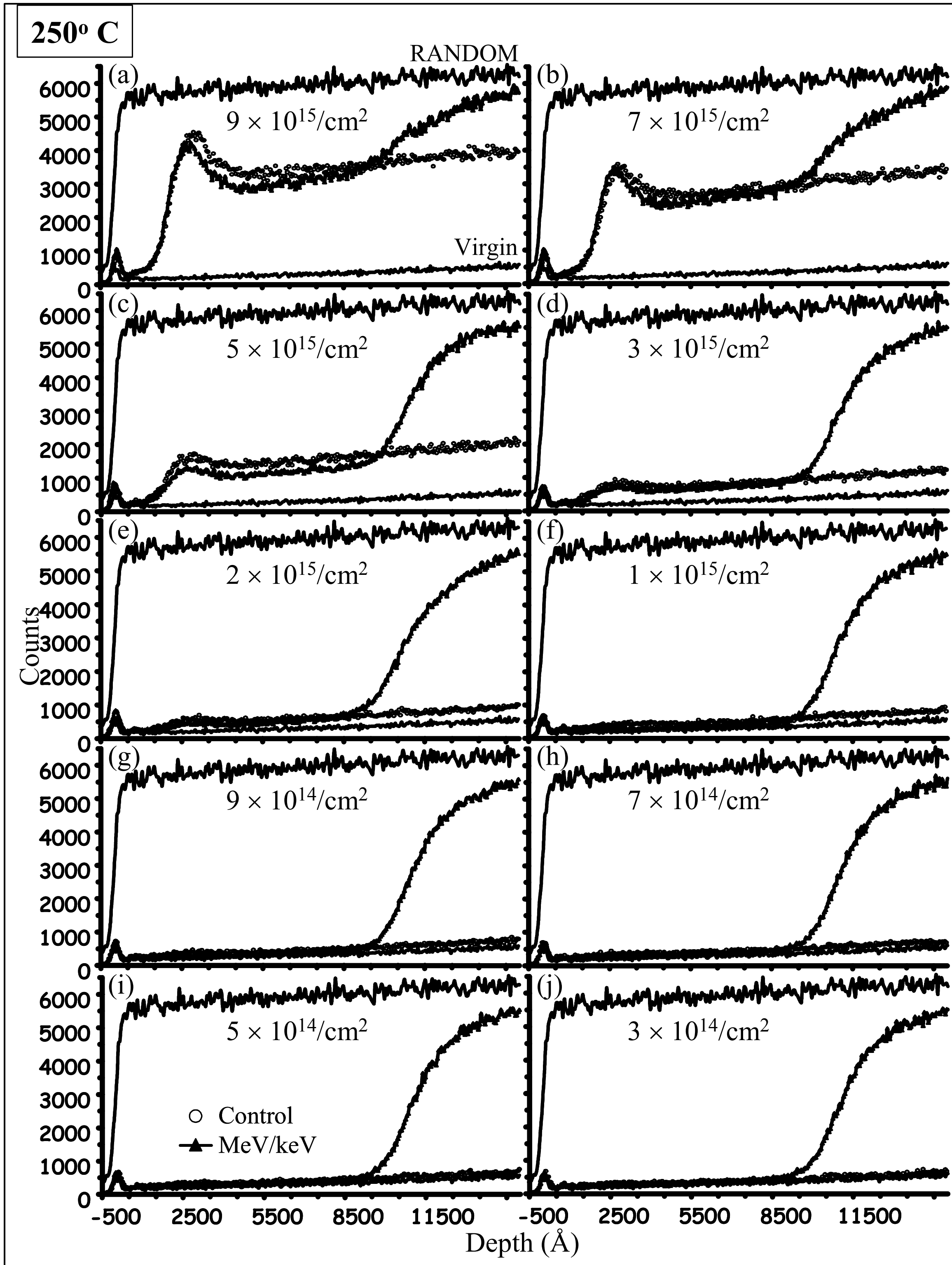

Figure 22. RBS/channeling spectra of 1.25 MeV Si^+-ions implanted with 200 keV Si^+-ions ranging in fluence from 10^{14} to $10^{16}/cm^2$ and 200 keV Si^+-ions alone (control curve) at 250° C.

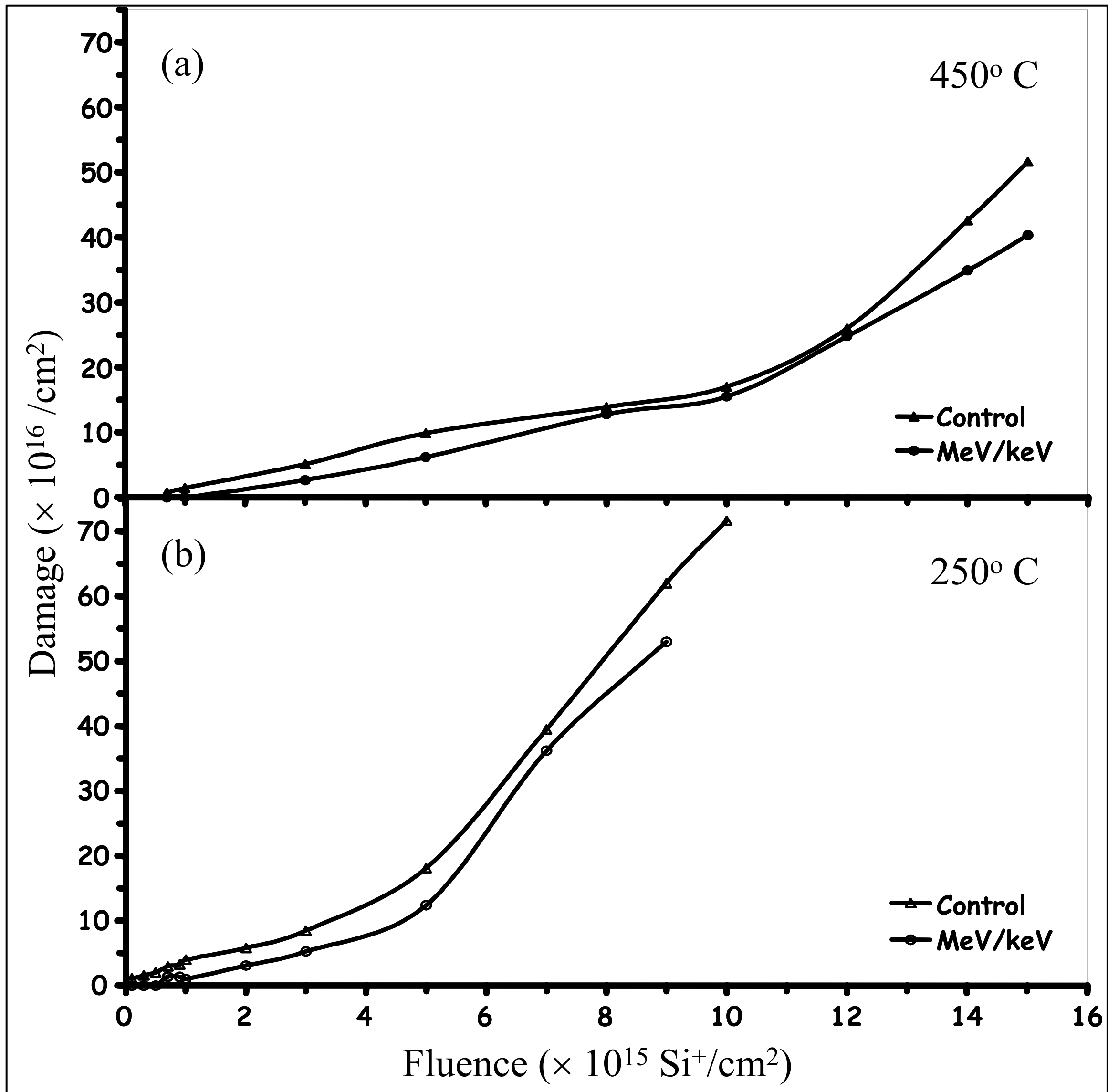

Figure 23. Damage for MeV/keV and control implants versus fluence of 200 keV Si^+-ions at 450° C (a) and 250° C (b). The MeV/keV damage is below the control value over the entire range of implant fluence. MeV Si^+-ions leave a vacancy supersaturation ahead of R_p of the MeV ions. The 200 keV Si^+-ion induced defects recombine with those vacancies to correct some of the disorder.

The damage from the MeV/keV implants is consistently lower than the control values reported for each fluence of 200 keV Si^+-ions implanted at 450 [fig. 23a] and 250° C [fig. 23b]. The MeV/keV damage follows the trend of the control curve throughout the range in fluence of the 200 keV ions. In fact, the curves relating the damage from the MeV/keV implants to the control samples are offset by a constant amount. The mechanism proposed below for the synergism from this dual implantation technique is depicted in figure 24. Consider that the MeV implant injects excess vacancy defects into the near-surface layer with a peak concentration at approximately ½ R_p or half the distance to the projected range of the MeV ions. Following MeV implantation, depending on the processing temperature, the excess vacancy defects form different size clusters.[99] These vacancies may be thought of as "holes" or open-volume defects within this near-surface region. Implanting 200 keV Si^+-ions at 450 or 250° C on top of this vacancy population "fills the holes" left by the MeV implant. When an interstitial and vacancy recombine, the holes are filled and the total ion-induced damage is reduced, thereby lowering the channeling yield in the MeV/keV profiles versus the control values [see for example, fig. 21 or 22]. These vacancy defects provide recombination sites for interstitials injected by the subsequent 200 keV implant. Since the dose of the initial MeV implant remained constant; the number of vacancies available as recombination sites remains constant over the fluence range of the 200 keV implantations. As a result, this leads to a constant offset of a few $10^{16}/cm^2$ as observed in figure 23 between the curves containing the damage extracted from the control and MeV/keV dual implanted samples. TRIM[24] simulations for 1.25 MeV, $5 \times 10^{16}/cm^2$ Si^+-ions implanted into Si in figure 25 corresponds to the condition where the peak of the interstitial excess (from the 200 keV

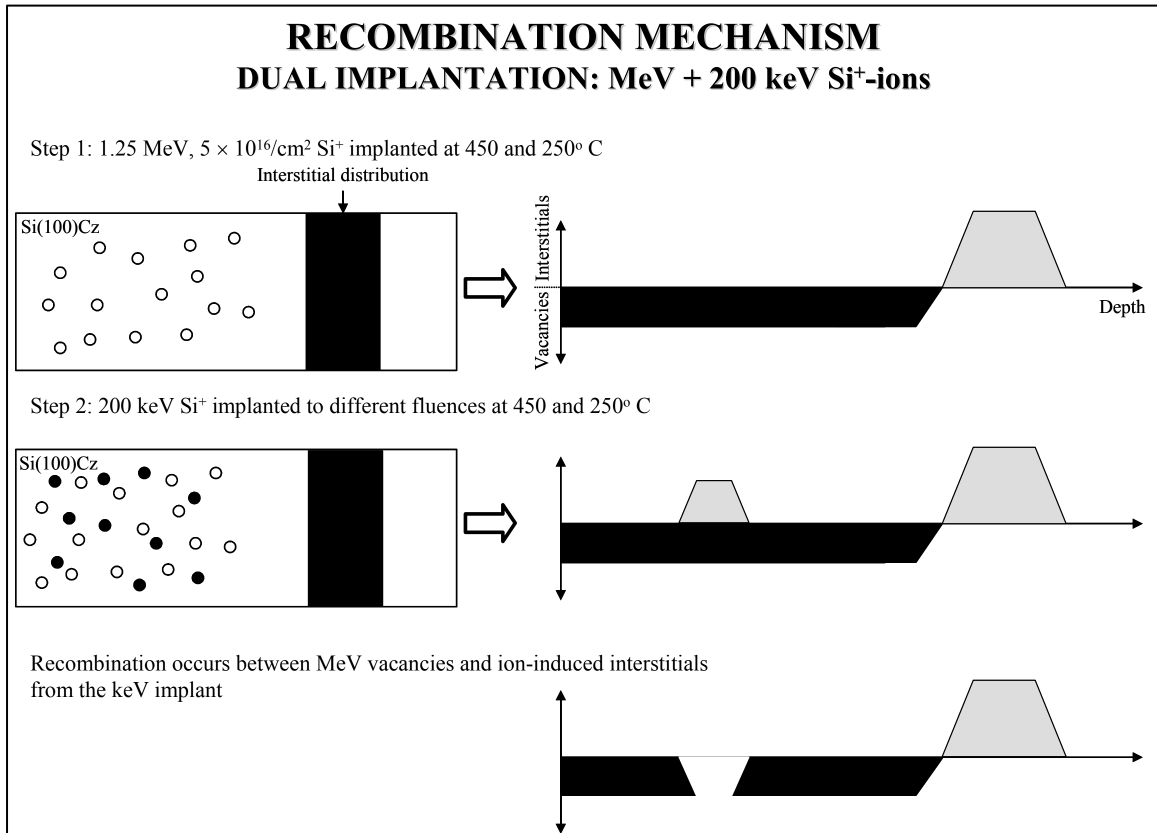

Figure 24. Recombination mechanism for samples dual implanted with 1.25 MeV and 200 keV Si^+-ions. The MeV implant generates vacancy defects or "holes" in the near-surface layer, and the ion-induced defects from the 200 keV Si^+ implant will recombine with those vacancy defects, filling the holes.

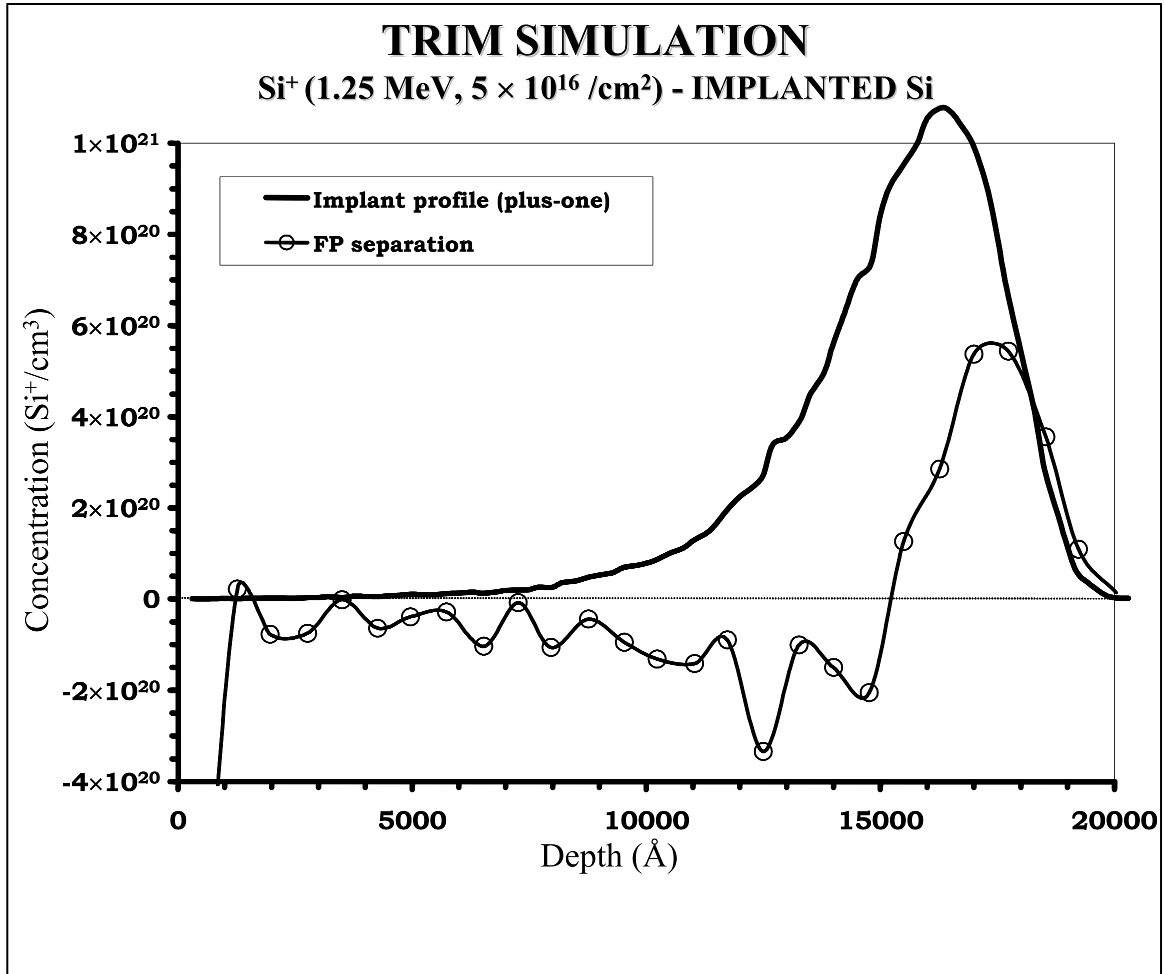

Figure 25. TRIM simulation of 1.25 MeV, $5\times10^{16}/cm^2$ Si^+-ions incident upon Cz-Si. The implant profile was cut off to better illustrate the vacancy region near the surface. The peak concentration of the implant profile is $1.8\times10^{20}/cm^3$.

implant) is equivalent to the excess vacancy concentration generated by MeV ions at ½ R_p. Thus, once the R_p interstitials introduced by the 200 keV ions annihilate the pre-existing vacancies, damage accumulation proceeds similar to that in the control samples. This simple model is consistent with the results, which demonstrates that the damage in the dual implanted samples accumulates similarly to the control but offset or delayed by a constant dose.

Reverse order of implants

In addition to varying the implant fluence of the 200 keV ions and the implant temperature, the order of implants within the dual implantation process was switched. In this case, the 200 keV Si^+-ions were implanted prior to the MeV implant (1.25 MeV, $5 \times 10^{16}/cm^2$ Si^+). Residual damage is plotted versus the fluence of the 200 keV Si^+-ions and compared to the damage from MeV/keV ordered implants and the control in figures 26 for 450° C implants and figure 27 for 250° C implants. Figures 28 and 29 detail RBS/channeling spectra of both MeV/keV and keV/MeV dual implants versus the control. The synergistic behavior observed between the previous dual implants of order MeV/keV did not persist when the order of the implants was altered. Data from samples implanted at temperatures of 250 and 450° C illustrate a reduction of ion-induced implant damage for lower fluences of 200 keV Si^+-ions. For lower keV implant fluences up to $8 \times 10^{15}/cm^2$ implanted at 450° C [fig. 26] and $3 \times 10^{15}/cm^2$ at 250° C [fig. 27], the keV/MeV curve is found below the control. Note that for the lower fluences below $2 \times 10^{15}/cm^2$, 200 keV Si^+-ions, the damage resulting from the MeV/keV ordering were about the same or slightly higher than the damage from implants done using the keV/MeV order. As the fluence of the 200 keV Si^+-ions is increased, the ion-induced

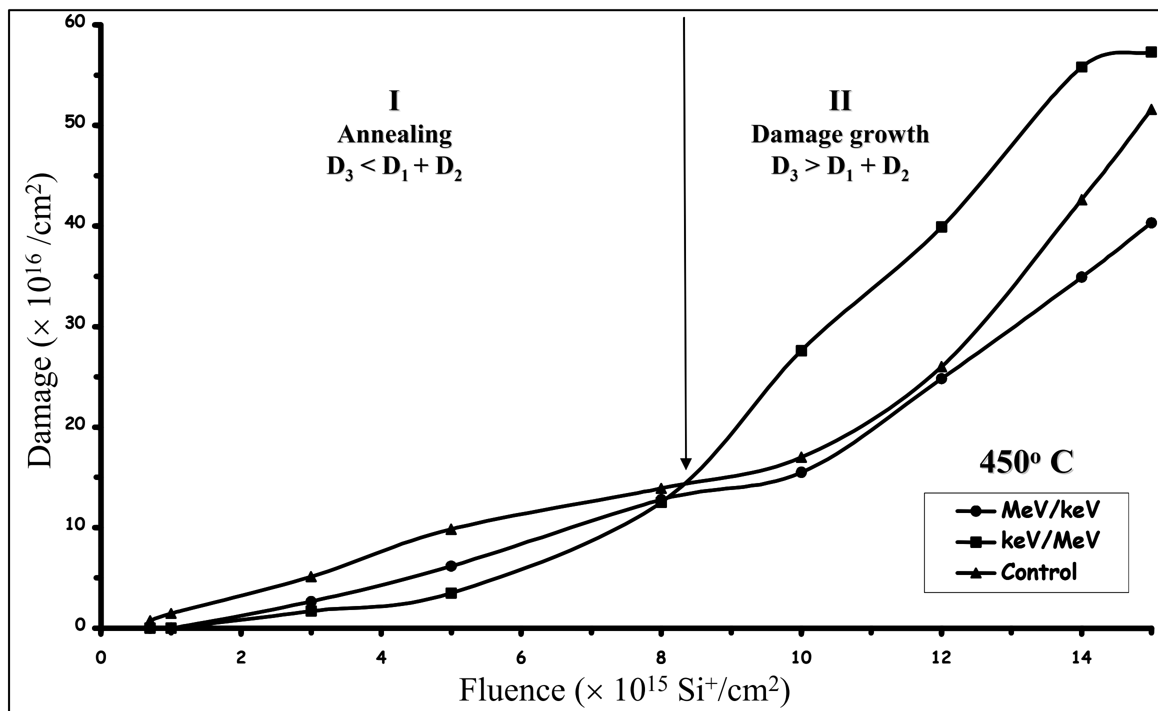

Figure 26. Damage extracted from RBS spectra versus implant fluence of the 200 keV Si^+-ions. MeV/keV curve reflects damage following implantation of 1.25 MeV+200 keV Si^+-ions at 450° C, and keV/MeV shows damage for implants with reversed order of implantation (200 keV+1.25 MeV Si^+-ions) at 450° C. The control contains the damage from implanting 200 keV Si^+-ions alone since no disorder is seen in the near-surface of the MeV implanted sample. Areas of damage annealing and anomalous growth are labeled for the keV/MeV implants. Disorder from the MeV/keV implants remains below the control curve.

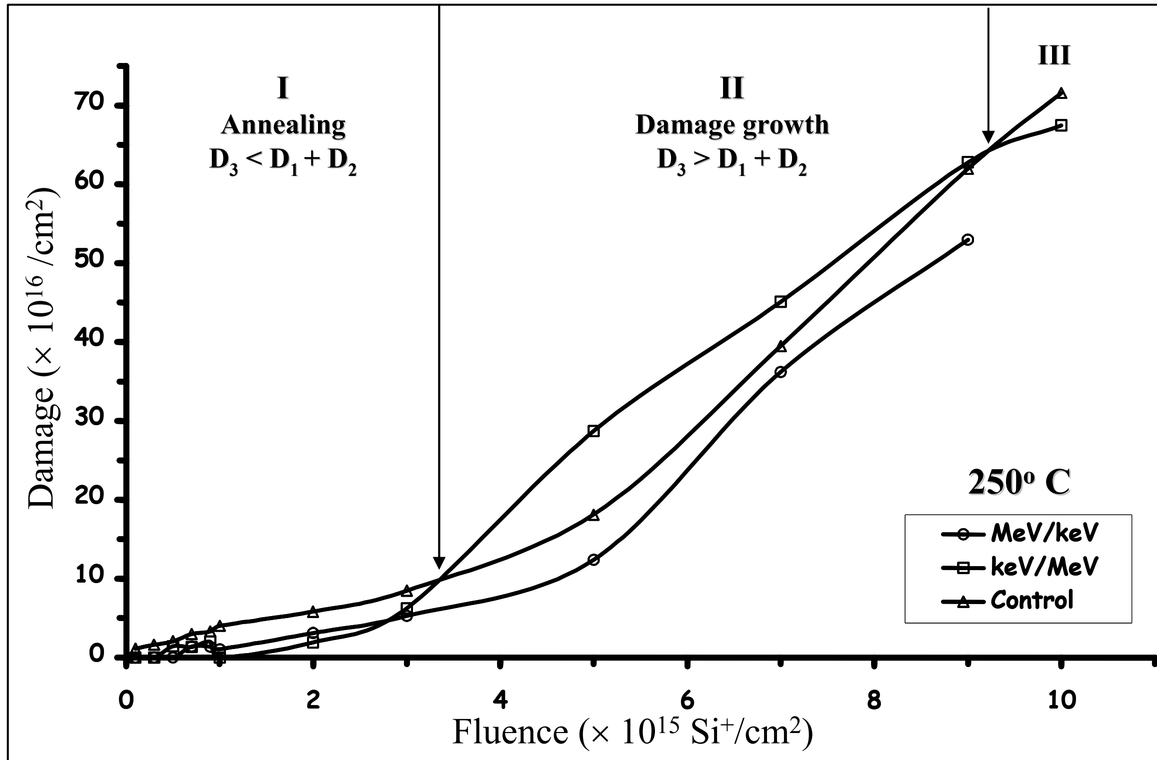

Figure 27. Damage extracted from RBS spectra versus implant fluence of the 200 keV Si^+-ions. MeV/keV curve reflects damage following implantation of 1.25 MeV+200 keV Si^+-ions at 250° C, and keV/MeV shows damage for implants with reversed order of implantation (200 keV+1.25 MeV Si^+-ions) at 250° C. The control contains the damage from implanting 200 keV Si^+-ions alone since no disorder is seen in the near-surface of the MeV implanted sample. Areas of damage annealing and anomalous growth are labeled for the keV/MeV implants. Disorder from the MeV/keV implants remains below the control curve.

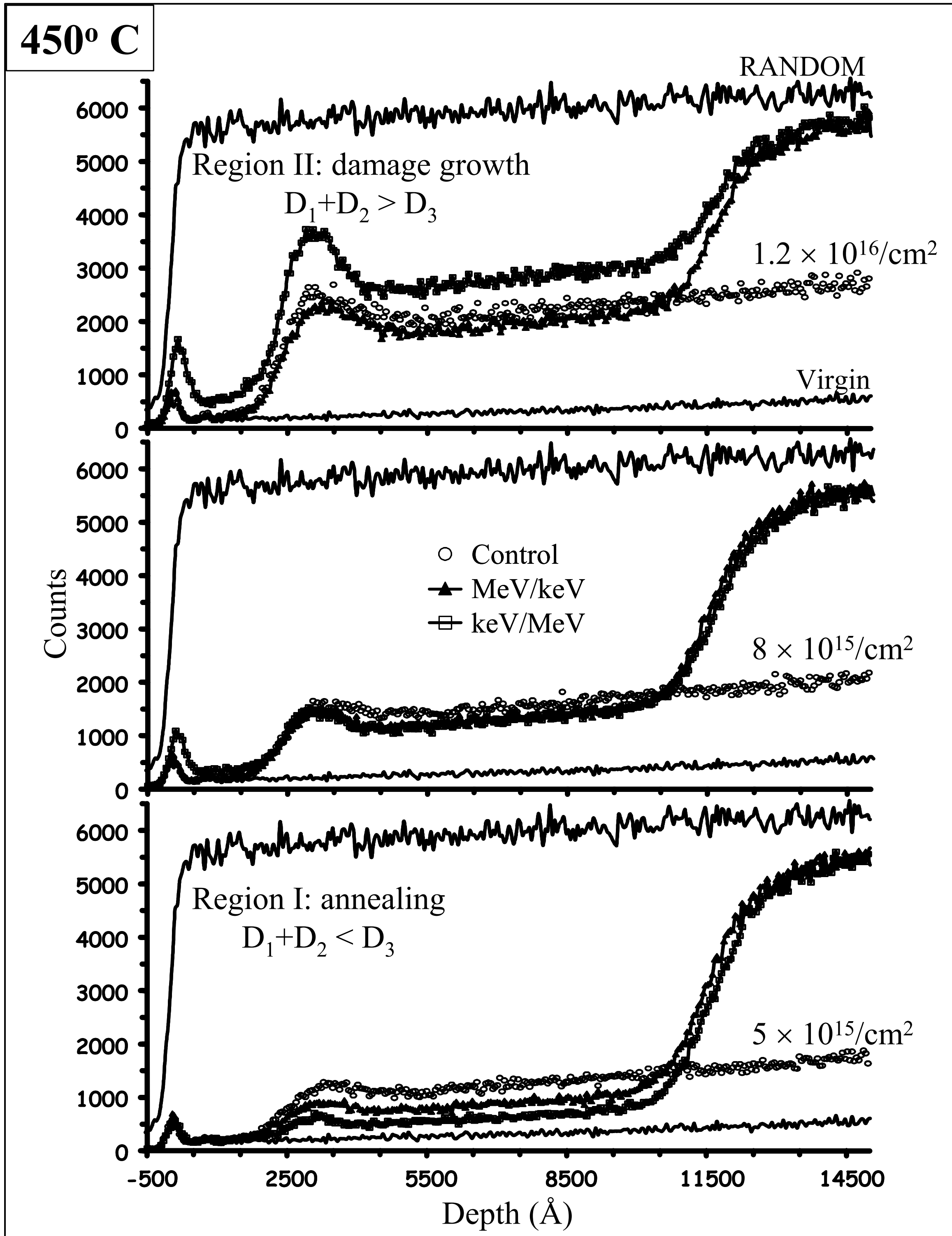

Figure 28. RBS/channeling spectra of MeV ions and 5 and 8×10^{15} and 1.2×10^{16} Si^+-ions/cm^2 both implanted at 450° C displayed in order of decreasing fluence of 200 keV Si^+-ions. The scattering yield for MeV/keV implants is below the control. The keV/MeV implants exhibit damage annealing for the lowest fluence of 200 keV Si^+-ions with a scattering yield below the control but transitions to damage growth for higher fluences of 200 keV Si^+-ions.

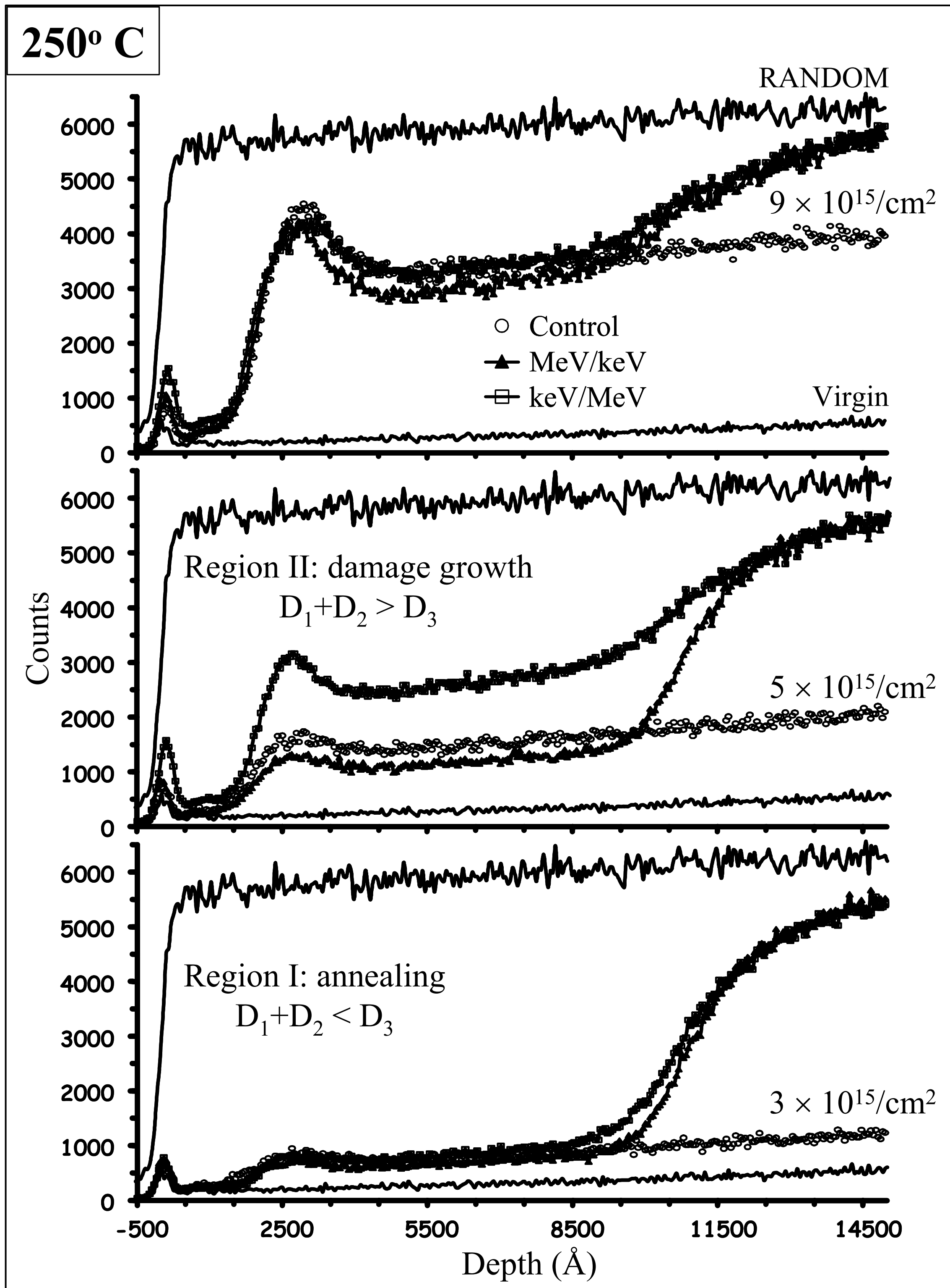

Figure 29. RBS/channeling spectra of MeV ions and 3, 5, and 8×10^{15} Si^{+}-ions/cm^2 both implanted at 250° C displayed in order of decreasing fluence of 200 keV Si^{+}-ions. The scattering yield for MeV/keV implants is below the control. The keV/MeV implants exhibit damage annealing for the lowest fluence of 200 keV Si^{+}-ions with a scattering yield below the control but transitions to damage growth for higher fluences of 200 keV Si^{+}-ions.

damage increases with implant fluence. However, for a critical fluence implanted at either 250 or 450° C, damage growth dominates. Anomalous damage growth is labeled as region II in figures 26 and 27. Following implantation of 8 × 10^{15}/cm^2, 200 keV Si^+-ions at 450° C [fig. 26] and 3 × 10^{15}/cm^2, 200 keV Si^+-ions at 250° C [fig. 27] the damage from implants of keV/MeV order exceeds the damage from implants of opposite order [MeV/keV] and the damage from the control samples. The mechanism for this damage growth is not fully understood. However, a possible explanation may depend upon the details of the damage microstructure as follows. As the 200 keV implant fluence is increased the interstitial defects at R_p cluster to form a dislocation network. At lower doses, simple prismatic loops are formed, which are produced by the coalescence of interstitials into platelets between major crystallographic planes. In this event, the interstitials within the loops readily recombine with the vacancies from the subsequent MeV implant. However, at higher doses, the dislocation network becomes tangled with a more complicated morphology and may no longer be energetically favorable for these defects within this dislocation network to dissociate during subsequent implantation and annihilate with the vacancy defects deposited in the same vicinity from the MeV implant. Thus, significant growth in the implant damage may result in samples irradiated with the MeV ions in samples implanted at doses sufficient to form a more complicated dislocation network.

It is clear that for the injected vacancy concentration, around 1 × 10^{20}/cm^3, used in this study, the recombination between MeV vacancies and keV interstitials dominated during the MeV/keV sequential implants. However, keV/MeV implants produced some unexplained anomalies. It would appear that for a lower fluence of the medium-energy

ions, the excess interstitials remained in small clusters or loops, which can be dissociated and annihilated through recombination with subsequently injected vacancies. However, at higher doses, these interstitials form more complex configurations (i.e., extended defects such as dislocation networks) that resist recombination and actually grow from the release of interstitials from smaller loops or interstitial clusters.

Summation: Excess defect model supported

A direct and simple example of the effects of the excess defects was detailed by the first experiment, see section "Damage profiles versus implant temperature", which compared residual ion-induced damage at various temperatures to TRIM simulations of the damage profiles. TRIM[24] simulations were compared to damage from 150 keV Si^+-ion implants at both LN_2 and 300° C. Good agreement is achieved between the excess defect distribution from the TRIM simulation and the channeled profile of the 150 keV Si^+-ion implant performed at 300° C, while the implant at LN_2 was modeled with the total number of displacements.

Essential corroboration of the excess defect model follows from confirmation that the co-implantation of high- and medium-energy Si^+-ions produces a vacancy-rich layer in the near surface left by an MeV implant to interact with and anneal the ion-induced interstitial defects from subsequent implantation of 200 keV Si^+-ions. The synergism observed within these co-implanted species was reported as a function of implant temperature, fluence of the medium-energy implants, and the order of implantation. From the model, it was anticipated that implanting MeV ions prior to 200 keV ions predamages the lattice with vacancies in the near surface region and interstitials beyond the projected range of the MeV implant. Subsequently implanting 200 keV Si^+-ions into the vacancy-

rich region influenced recombination between the ion-induced interstitials and the pre-existing vacancies. Subsequently implanting 200 keV Si^+-ions, fills the ‘holes’ left by the MeV implant before inducing any damage accumulation.

A somewhat more complicated mechanism was observed upon switching the order of implantation. Anomalous damage accumulation is realized when the order of the implants is reversed. Clusters of interstitial defects are probably formed following implantation of the 200 keV Si^+-ions prior to any injection of vacancy defects into this region. This growth in the damage is not fully understood, but may be attributed to a dense dislocation network that forms, which preferentially sinks the interstitials (rather than vacancies) produced during subsequent implantation.

The ability of the model to predict damage that survives implantation and a post-implant anneal was validated. Employing this new excess defect model along with tools such as high-energy ion implantation, pre-amorphization, or dual high- and low-energy implantation enables novel manipulations of defect excesses to be developed. Such techniques are generally labeled as defect engineering, and will be accomplished through application of this new excess defect model, which establishes a new paradigm for understanding both ion-induced damage formation and mechanisms for manipulating such damage to yield engineered properties.

CHAPTER 6

PREDICTIVE NATURE OF MODEL: DEFECT ENGINEERING

Introduction

Excess defects described previously were shown to result is a different spatial distribution than the total defect population produced by the interaction of energetic ions with matter. Such differences make it imperative that the effects of excess defects on such phenomena as impurity diffusion, defect annealing, etc, be understood, as well as the conditions under which these effects occur. To this end, the model was validated and detailed in the previous chapter, as well as its range of applicability. Positron annihilation spectroscopy (PAS) data confirmed the presence of excess vacancies in the near surface layer, which survive higher temperatures, especially in silicon-on-insulator (SOI) material versus bulk Si [refer to fig. 13]. Excess interstitials were shown to be located below the excess vacancies just beyond R_p, the projected range of the implanted species.

Novel defect-engineering methods based upon the excess defect model, to suppress or remediate the effects of ion-induced defects will be presented in this chapter. Defect engineering often employs the use of a second implant as a tool to eliminate or reduce defects produced by the primary. In such a case, the subsequently implanted ions are used solely to mitigate or suppress the deleterious effects of lattice damage produced by the primary beam. In the absence of such efforts, high-temperature annealing is used following implantation to eliminate or reduce the ion-induced defect concentration.[97] Such methods can provide substantial engineering tools for processing Si, as well as further establish the importance of the model in describing ion-solid interactions. The process of defect engineering has gained popularity since the early 1990's. Aggressive

trends in the design rules consistently demand better control over the distribution of ion-implanted impurities to form shallow electrical junction depths and limit lateral impurity diffusion. Therefore, knowledge of defect distributions and defect-impurity interactions has become a priority in both research and processing efforts.

Also, implantation at high-temperature allows for more efficient recombination or dynamic annealing of the defects at temperatures far below those typical for post-implant annealing procedures, thereby saving on thermal budgets.[100] Thus, the number of residual or secondary defects might be decreased or the complexity of their configuration reduced following ion implantation. However, such methods have not provided the control over dopant profiles necessary for the aggressive design rules for Si processing. Thus, exploring the engineering of ion-induced defects through ion beams or the actual implant could impact device processing time or the number of process steps.[101] Much success has been reported in the field of ion beam defect engineering (IBDE)[28,102] and the manufacture of SOI material through separation by implantation of oxygen (SIMOX) processing.[103,126] Wang, et al. used IBDE techniques to reduce secondary defects from a shallow implant. The end-of-range (EOR) defects from a subsequent MeV implant acted as a gettering center for defects which otherwise might contribute to high impurity levels, anomalous dopant diffusion, or the formation of stable defect complexes near desired junction depths.[28] High-energy, -temperature, and –dose implantation have been employed to create SOI material by the SIMOX process.[103]

To meet the challenge of aggressive design rules (for Si-based microelectronics) primarily requires the ability to form ultra-shallow electrical junctions by ion implantation. To this end, both the broadening due to ion-channeling during implantation

and dopant diffusive during post-implantation annealing must be controlled. This redistribution of the dopant profile due to both these effects is undesirable because it increases the depth of the implanted profile and, hence, the depth of the electrical junction. Transient-enhanced diffusion (TED) of some ion-implanted dopants is usually observed during post-implantation annealing and greatly exasperates the problem of forming shallow junctions. TED greatly enhances the redistribution of dopants over intrinsic diffusion processes but is transient in that it decreases rapidly with time. It has been shown that the presence of ion-induced defects within the implanted region is the source of TED.[104] The presence of excess vacancies or interstitials will impact corresponding elements that diffuse by either vacancy or interstitial mechanism (e.g., antimony or boron, respectively) or those that diffuse by a fraction of each mechanism (e.g., arsenic).[32]

TED of a dopant such as boron, an interstitial diffuser[32], is known to result from ion-induced interstitials formed when B^+ is implanted directly into Si. These excess interstitials within the implant volume cluster to form {311} defects or elongated, interstitial-type defects extending along the (113) plane. Previous experiments[105] have conclusively established {311} defects as the dominant defect contributing to TED of dopants, such as boron, implanted into crystalline Si. During thermal annealing, the {311} defects or defect clusters[106] dissociate by releasing interstitials which then are available to interact with the B^+ resulting in an enhanced diffusivity.[105,106]

Specifically, defect engineering will be employed to control excess defect populations believed responsible for processes, such as TED. Methods of defect engineering include overlapping complementary excess defects, to promote their

elimination by recombination of the defects. High energy ion implantation may inject vacancy or interstitial defects can be injected at lower energies to manipulate the excess defect concentration from a primary implant. This technique was demonstrated in the previous chapter using dual ion implantation both prior and subsequent to the thermal annealing stage. These previous examples were presented as evidence for the excess defects and their bifurcation into distinct distributions of vacancies within the near-surface and interstitial defects beyond. In this chapter, experiments will be presented that utilize defect engineering techniques based on the "excess-defect" model to target a specific problem encountered in fabrication of Si microelectronics. As a reminder, it should be clear that all experiments are designed according to the details of the excess defect model, i.e., excess defects come from three sources; spatially separated Frenkel pairs, extra atoms corresponding to the implant dose (the plus-one contribution[23]), and sputtering of the surface. These contributions are illustrated in figure 30 for TRIM[24] at 1.25 MeV Si^{+}-ion implantation. The model is applicable over a range of parameters. This model addresses energy ranges from a few keV to several MeV, as well as, moderate ($10^{14}/cm^2$) to high ($10^{18}/cm^2$) implant fluences. Results from three experiments will be discussed. Each is designed to demonstrate the use of techniques derived from the excess defect model to engineer lattice defects produced by different implant conditions. The efficacy of the results will further reveal the value of the model.

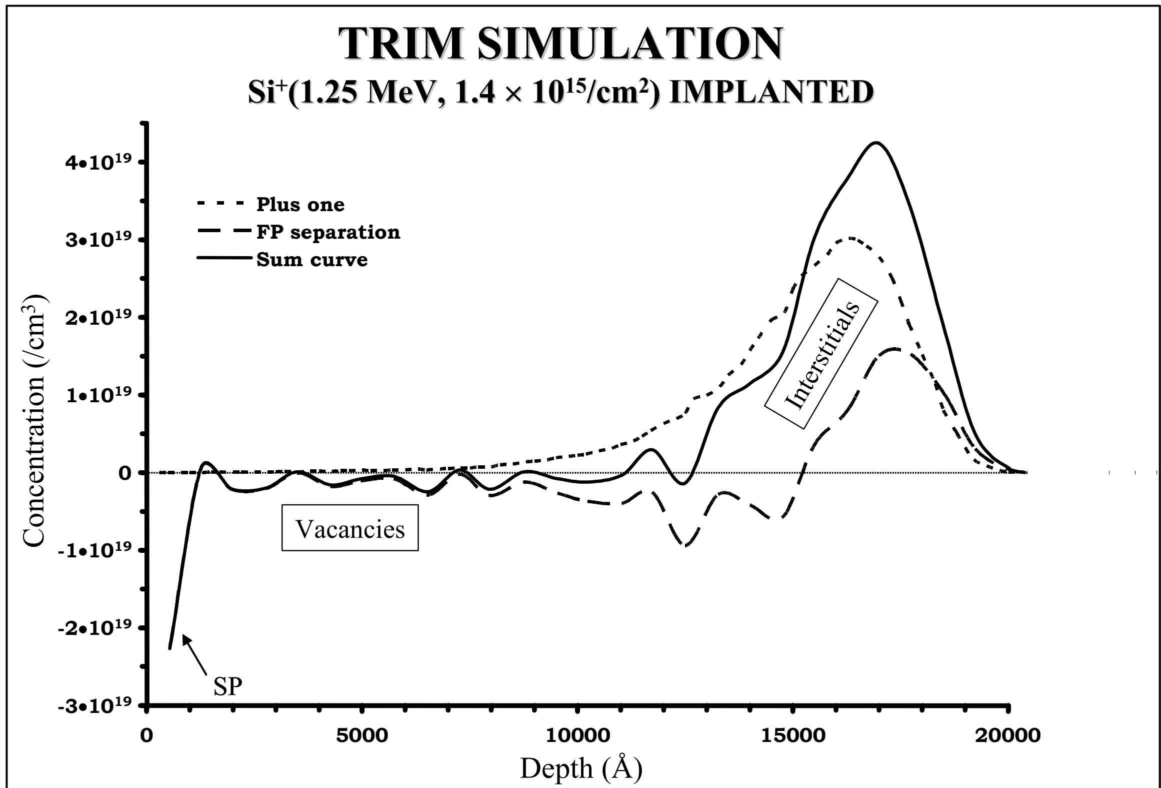

Figure 30. TRIM simulation of 1.25 MeV, 1.4×10^{15} Si^{+}/cm^{2} implanted into Si illustrating distributions of excess defects that combine for overall vacancy and interstitial regimes. Reprinted with permission from E. G. Roth, O. W. Holland, and D. K. Thomas, *Appl. Phys. Lett.* **74**(5), 679, Copyright 1999, American Institute of Physics.

Experiment I: Suppression of TED of implanted B^+

Discussion

Experiments evaluating the ability of an amorphous layer to inhibit the redistribution of the dopant profile due to TEM during post-implantation annealing were studied. However, results using traditional pre-amorphization to prevent TED of boron marker layers have varied between those which show the elimination of TED[107], to others that indicate no change in TED.[108,109] The difference apparently depends upon the magnitude and configuration of the EOR defects left below the a-c interface. Therefore, an objective of this work is to gain a better understanding of the source of interstitials that contribute to TED in pre-amorphized Si. Methods to either control or eliminate these sources of defects will be explored.

Two experiments were devised to engineer the EOR defects directly. The first experiment makes use of pre-amorphization of the Si lattice as a means to control any broadening of the profile due specifically to channeling of the ions implanted into crystalline material. Light ions (e.g., boron) may penetrate the lattice and travel to a depth beyond what was intended when they travel within the channels of the substrate.[1] Channeling of light dopant ions, such as boron, is eliminated when the boron distribution is positioned within an amorphous or random volume due to the absence of channels in the amorphous substrate.[110,111] Reduction of junction depths by as much as 1500 Å immediately following implantation processing is realized, as detailed in figure 31 containing initial profiles of a 40 keV, $10^{14}/cm^2$ boron implant in both pre-amorphized and crystalline Si.

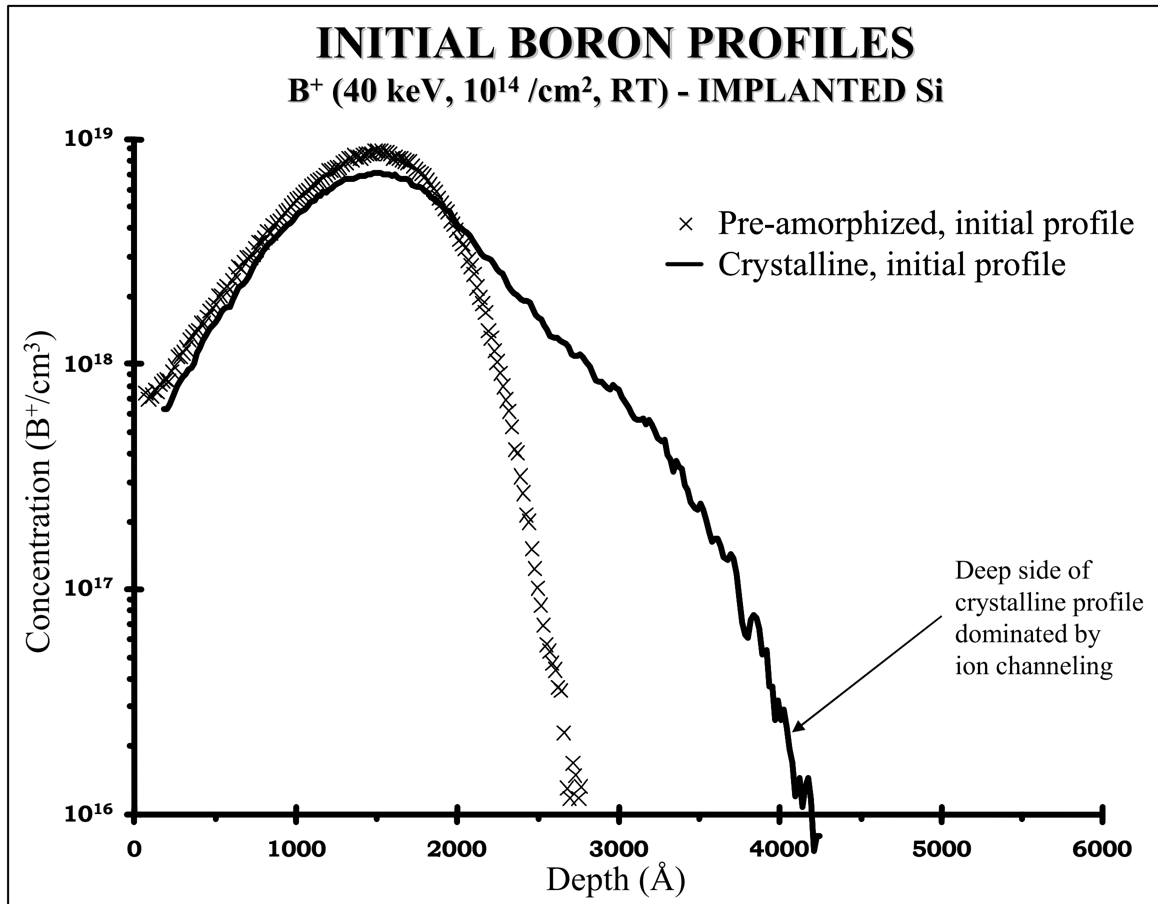

Figure 31. SIMS profiles of 40 keV, 10^{14} B^+/cm^2 implanted into fz-Si(100) and pre-amorphized Si at RT. The depth of the light dopant ion in crystalline Si is dominated by a deep channeling tail that extends about 1500 Å further into the lattice past the depth of the B^+ implanted into pre-amorphized Si.

Pre-amorphizing the lattice was also performed in the hope that it would eliminate the R_p defects, which contribute to enhanced diffusion upon post-implant thermal treatment of the lattice. At a sufficient dose, damage from Si^+ self-ion implantation produces an amorphous layer at the surface that can be made arbitrarily thick by adjusting the ion energy to fully contain a subsequent boron implant. Boron was chosen as the dopant in this study because it is used ubiquitously for p-type doping and it diffuses predominantly by an interstitial mechanism.[32] Limiting the implanted dopant distribution to the amorphous layer constrains the ion-induced displacement damage to the amorphous layer. Given the inherent random environment within the amorphous layer, the displacement damage does not lead to any morphological changes within the layer, and therefore no damage accumulation. Also, the flexibility of the amorphous layer in accommodating different bonding configurations enables the assimilation of implanted ions following regrowth of the layer; dopant atoms are incorporated onto substitutional sites without any residual damage except at the original a-c interface.[3,92] Consequently, the activation of the dopant during annealing is nearly one hundred percent efficient per the complete incorporation of boron onto lattice sites during SPEG.

The second technique proposed used high-energy ion implantation to selectively inject a vacancy excess sufficient to recombine with plus-one interstitials from a subsequent dopant implant. The goal in engineering complementary excess defect profiles to overlap was the annihilation of those defect excesses. As such, the interstitial type defects responsible for the TED of boron would be eliminated. High-energy implantation generates a preponderance of vacancy defects ahead of the interstitials deposited at the projected range of the energetic ions.[20] Co-implantation of boron and

high-energy Si^+-ions included using the vacancy excess near the surface from the high-energy implant to initiate local recombination with ion-induced interstitials from the B^+-implant. In order to reduce or eliminate the interstitial defects following dopant implantation, the dopant is introduced at an energy necessary to position R_p of the dopant implant at the depth of the highest concentration of vacancy defects. TED of the B should be reduced or eliminated if B^+-induced interstitials recombine with the vacancy component instead of contributing to redistribution of the dopant.

Experiment

Substrates used in the first experiment where a dopant implant was introduced entirely within an amorphous layer consisted of B doped, float-zone (fz-) Si (100) samples with resistivity of 2500-3500 Ωcm. Fz-Si(100) was used because it contains impurities, such as oxygen known to interact with defect species. The goal was to only investigate damage resulting from the implant process without concern for interactions between impurities.

An amorphous layer was generated in the samples prior to introduction of the dopant ion. The samples were amorphized by implanting $^{30}Si^+$ self-ions. The energy of the amorphizing implants remained constant throughout this experiment. Dual implants of 70 and 140 keV $^{30}Si^+$-ions implanted at either - 50° C with a fluence of $6 \times 10^{14}/cm^2$ or RT with a fluence of $1 \times 10^{15}/cm^2$ generated an amorphous layer. These fluences were necessary to create an amorphous layer continuous to the surface. Different amorphization conditions, such as energy, fluence, and temperature, were used to modify the EOR defects below the a-c interface, so their effect upon dopant diffusion could be investigated. Varying the temperature of the amorphizing implant altered both the

magnitude and microstructure of the excess defects below the a-c interface. Both implant conditions amorphized the silicon continuously to the surface, as was confirmed by RBS/channeling analysis. Boron implants were performed at RT with an energy of 40 keV to a fluence of $10^{14}/cm^2$. The samples were tilted 5 degrees off normal, with respect to the incident beam, in an effort to suppress channeling of the implanted ions. Finally, the boron was diffused using a conventional, quartz-tube furnace with argon ambient at either 800 or 1000° C for 15 minutes.

SOI material prepared by a wafer bonding and etch-back process to have a top Si layer of ~1 μm of Cz-Si (100) was used in the second experiment for the suppression of TED of boron using the co-implantation technique. The layered morphology of SOI material was used to inhibit defect fluxes, so the interstitial defects from the MeV implant were deposited well beyond the Si/SiO_2 interface. High-energy implants of differing fluence were performed prior to the boron implant. Samples were co-implanted with 2 MeV Si^+-ions implanted at RT with fluences of 1 and $5 \times 10^{18}/cm^2$ and then with 40 keV, 10^{14} B^+/cm^2 at RT. An 800° C, 15 minute anneal was performed on the samples in a conventional furnace within an argon ambient. Boron profiles for all of the samples were obtained using secondary ion mass spectrometry (SIMS) analysis with an O^+ primary beam. Rutherford backscattering (RBS)/channeling measurements with a 2.3 MeV He^{++} ion beam utilized a standard surface-barrier detector positioned at 160° to intercept the backscattered ions.

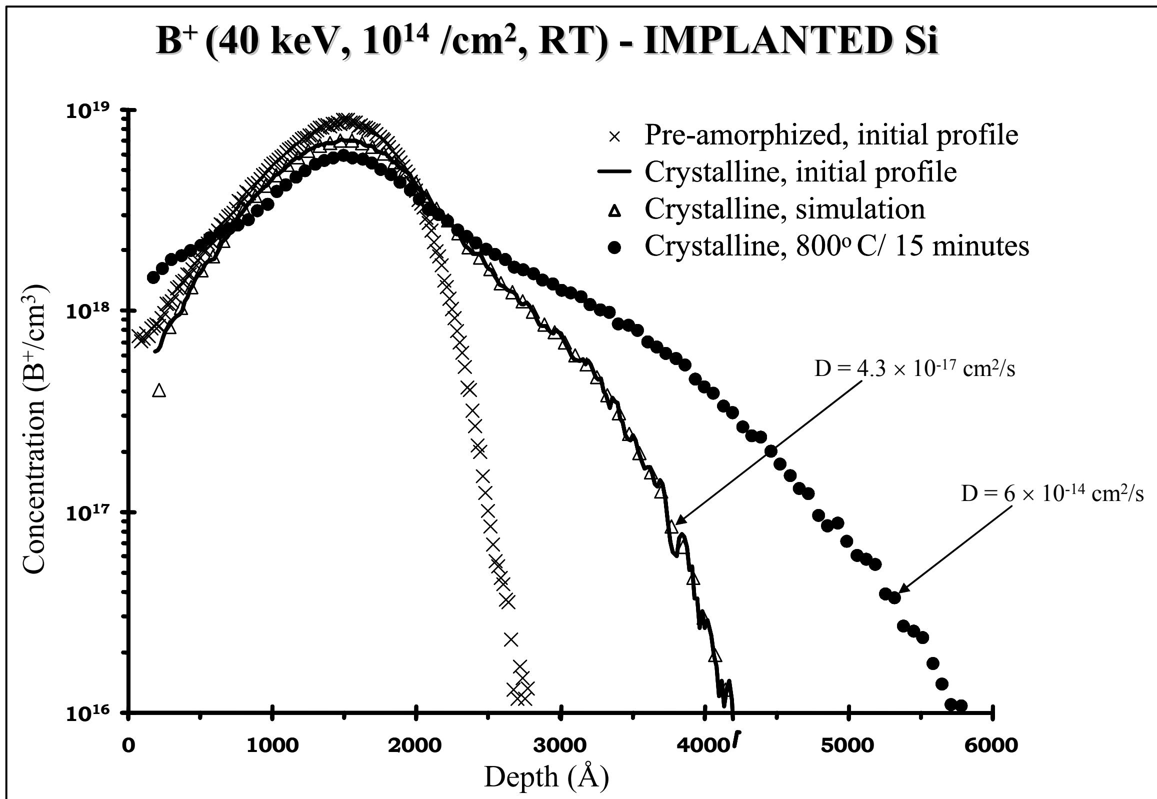

Figure 32. SIMS profiles of 40 keV, 10^{14} B^{+}/cm^{2} implanted into fz-Si(100) and pre-amorphized Si at RT. The depth of the light dopant ion is significantly reduced, about 1000 Å, due to the reduction in the channeled tail for B^{+} implanted into pre-amorphized material. After thermal processing at 800° C for 15 minutes, the boron profile has diffused approximately 1500 Å beyond the initial junction depth. A finite element analysis (△) and an initial profile are shown for comparison. It is noted that little or no movement of the boron should occur for this time and temperature of processing.

Results

Model predicts EOR interstitials-consistent with B^+ diffusion

Dopant profiles in figure 32 from Si(100) samples implanted with B^+-ions only illustrate the magnitude of the enhanced diffusion caused by ion-induced defects. The profile after processing at 800° C for 15 minutes extends considerably beyond its initial (as-implanted) state. The diffused boron profile extends about 1500 Å beyond the as-implanted profile. A finite-element analysis, as described in ref. 112, demonstrated that this diffusion was clearly enhanced over the tracer value (which predicts essentially no movement of boron at this time and temperature). The diffusivity extracted from this analysis was 6×10^{-14} cm^2/s, which is almost three orders of magnitude greater than the tracer value, 4.3×10^{-17} cm^2/s at 800° C.

It is interesting to note that much of the initial penetration of the boron profile into the crystalline sample is due to the effects of channeling upon the as-implanted profile. This is evident when the initial distribution in crystalline Si is compared to that from a pre-amorphized sample in figure 32. Channeling obviously occurs in the single-crystalline sample despite the use of a five-degree tilt during implantation. Channeling is a particular problem for light-ion implantation since the damage to the lattice is minimal at RT and, thus, does not inhibit this effect (i.e., the lattice essentially remains crystalline). The channeling tail in the initial profile in the crystalline material extends about 1500 Å beyond the as-implanted profile from the pre-amorphized sample [fig. 32]. This is almost identical to the in-diffusion, observed in the sample pre-amorphized at -50° C, caused by the transient at 800° C. Thus, it is clear that the task of forming shallow junctions is affected by a number of factors related to ion-solid interactions, including

crystallinity of the substrate, energy of the penetrating species, implant temperature, and implanted fluence to name a few.

Another interesting phenomenon exhibited in the profiles in figure 32 is the immobile boron peak near the ion range, 1550 Å. This complexing of boron was observed previously and explained to be clustering of substitutional boron with boron interstitials.[113,114] These complexes are rather stable and immobilize the boron at a relatively low annealing temperature (i.e., about 800° C). There was some uncertainty as to the nature of the immobile boron, specifically whether or not the boron is electrically active. Ref. 115 suggested that a high fraction of this boron is electrically active, while the B_S-B_I cluster model[113,114] assumes it is not. Note that B represents a boron atom and I an interstitial. The concentration of implanted boron differed widely between these different experiments. However, the problem was clarified by L. Pelaz and coworkers at Bell Laboratories, Lucent Technologies.[116] The investigation in ref. 116 confirmed that the boron in the clustered region is indeed electrically inactive.

Pre-amorphizing the sample prior to dopant implantation has indeed been shown to be effective in eliminating ion-channeling effects, clustering of the implanted dopant at the distribution peak, and interactions with extended defects, which form as a result of the implant, e.g. the {311} defects. However, as evidenced in figure 32, enhanced diffusion of the dopant persists in the pre-amorphized samples. TED of boron in crystalline Si has been attributed to the {311} defects, but the same cannot be said for this experiment, as no {311} defect formation occurs due to the amorphized state of the lattice prior to B^+-implantation. The encapsulation of boron into the continuous amorphous prevents any extended defect formation during recrystallization in the amorphous layer. According to

the excess defect model, the only source of excess defects remaining within the lattice following SPEG is a fraction of the excess interstitials that lie beyond the original a-c interface.

The result from B^+-implanted into crystalline Si justifies the use of pre-amorphization, if for no other reason, to eliminate the effects of channeling. In addition, B^+-implanted into pre-amorphized Si prevented interstitial agglomeration into the {311} defects due to the elimination of the plus-one state during SPEG. This, in turn, prevents TED from free interstitials (i.e., with no vacancy complement) generated by dissociating {311} defects. Pre-amorphization does, however, appear to leave a source of interstitials at the original a-c interface[93,94] as witnessed in the RBS/channeling spectra of figure 33. The enhanced diffusion of boron following boron implantation into pre-amorphized fz-Si is thought to be driven by those interstitial-type defects found on the crystalline side of the original a-c interface labeled EOR defects. The effects of the distinct band of damage left by pre-amorphization upon dopant diffusion were investigated using different implant temperatures and fluences to alter the damage morphology and ultimately the magnitude of EOR damage at the a-c interface. The energy of all dual amorphizing implants was kept constant at 70 and 140 keV. The EOR defects are in general interstitial-type[93], but their number and microstructure depend upon the irradiation conditions as will be discussed. This investigation attempted to reveal the effect of the magnitude and microstructure of the defects residual at the a-c interface, determined from the irradiation conditions.

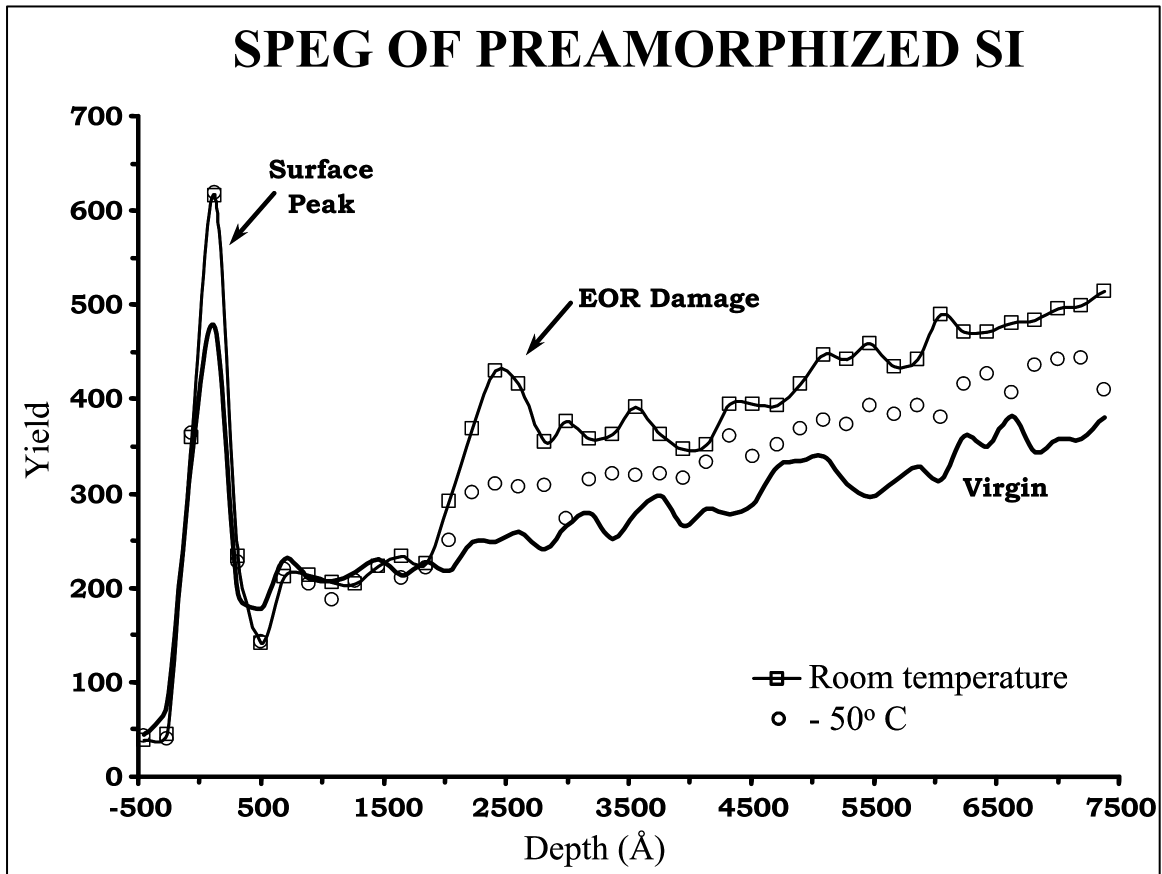

Figure 33. <100> aligned, channeled spectra of 40 keV, 10^{14} B^{+}/cm^{2} implanted into Si preamorphized with self ions at different implant temperatures; RT and - 50° C to manipulate the magnitude and configuration of damage at the a-c interface. The samples were regrown in a conventional furnace at 800° C.

Implant temperature: - 50° C versus RT

The pre-amorphizing implants, discussed in the preceding paragraph, were done at different temperatures: RT and -50° C. Ion-induced damage varies nonlinearly with temperature and exhibits a marked sensitivity near RT[8,90] so altering the implant temperature between -50° C and RT was expected to greatly impact the EOR damage. Even though damage nominally decreases with increasing temperature, the EOR defects are generally considered to increase with temperature. This is attributed, in part, to the details of the amorphization process. Since the depth of the a-c interface generally increases as temperature decreases[8,90], more of the EOR defects are eliminated by incorporation within the amorphous layer at lower temperatures. Figure 33 shows <100> aligned channeled spectra comparing the effects of a post-implant anneal at 800° C on Si pre-amorphized at RT and -50° C. First, the low channeling yield in each spectrum indicates that SPEG has eliminated the amorphous layer by single-crystal growth [fig. 33]. Secondly, the RT sample contains a distinct band of damage located at the EOR (at about 2600 Å) while the damage in the - 50° C sample is much reduced. This indicates that either less damage was formed at - 50° C or more was annealed (i.e., interstitials released) at 800° C. This reduction in damage in the colder implanted sample was anticipated considering the previous discussion of the amorphization process at - 50° C versus RT and is verified by this analysis.

The RT and -50° C samples were annealed at 800° and 1000° C for 15 minutes following B^+ implantation in a conventional furnace with argon ambient. Recalling from the earlier discussion of the diffusion of boron in crystalline silicon, there should be little or no movement of boron for thermal processing at 800° C for 15 minutes. However, the

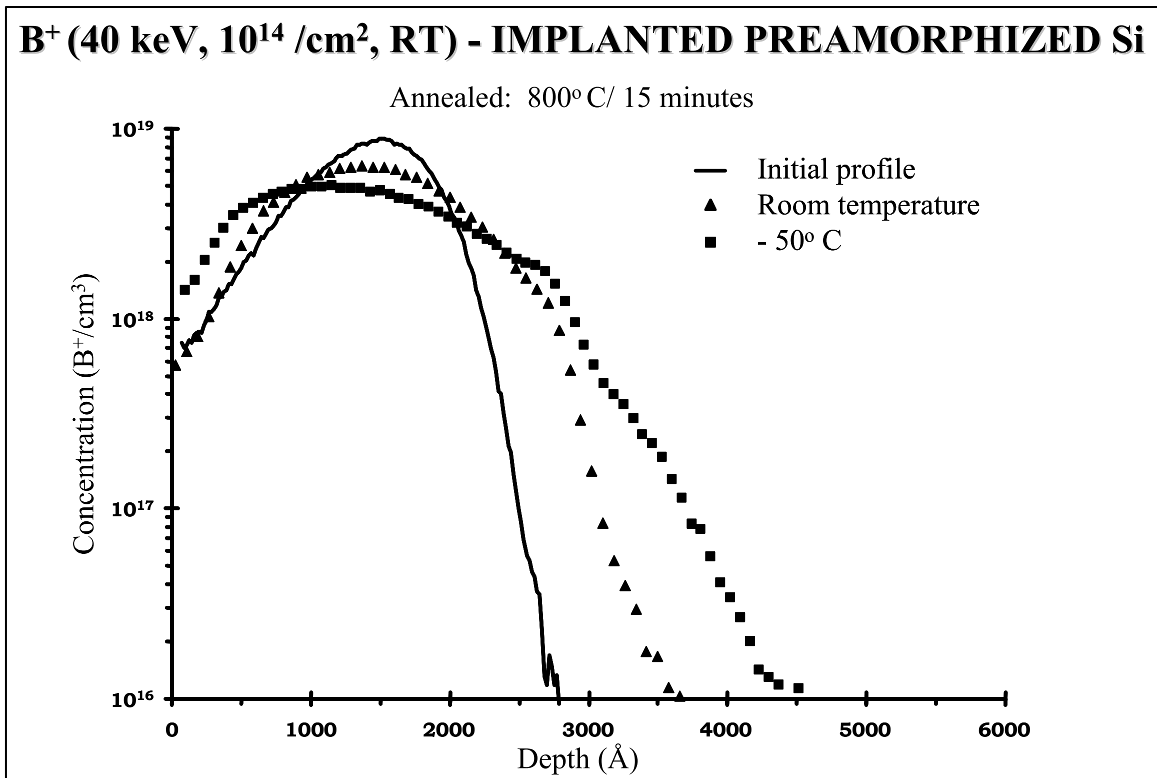

Figure 34. SIMS profiles of 40 keV, 10^{14} B^{+}/cm^{2} implanted into Si pre-amorphized with self ions at different implant temperatures; RT and - 50° C. These samples were annealed at 800° C for 15 minutes and the initial profile was added for reference. Reprinted from *J. Electron. Mater.* **26**(11), E. G. Roth, O. W. Holland, V. C. Venezia, and Bent Nielsen, "Methods of Defect-Engineering Shallow Junctions Formed by B^{+}-Implantation in Si", p. 1349, Copyright 1997, with permission from TMS.

diffusion at 800° C of the RT and -50° C profiles is significantly enhanced [fig. 34]. The diffusivity of the - 50° C sample was measured to be 3×10^{-14} cm^2/s, which is three orders of magnitude greater than the tracer value, although it is smaller by half than the diffusivity measured in Si implanted with B^+ only. Also, a comparison of the initial profile with both diffused profiles indicates a very smooth transition (i.e., no sign of any immobile boron remains at the range of the implanted B) which is consistent with previous results.[109] The absence of an immobile peak was anticipated since the SPEG incorporates the implanted boron onto lattice sites leaving no interstitial boron to form complexes. This clearly indicates another advantage of using pre-amorphization in maintaining a shallow profile following implantation of a light ion, for example in the formation of junctions by B^+-implantation.

More diffusion had been anticipated in the RT sample due to the higher concentration of EOR damage in that sample. However, the diffused profiles in figure 34 show that the boron in the - 50° C sample extends about 1000 Å farther into the substrate than the RT sample. While it is clear that pre-amorphization did not eliminate TED, it is significant to realize that the junction depth can be affected by as much as 1000 Å just by changing the implant conditions. These results contribute to a burgeoning picture of the sensitivity of TED to the presence of excess interstitial-type defects from pre-amorphization. K. S. Jones, et al.[109] observed TED of epitaxially grown boron marker layers in regrown Si. The sample was amorphized with 146 keV, 5×10^{15}/cm^2 Si^+ implanted at 77 K (- 196° C) or the same implant with 292 keV Si^+-ions. However, H. S. Chao, et al.[107] witnessed no movement of implanted boron within regrown Si when they amorphized the Si substrate with 100 keV, 2×10^{15}/cm^2 Si^+ at RT. These differing results

were explored by considering the density and size of the dislocations within the EOR band at the a-c interface (which is directly dependent upon the amorphizing implant conditions). Defect clusters at the implanted range of the ion coalesce to form larger more stable defects (i.e., dislocations, during the annealing process).[25,117] This coarsening of the EOR defects into stable dislocations not only ties up interstitials, making them unavailable for participation in TED (over the temperature range where the defects remain stable), but can also getter any interstitials released from smaller, less stable clusters during thermal cycling. In Jones' experiment, the amorphizing implant conditions produced a low density of dislocations at the a-c interface, which allowed interstitials to back diffuse into the regrown layer and contribute to boron diffusion. The amorphizing implant at RT performed by Chao et al., however, produced EOR dislocations of sufficient size and density to act as a significant sink for interstitials so none were released to contribute to TED. The results presented for this experiment are consistent with the results of these two other experiments. The RT implant in this experiment, consistent with Chao's results, limited the transiency (compared to that of the - 50° C sample, see fig. 34) but failed to produce the "critical" size and density of dislocations necessary to completely block the interstitials at the original a-c interface. Comparison of the pre-amorphizing conditions between the various experiments is consistent with this conclusion. The self-ion dose used in the present experiment was lower than in Chao's work and should produce fewer defects within the EOR band; in fact, as simulated by TRIM[24] the number was reduced by a factor of two.

Although consider the work of Solmi, et al.[118] and Pennycook and coworkers.[119,120] They questioned the "purity" of the regrown layer suggesting the

regrown layer retained memory of lattice strain from the defect pathology[118] or rather incorporated trapped supersaturations of interstitials following processing.[119,120] The diffusion observed in the regrown samples varied according to the amorphization conditions, RT versus - 50° C. Per the above discussion, it would appear that the diffusion, respective of the different amorphizing conditions, may be accounted for by considering the magnitude and microstructure of those defects found below the a-c interface, i.e. the EOR defects. So, even if some memory of the excess defects remained within the SPEG layer, it did not appear to exceed the contribution from the interstitial defects at the EOR. The difference between the two measurements represents the minimum effect of the EOR defects, but this is comparable to the total effect. Thus, the contribution from the EOR defects is evident in the resulting diffusion of boron in regrown Si following thermal processing.

As suggested by the excess defect model, residual defects remain below the continuous amorphous layer. Since altering the pre-amorphizing implants affects the defect microstructures below the a-c interface, the successful elimination of TED of B^+ in amorphized Si rests upon the density and configuration of those EOR defects below the a-c interface following SPEG. This defect band, if of sufficient density, acts as an effective barrier, essentially a perfect sink, to those defects present below the a-c interface that dissociate and back diffuse towards the surface.

Further speculation of the profiles diffused at 800° C revealed an abrupt change in the slope of the boron profiles at 2600 Å; the position of the a-c interface. At this depth, an anomalous bump occurs, as seen in figure 34. The depth correlation between the EOR damage in the RBS/channeled spectra [fig. 33] and the anomalous bump in the 800° C

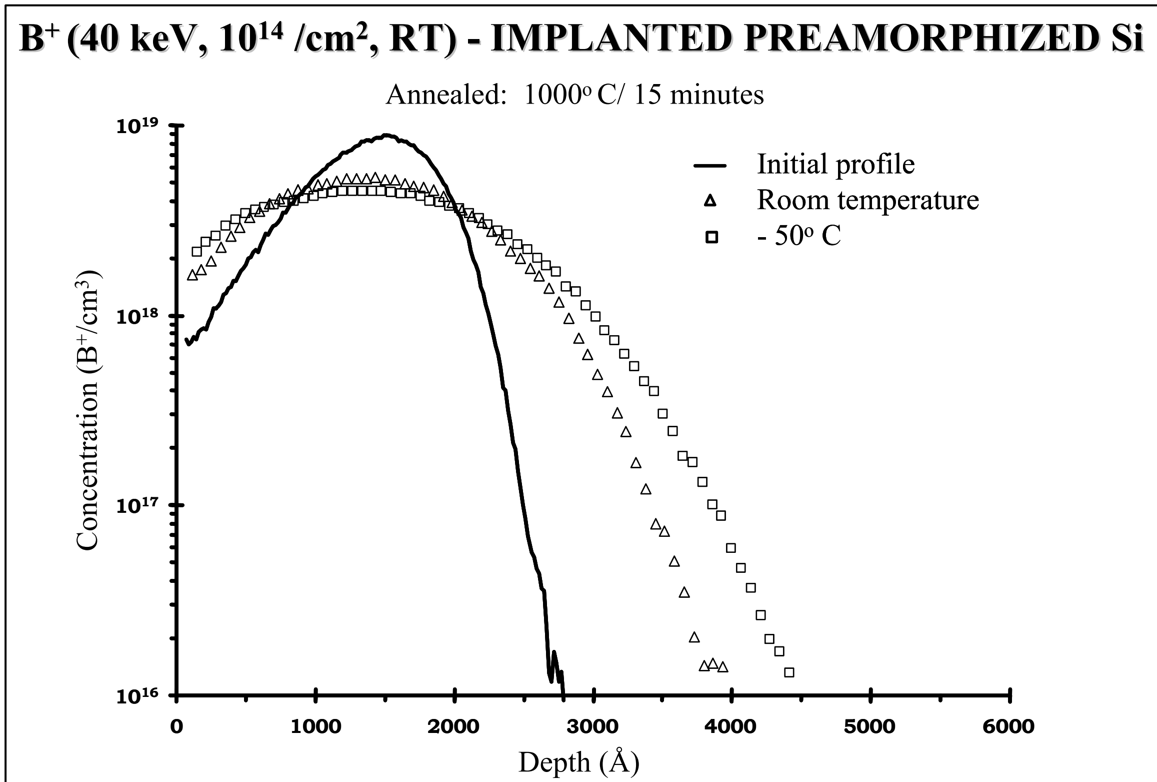

Figure 35. SIMS profiles of 40 keV, 10^{14} B^+/cm^2 implanted into Si pre-amorphized with self ions at different implant temperatures; RT and - 50° C. These samples were annealed at 1000° C for 15 minutes and the initial profile was added for reference. Reprinted from *J. Electron. Mater.* **26**(11), E. G. Roth, O. W. Holland, V. C. Venezia, and Bent Nielsen, "Methods of Defect-Engineering Shallow Junctions Formed by B^+-Implantation in Si", p. 1349, Copyright 1997, with permission from TMS.

diffused profiles implies that the diffusing boron is interacting with the damage at the EOR.[121] As suggested in ref. 128, impurities can pin extended defects, preventing further motion, and also create nucleation sites for damage growth. This bump at the depth of the a-c interface is absent in both the RT and - 50° C profiles diffused at 1000° C for 15 minutes reported in figure 35. Thus, any interaction between the EOR defects and the diffusing dopant is minimal at this time and temperature of thermal processing. Also, the diffusion in the boron profiles at 1000° C follows the tracer value for diffusion much more closely; indicating TED does not dominate thermal processing at 1000° C. Surprisingly, the diffusion at 1000° C is not that dissimilar to that at 800° C, indicating higher-temperature, shorter-cycle anneals might effectively manage the effects of transient diffusion.

Dual implantation in SOI

A second technique was investigated foregoing the development and regeneration of an amorphous layer, and investigating another mechanism for eliminating ion-induced interstitial defects. This alternative method involved the injection of defects by high-energy ion implantation as opposed to pre-amorphization of the substrate prior to dopant implantation. High-energy ion implantation was used to inject vacancies to produce recombination centers for plus-one interstitials from the subsequently implanted dopant. Co-implantation is a process where implants are performed sequentially. In this experiment, ions were co-implanted to create overlapping regions of complementary point defects to enhance the probability of recombination, described in figure 36. In this dual implant study, a MeV implant was performed prior to an implant of $10^{14}/cm^2$ B^+-ions similar to the previous experiment. High-energy Si^+-self-ions implanted into an SOI

Co-Implantation of High- and Medium-Energy Si^{+}-ions

High-energy implant: Si^{+} (2 MeV, 1 and 5 × 10^{15} /cm^2, RT)

Boron implant: B^{+} (40 keV, 10^{14} /cm^2, RT)

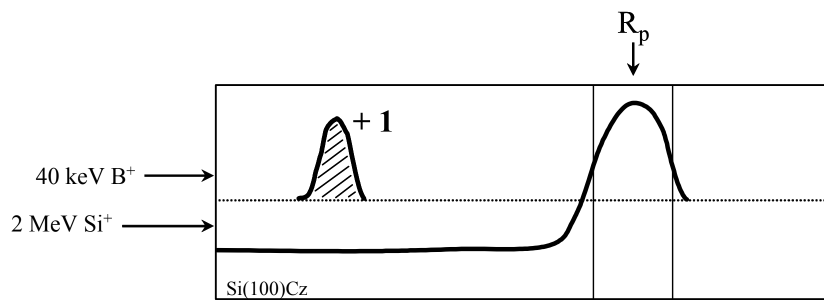

Figure 36. B^{+}-ions implanted into SOI implanted first with 2 MeV Si^{+}-ions at RT to influence B^{+}-induced interstitials to recombine with vacancy defects in the near-surface layer from the MeV implant.

substrate were intended to modify the defect distribution by positioning excess vacancies in the vicinity of the B^+-induced interstitials.

SOI material was the chosen substrate in this experiment because of its unique structure including a single-crystal surface layered above a thick buried oxide. Implantation was done at energies which placed the interstitial excesses well beyond the Si/SiO_2 interface to limit interstitial defect fluxes from R_p of the MeV implant. The co-implanted SOI samples were each implanted with B^+-ions following a dose of 2 MeV Si^+-ions at either 1 or $5 \times 10^{15}/cm^2$, which yielded an excess or net vacancy concentration of 10^{18} and $5 \times 10^{18}/cm^3$, respectively, as predicted by TRIM.[24] The vacancy concentration produced at the higher dose compares with the peak concentration of boron of $1 \times 10^{19}/cm^3$. Figures 37 and 38 show the 800° C diffused profiles of the 1 and $5 \times 10^{15}/cm^2$ MeV co-implants, respectively. No effect was observed for the sample implanted with both $1 \times 10^{15}/cm^2$ MeV and B^+-ions. The co-implanted profile diffused about 1000 Å beyond the initial profile, the same as in the sample implanted with B^+ only. However, while some movement of the B profile is seen in the co-implanted sample at the higher dose, 5×10^{15} Si^+/cm^2, the junction depth remained unchanged from its position in the as-implanted profile. An anomalous out-diffusion of boron with the higher dose MeV implant of Si^+-ions is observed following annealing at 800° C. Some B within the shallow portion of the profile moved towards the surface. This represents an interesting phenomenon, one not fully explored within the scope of this study. It is clear that the vacancy injection at the higher dose (where the vacancy concentration more nearly matched the implanted fluence of boron) had a marked effect in controlling diffusion leaving the depth of the diffused profile the same as the original. This was

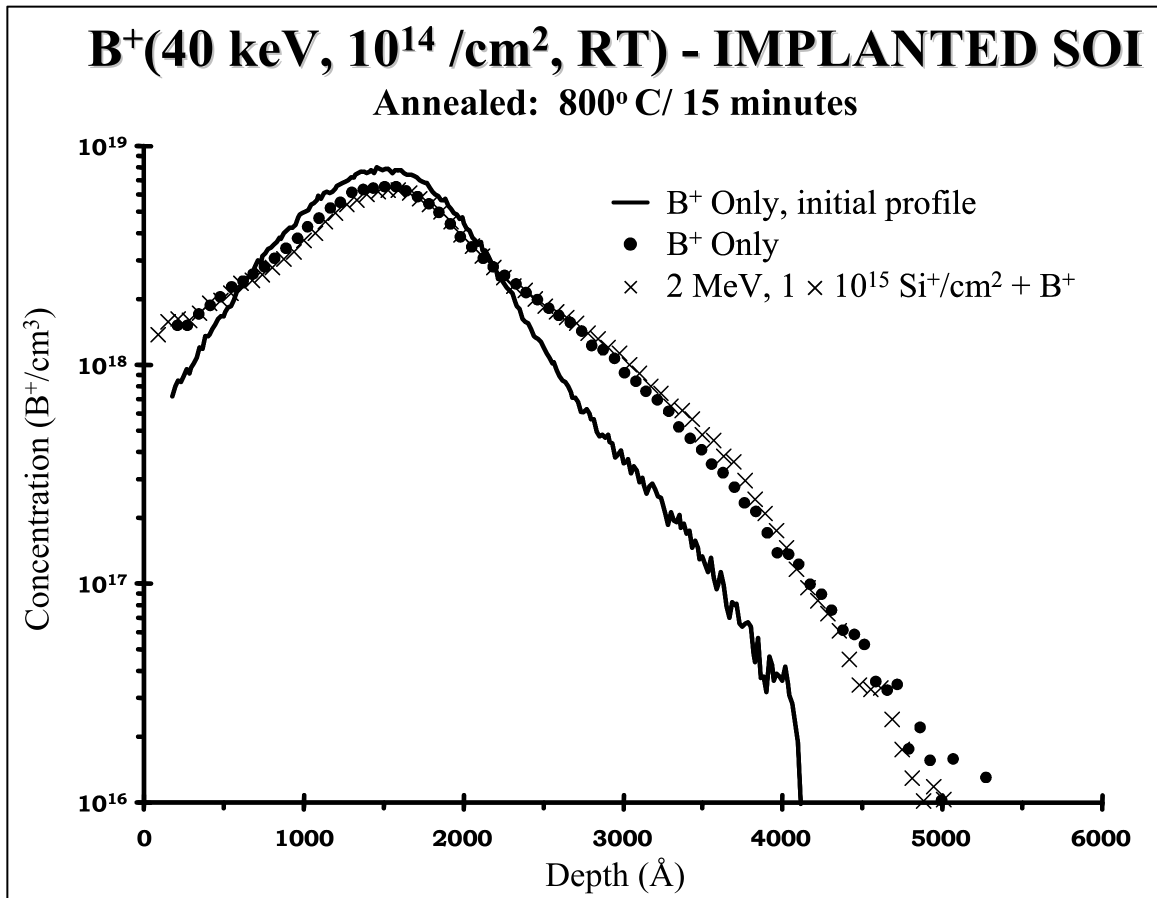

Figure 37. SIMS profiles for 40 keV, 10^{14} B^+/cm^2 implanted into SOI. The samples were diffused at 800° C for 15 minutes. The initial profile of B^+ only implanted into SOI was compared to material co-implanted with 2 MeV, 1×10^{15} Si^+/cm^2. The diffused B^+-only profile was added for reference. Reprinted from *J. Electron. Mater.* **26**(11), E. G. Roth, O. W. Holland, V. C. Venezia, and Bent Nielsen, "Methods of Defect-Engineering Shallow Junctions Formed by B^+-Implantation in Si", p. 1349, Copyright 1997, with permission from TMS.

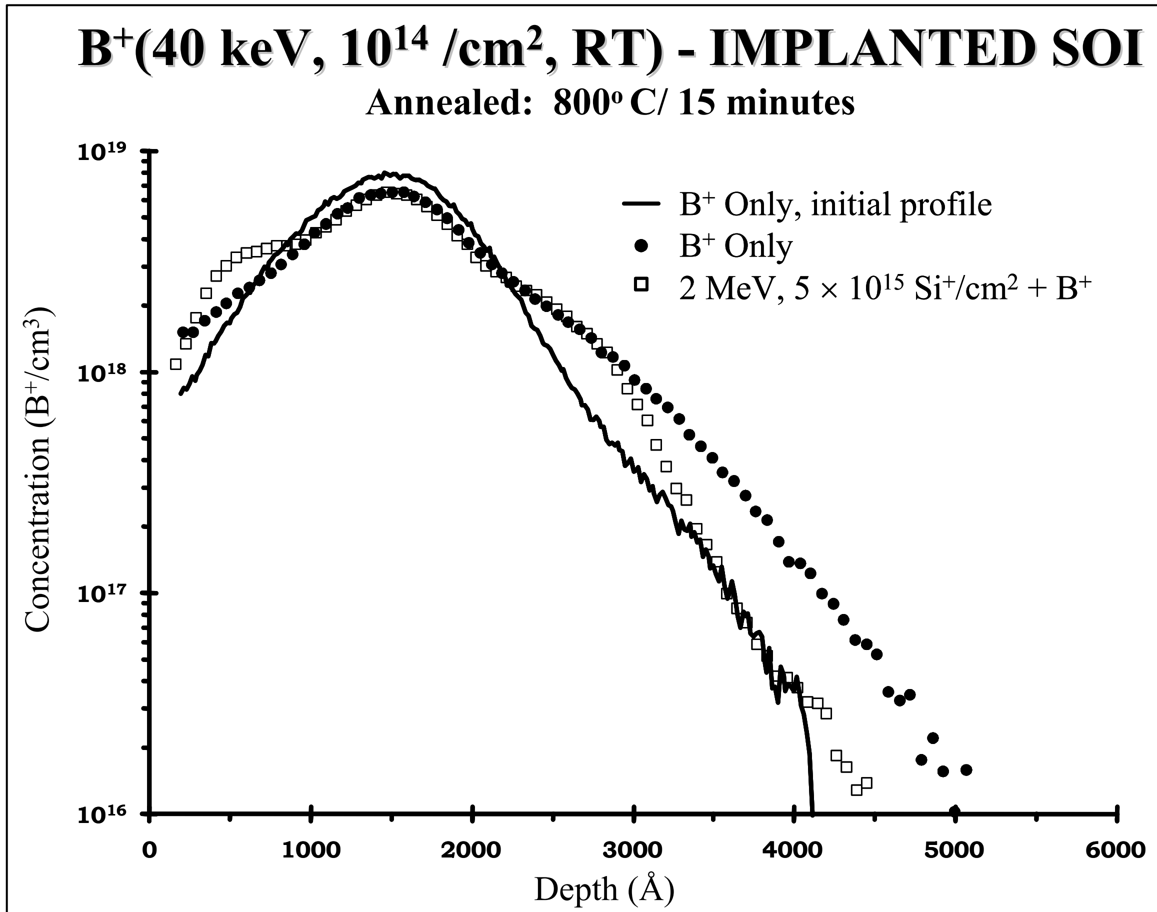

Figure 38. SIMS profiles for 40 keV, 10^{14} B^+/cm^2 implanted into SOI. The samples were diffused at 800° C for 15 minutes. The initial profile of B^+ only implanted into SOI was compared to material co-implanted with 2 MeV, 5×10^{15} Si^+/cm^2. The diffused B^+-only profile was added for reference. Reprinted from *J. Electron. Mater.* **26**(11), E. G. Roth, O. W. Holland, V. C. Venezia, and Bent Nielsen, “Methods of Defect-Engineering Shallow Junctions Formed by B^+-Implantation in Si”, p. 1349, Copyright 1997, with permission from TMS.

presumably due to recombination with the plus-one interstitials. The absence of an effect at the lower dose of MeV-ions leaves some doubt within the details of the mechanism. However, the results might suggest a sufficient vacancy concentration is required to annihilate the defects introduced with the boron implant.

It is interesting to note that a deep channeling tail, extending to about 4000 Å, is common to both as-implanted B^+ profiles in bulk Si(100) [fig. 32] and SOI [fig. 37]. However, similarities between the profiles end there. The 800° C diffused profile in bulk Si is about 500 Å deeper than the respective profile in SOI. The greater amount of TED in bulk Si than SOI is an important aspect of ion-induced effects, especially in porting Si-based manufacturing technology to meet the emerging applications for SOI-based electronics. This smaller amount of TED in SOI clearly indicates the number of "free" interstitials within the diffusion volume is less than in implanted fz-Si. The reason for this is unknown but is probably related to two obvious differences in the materials. The presence of the Si/SiO_2 interface in the SOI substrate may getter interstitials from the diffusion volume. Additionally, the SOI is fabricated using Czochralski-grown Si, which has a higher concentration of impurities such as oxygen and carbon than fz-Si. These impurities are known to bind to defects. Such complexes, if stable at the diffusion temperature, can reduce the number of interstitials available for diffusion and, thus, reduce TED.

To summarize, the amorphization of silicon with $^{30}Si^+$-self ions prior to implantation of boron eliminated both ion-channeling effects and clustering of the implanted boron, which immobilizes boron near the peak of the implanted profile. However, amorphization of the Si layer did not eliminate TED of boron, apparently as a

result of the defect band at the a-c interface, which was not of sufficient density to capture interstitials dissociating from the EOR defects during a post-implant thermal treatment. This defect flux across the a-c interface drives TED of boron in pre-amorphized Si. Although the transient was reduced by a factor of two over that in the B^+-only implanted sample. In fact, manipulating the irradiation conditions, and in turn, the microstructure and configuration of the EOR defects, alters the junction depth by 1000 Å. Further investigation might yield control over TED by way of pre-amorphization of the material prior to dopant implantation through discerning manipulation of the irradiation conditions.

The co-implantation technique involving high-energy and subsequent dopant implants was more successful in engineering the excess defects, and consequently, mediating TED of boron. Co-implanting a sufficient dose of high-energy Si^+-self ions with B^+-ions controlled the TED of boron so that the junction depth was not altered following a post-implant thermal anneal. Unexpected anomalies in the annealed profile inhibit direct recognition of the mechanism involved in this co-implantation series. The clustering peak at the height of the boron profile; anomalous out diffusion and initial inward diffusion; and the effectual cut-off of additional movement of the dopant profile establishing the annealed junction depth at the exact position of the as-implanted profile were evident.

Experiment II: "Front" amorphization – eliminating the end-of-range defects associated with amorphization

Discussion

Development via utilization of excess defect model

Regrowth of an amorphous layer through SPEG yields a defect-free crystalline layer in registry with the underlying substrate.[92] Upon recrystallization, any implant damage within the continuous amorphous layer is “erased” or removed and a perfect single crystal above the original a-c interface is restored. Since the ion-induced defects responsible for the redistribution of the TED of dopants are encompassed fully within the amorphous layer, amorphization of the layer and subsequent SPEG should presumably eliminate the formation of any residual defects including extended defects, such as {311}’s.[122] Logically, it was anticipated that TED of boron might be eliminated when the boron distribution and all B^+-induced defects were completely encompassed within a pre-existing amorphous layer. However, following a thermal anneal, TED of B markers within Si pre-amorphized with either Si^+[109] or Ge^+[123] has been reported. In fact, several researchers hold the interstitial-type defects below the a-c interface contribute to the TED of boron within the regrown layer.[109,124] This is consistent with results previously discussed. Thus, pre-amorphization of the lattice prior to dopant implantation is not sufficient to eliminate the defects responsible for TED.

SOI versus bulk Si

In an attempt to unequivocally determine the mechanism behind TED of boron within SPEG layers, a novel “front amorphization” experiment was designed. This front amorphization experiment, illustrated in figure 39, included recrystallization of a buried amorphous layer from the surface down to the top SiO_2 interface found within SOI material. Islands or isolated zones of defect-free crystalline Si were left at the surface

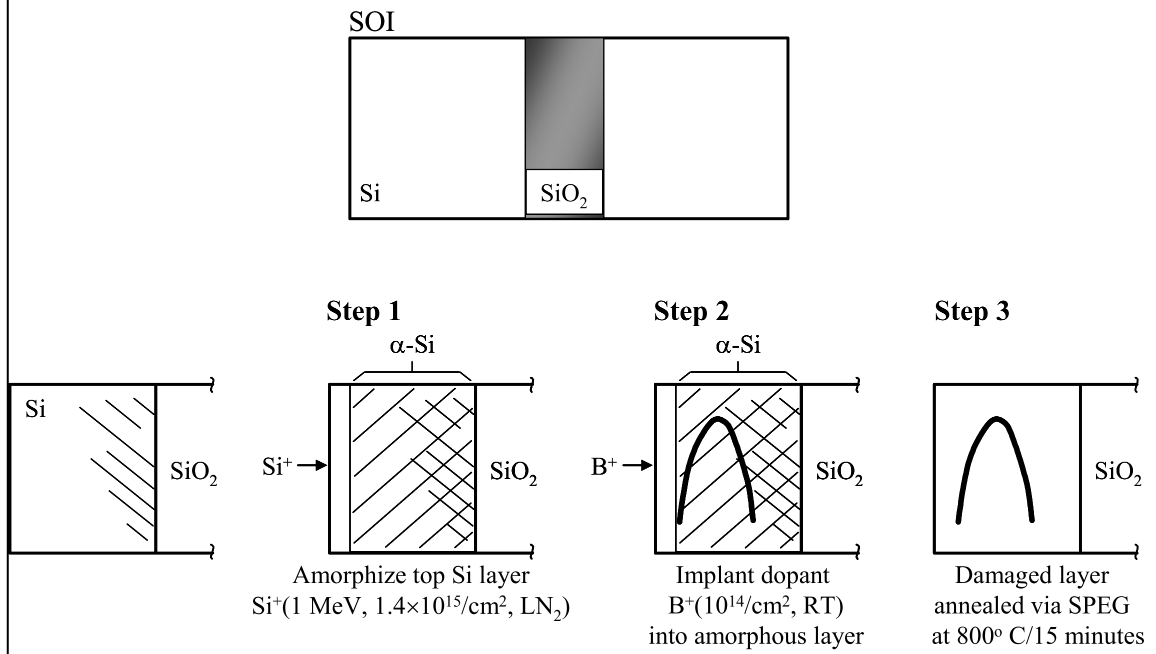

Figure 39. "Front Amorphization" experiment: pre-amorphize crystalline Si layer of SOI material to just below the surface, so solid phase epitaxial growth of the amorphous layer will be seeded from the surface where a known vacancy supersaturation exists from the MeV implant necessary to amorphize the Si to just below the surface.

following amorphization to seed SPEG. This technique is similar to one used to decrease the defect density in silicon-on-sapphire (SOS) material[125] and in the formation of SOI material by O^+ implantation.[126] This method is substantially different from traditional pre-amorphization of Si where a continuous amorphous layer is formed at the surface with a buried a-c interface. It will be shown that the nature of the residual defects at the a-c interface when recrystallized from the surface is different from that buried interface in traditional pre-amorphized layers. This experiment will explore these differences which will clarify the nature of the defects on the crystalline side of the a-c interface and their role in TED of implanted boron.

Preliminary studies were done to determine the interaction between the vacancies and interstitials that survive implantation in SOI material versus bulk Si. Si^+-self ions were implanted in both SOI and bulk fz-Si with an energy of 2 MeV to a fluence of $1 \times 10^{17}/cm^2$ at 450° C. Implantation at the elevated temperature was necessary to promote local recombination between the vacancies and interstitials to reduce the damage in the lattice from the implant process. PAS profiled the distribution of vacancy-type defects in the respective samples. The dependence of the vacancy defects upon annealing temperature was evaluated at temperatures of 800 and 1000° C. The S-parameter is plotted versus positron energy following annealing for both implanted SOI and Si samples in figures 13 and 40, respectively. Following annealing at 800° C, the normalized S-parameter is higher in the Si than in SOI. The difference in the intrinsic oxygen concentration in Czochralski (Cz)-Si versus fz-Si might explain the observed phenomenon. The top Si layer of the SOI material is essentially Cz-Si. The higher O concentration in Cz-Si is due to the growth processes of fz- and Cz-Si. The growth

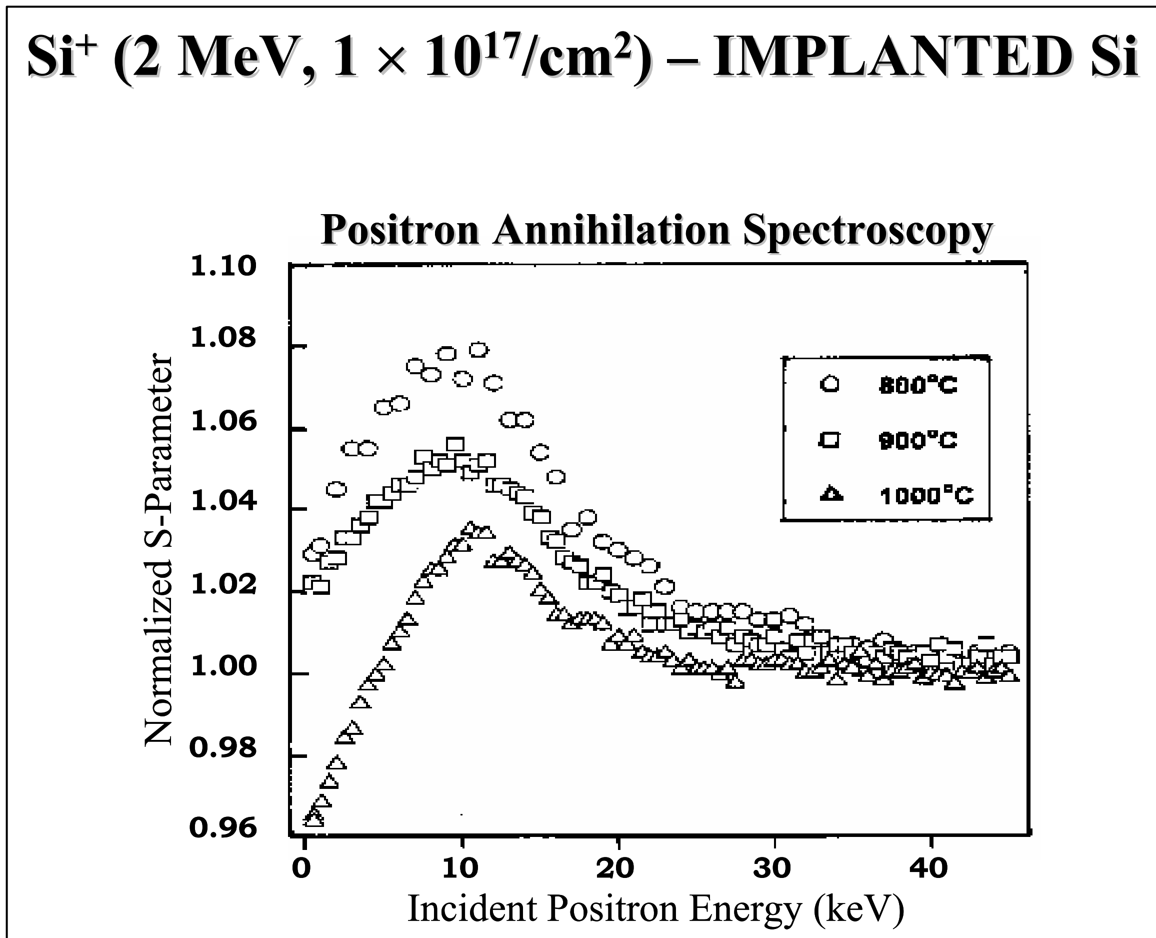

Figure 40. PAS of 2 MeV, $10^{17}/cm^2$ Si^+ implanted into Si and annealed at 800, 900, and 1000° C. The vacancy defects survive to high annealing temperatures.

process for fz-Si results in a purer crystalline Si containing a lower concentration of impurities. Two facts exist, first, the intrinsic oxygen concentration in Cz-Si exceeds that found in fz-Si and second, oxygen interacts inherently with vacancy defects forming V_nO complexes (where n is the number of vacancies in the complex), and will result in a lower S-parameter.[35] Comparing the S-parameter of the 1000° C annealed SOI and Si samples, figure 13 and figure 40, respectively; it is obvious that the vacancy defects survive to higher annealing temperatures in SOI than in bulk Si. This result justifies the assumption that the SiO_2 layer traps the excess interstitials injected by MeV irradiation and reduces the communication between the vacancies and interstitials from the MeV implant. This is important for the front amorphization experiment because with the presence of a SiO_2 layer, recrystallization is induced from the surface into the bulk, and also deep interstitials are prevented from back diffusing towards the surface and into the regrown layer.

Experiment

Bonded SOI material was used in this experiment, which formed by bonding to two silicon wafers with oxidized surfaces. Following bonding, the surface is polished sufficiently to yield a 1-μm-thick Si overlayer, and a buried oxide. The SOI samples were prepared with a continuous amorphous layer extending from just below the surface of the Si to the buried Si:SiO_2 interface by implanting 1 MeV Si^+-ions at LN_2 temperature to a fluence of $1.4 \times 10^{15}/cm^2$. The implant was performed at LN_2 temperature to manipulate the near-surface morphology in the samples. The amorphous layer advances in a planar fashion for RT implantation, but for LN_2 temperatures the amorphous layer grows via the overlapping of amorphous clusters.[8,90,127] Thus, amorphization at cold

temperatures allows the a-c interface to approach the surface, leaving only pockets of crystalline Si at the surface to seed SPEG of the buried amorphous layer. To the sensitivity of RBS, the layer may in fact appear amorphous (i.e., the backscattered yield is equal to that of the random profile). However, investigating the behavior following a low temperature anneal for a short time reveals regrowth only at the surface, which is consistent with crystallization of a mixed phase, e.g., amorphous pockets coexistent with crystalline Si.[89]

The fluence was sufficient to amorphize the 1-μm-thick Si overlayer leaving small amounts of residual crystallinity at the surface to seed SPEG of the buried amorphous layer. Following amorphization, 40 keV, $10^{14}/cm^2$ B^+-ions were implanted at RT. At this energy, the B distribution was completely encompassed within the amorphous layer. These steps are illustrated pictorially in figure 41. SIMS using an O^+ primary beam profiled the B. RBS/channeling analysis with 2.3 MeV He^{++}-ions characterized the amorphized layer and residual defects following SPEG. The post-implant anneals were completed in a quartz-tube furnace with a flowing Ar ambient.

Results

RBS/channeling analysis of the implanted sample, figure 42, reveals the progression of SPEG and the quality of the recrystallized layer following annealing. Analysis of a 300° C-annealed profile confirmed that crystalline Si islands remnant at the surface seeded recrystallization of the buried amorphous layer. The reduction of the aligned yield after 300^oC annealing [fig. 42] is consistent with epitaxial recrystallization of small amorphous inclusions, which are known to anneal at lower temperatures than a continuous amorphous layer.[89] No recrystallization is observed at this temperature other

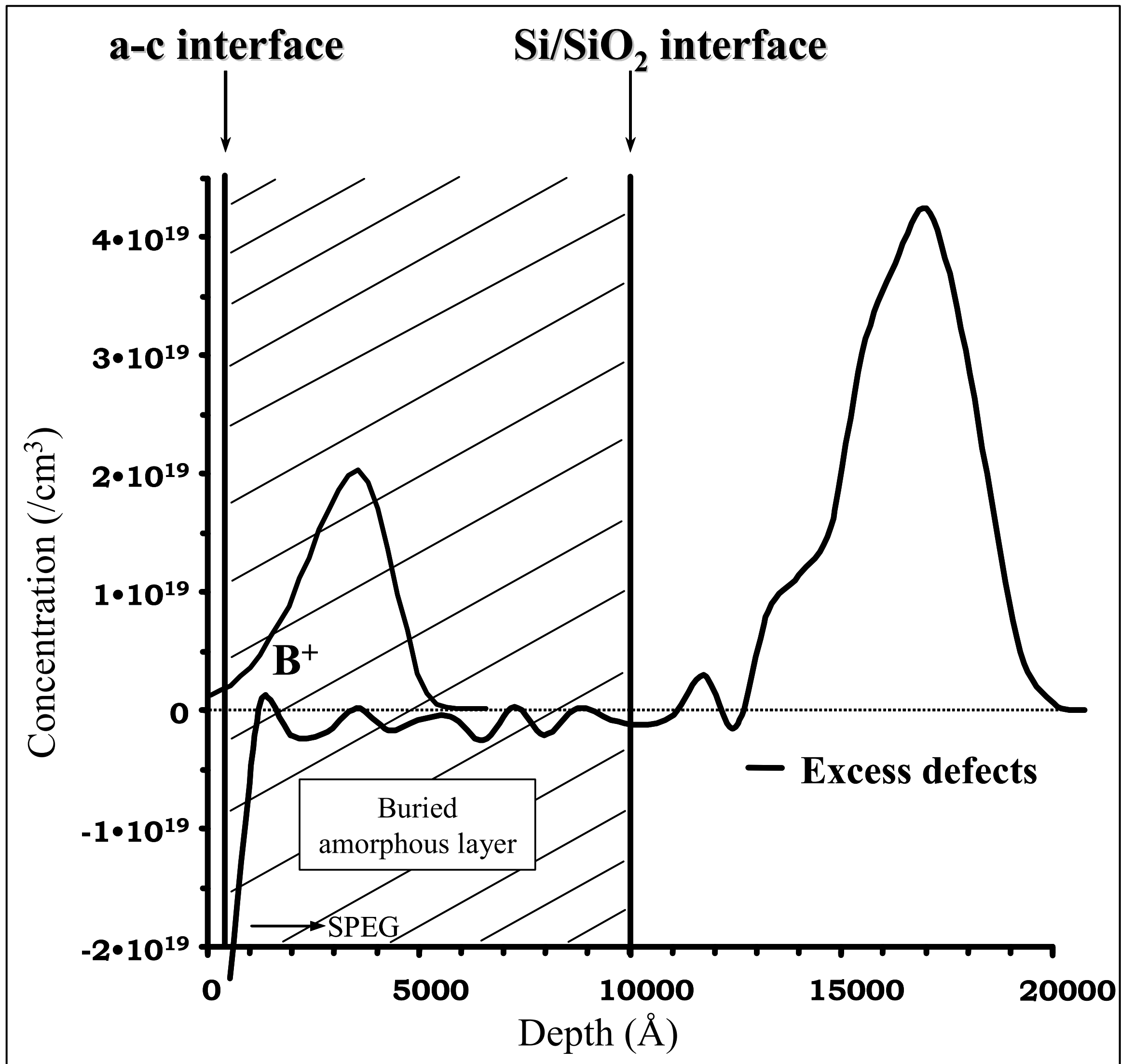

Figure 41. Progression of implants supporting the front amorphizaton experiment are displayed in a pedagogical illustration showing the first amorphizing Si implant, Si^+(1.25 MeV, $1.4\times10^{15}/cm^2$, LN_2) SOI, deposited the interstitial excess from the amorphizing implant beyond the Si/SiO_2 interface and amorphized the top Si layer continuously to just below the surface leaving enough crystalline material to initiate SPEG of the layer with the anneal following introduction of the boron, dopant implant contained entirely within the amorphous layer.

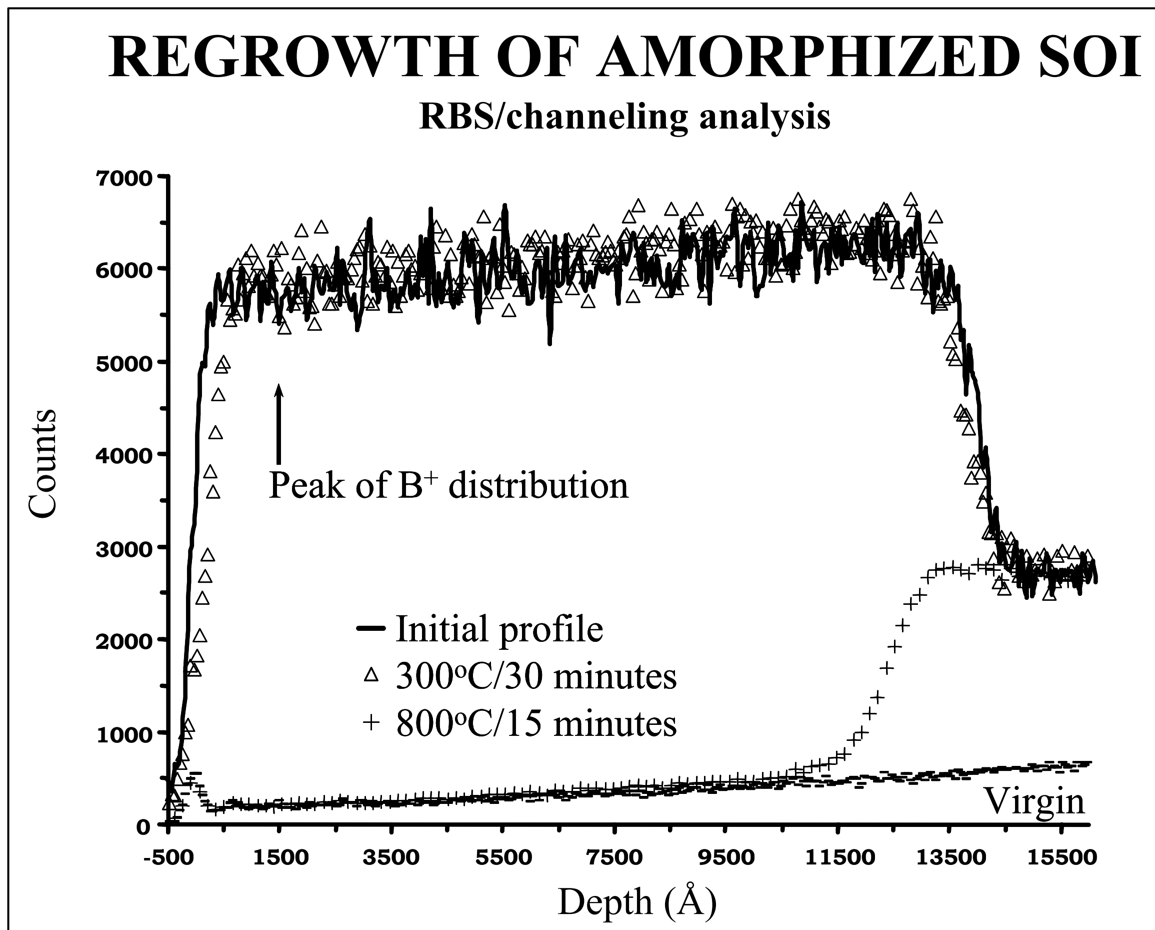

Figure 42. Aligned RBS/channeling analysis of SOI amorphized with Si^+ (1.25 MeV, $1.4\times10^{15}/cm^2$) at LN_2 temperature. An anneal of 300° C for 30 minutes compared with the initial profile confirms SPEG seeded from the crystalline Si left at the surface. The aligned yield of the 800° C, 15 min. annealed profile compared with the virgin spectrum indicates a high quality regrowth. Reprinted with permission from E. G. Roth, O. W. Holland, and D. K. Thomas, *Appl. Phys. Lett.* **74**(5), 679, Copyright 1999, American Institute of Physics.

than near the surface. The backscattered yield following regrowth at 800° C for 15 minutes, in figure 42, is consistent with that observed in the virgin or unimplanted sample. Thus, to the sensitivity of RBS/channeling, little or no damage exists either within the regrown layer or at the Si/SiO_2 interface. Also, the 800° C results further confirm that SPEG was seeded only from the front interface. If SPEG were initiated from the oxide-Si interface as well as the front, a polycrystalline layer would be observed within the Si overlayer, and no such layer is present. Amorphous layers are regrown, as groups of atoms are reoriented to the underlying crystalline structure. Growth persists into the amorphous layer. If growth occurs from both a back and front amorphous layer, as the two proceeding interfaces meet, polycrystalline structure results due to the incorporation of the network of accompanying defects.

Since TED of boron provides clear evidence for the presence of interstitial defects within the irradiated volume, analysis of diffusion profiles provides a sufficient test to determine the efficacy of any method devised to eliminate those defects. Specifically, the diffusion of the implanted dopant will be monitored as a tool to investigate the defect distribution residual in the lattice following implantation of the dopant within an amorphous layer and subsequent thermal treatment. SIMS was used to profile the boron distributions both initially and following annealing. Figure 43 shows a boron profile following 800° C annealing for 15 minutes. Initial and 800° C profiles of boron implanted into pre-amorphized bulk Si, where the continuous amorphous layer at the surface was formed by amorphizing inward to a depth of 2500 Å, were added for reference. The profile of boron implanted into the buried amorphous layer is identical to the initial profile. The boron distribution in the regrown SOI exhibited no enhanced diffusion; while

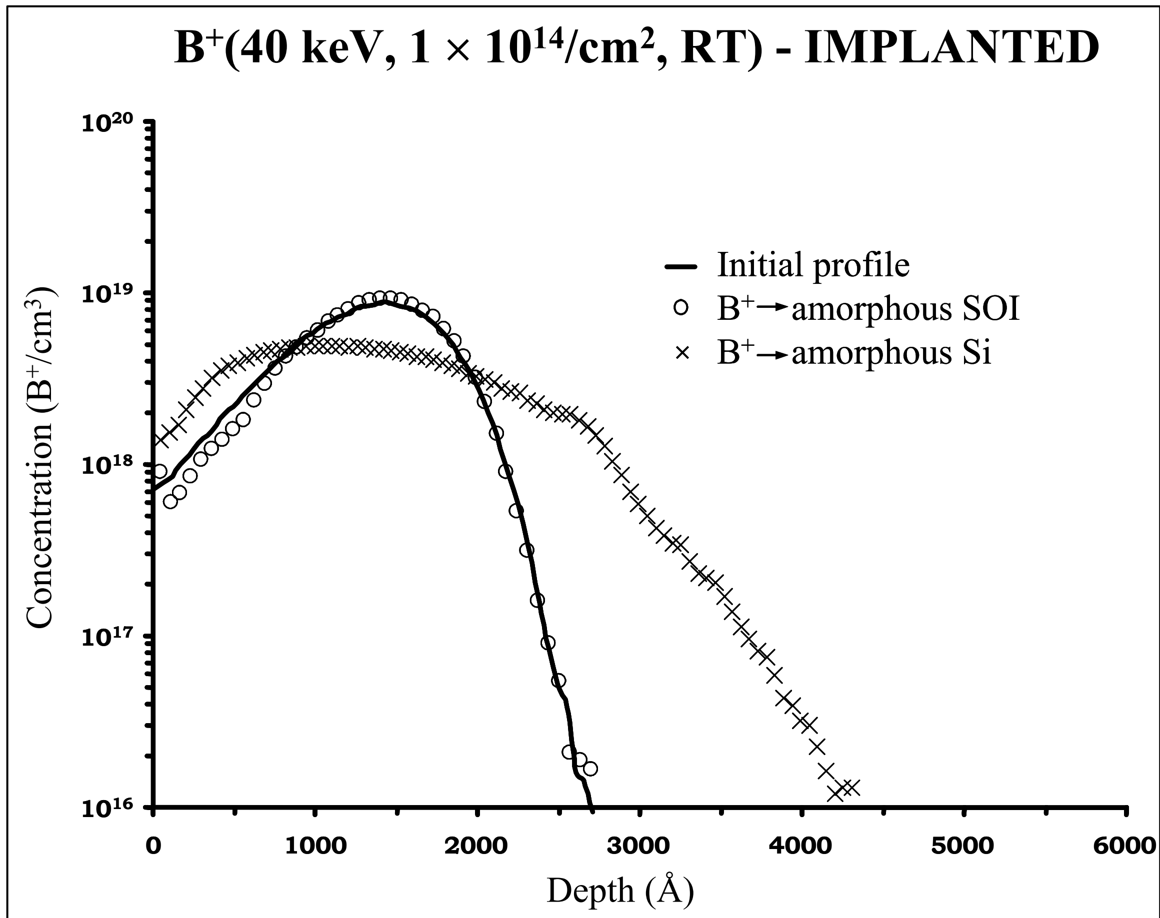

Figure 43. The diffusion of 40 keV, $10^{14}/cm^2$ B^+-ions was compared following an 800° C, 15 minute anneal for B implanted into a buried amorphous layer in SOI to B implanted into Si amorphized to the surface. The initial profile of B in Si amorphized to the surface was added for reference. Reprinted with permission from E. G. Roth, O. W. Holland, and D. K. Thomas, *Appl. Phys. Lett.* **74**(5), 679, Copyright 1999, American Institute of Physics.

for the same time and temperature of thermal processing, boron implanted into traditional pre-amorphized Si and regrown to the surface exhibited a 1000 × enhancement in its diffusivity [fig. 43]. The TED has been eliminated for boron implanted into the buried amorphous layer. This is indicative of the absence of excess defects within the regrown layer that would typically be responsible for enhancing dopant diffusion.

A second illustration of the success of this technique is for 150 keV B^+-ions implanted into a similar buried amorphous layer. The implant fluence ($10^{14}/cm^2$) and temperature (RT) were consistent with the previous measurements of 40 keV B^+-ions. In figure 44, there is clearly no movement of the boron profile following thermal processing at 800° C for 15 minutes. The 800° C annealed profile mimics the initial profile exactly. Redistribution of the boron profile was not affected by the interstitials within or beyond the SiO_2 layer from the amorphizing implant. Following annealing at 1000° C for 15 minutes, the measured diffusion is again not enhanced. The diffusion length ($\sqrt{2Dt}$) calculated for the 1000° C anneal using an intrinsic value of diffusivity of 2.6×10^{-14} cm^2/sec[128] is 683 Å. The maximum separation at any point along the profiles does not exceed this diffusion length, confirming no TED was observed for a 1000° C, 15 minute anneal. With this unique implant schedule [illustrated pedagogically in fig. 39], a buried diffusion marker may be produced by ion implantation.

The SIMS results show no movement of the boron within the buried amorphous layer following annealing at 800° C for 15 minutes, as expected from diffusion simulations for this time and temperature of thermal processing. The 1000° C annealed profile of 150 keV B^+-ions also does not exhibit any enhanced diffusion. This result demonstrates that the diffusion seen in previous experiments for boron implanted into

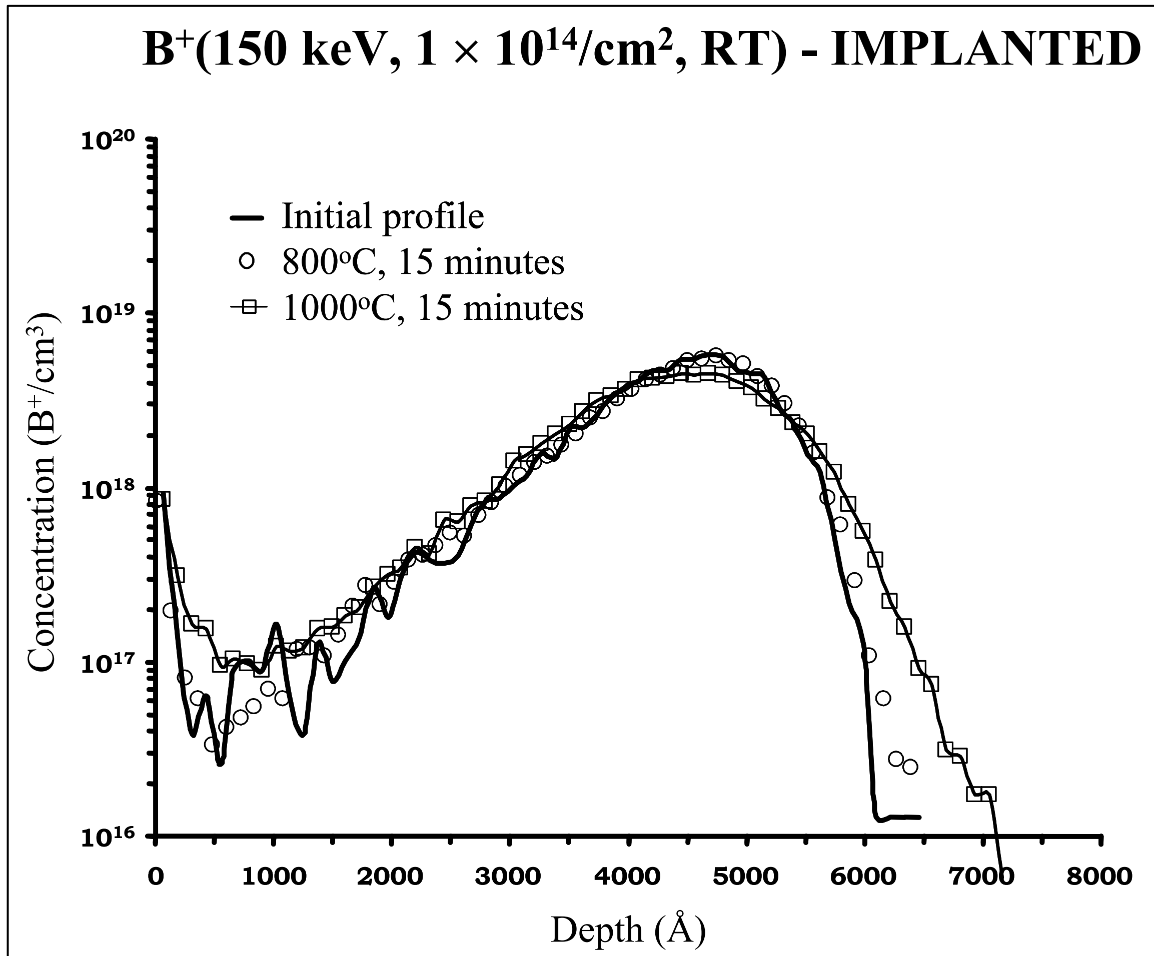

Figure 44. The diffusion of 150 keV, $10^{14}/cm^2$ B^+-ions implanted into a buried amorphous layer in SOI following annealing for 15 minutes at 800 and 1000° C was profiled with SIMS. The initial profile was added for reference. Reprinted with permission from E. G. Roth, O. W. Holland, and D. K. Thomas, *Appl. Phys. Lett.* **74**(5), 679, Copyright 1999, American Institute of Physics.

pre-amorphized Si is a direct result of the dissociation of extended interstitial defects below the a-c interface, and is not intrinsic to SPEG of the amorphous layer. The defects driving the enhanced diffusion of boron within the recrystallized layer are not trapped within the regrown layer during SPEG.

This experiment confirms the mechanism for TED of boron in pre-amorphized material and provides an example of the predictive capacity of the excess-defect model. It is clear that the TED of boron contained entirely within an amorphous layer arises if interstitial-type defects below the amorphous layer dissociate and are available to contribute to dopant diffusion during regrowth of the amorphous layer. Removing those interstitial defects eliminates any TED of the boron implanted within the amorphous layer.

Experiment III: High-energy ion implantation - dual implants with keV Si^+-self ions above the amorphization threshold

Background

Next, a dual implant technique was investigated to study the interaction of defects at the a-c interface with the vacancy defects injected during high-energy implantation. This dual implant technique is depicted in figure 45. The efficacy of these vacancies in eliminating the interstitial-type defects below the a-c interface will be examined. This distribution of excess defects produced by high-energy implantation is illustrated by a TRIM[24] simulation of a 1.25 MeV Si^+ implant in figure 30. Comparison studies of pre-amorphized materials both with and without a prior MeV implant of Si^+-ions were performed. Defect interactions were observed as a function of MeV implant parameters.

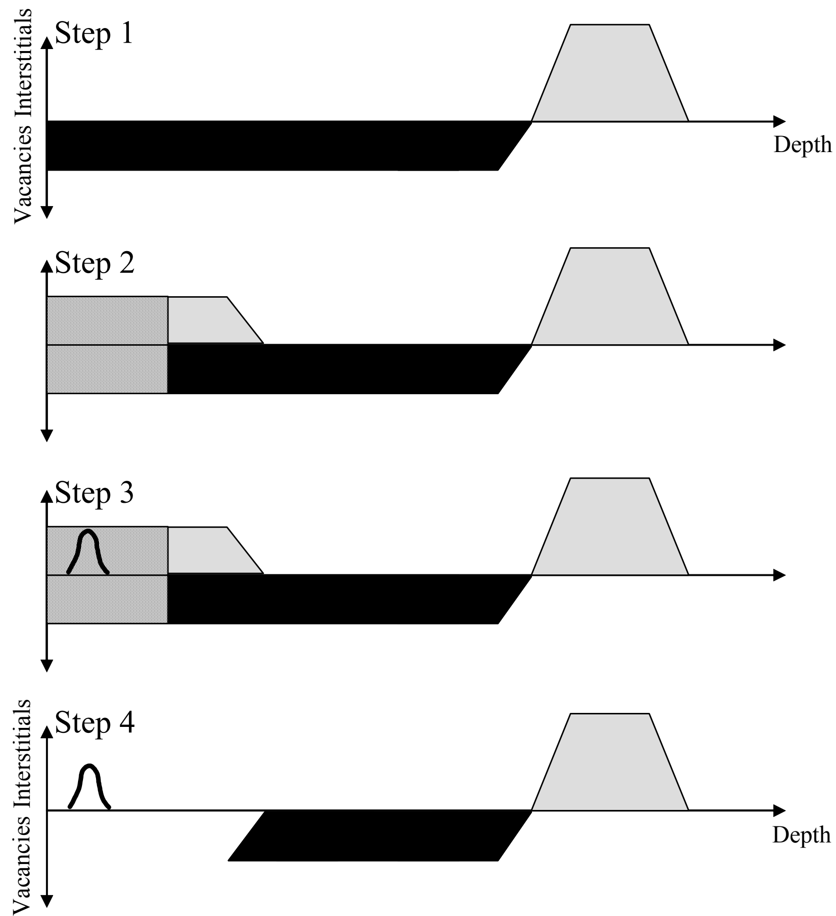

Figure 45. Measuring synergism of dual implantation and amorphization following processing steps: 1-MeV implantation of Si substrate; 2-amorphization of surface layer to a depth of approximately 2500 Å; 3-introduction of dopant species encompassed within the amorphous layer; and 4-regrowth of the amorphous layer.

Experiment

Cz-grown p-type Si(100) was used in this study. The implantation sequence involved the use of medium-energy $^{30}Si^{+}$-ions (to amorphization the lattice) followed by high-energy Si^{+}-ions. The high-energy, 1.25 MeV Si^{+}-ions were implanted at either 100, 250 or 450° C, over a range of fluence, 1 - 6 × $10^{16}/cm^{2}$. The samples were tilted five degrees, with respect to the incident beam, in an effort to minimize channeling of the implanted ions. The medium-energy implant involved the use 70 and 140 keV ions at a dose of $10^{15}/cm^{2}$ Si^{+}-ions implanted at RT, which was sufficient to amorphize the Si to a depth of ~2500 Å below the surface. RBS/Channeling analysis confirmed the amorphous layer was continuous to the surface by ensuring the backscattered yield matched a randomly aligned sample spanning the width of the layer to the surface. The random spectrum is representative of a completely randomized state within the lattice. Si-self ions were used exclusively in this study to avoid convoluting the defect interactions with chemical effects. The samples were annealed at 800° C for 20 minutes in a conventional quartz-tube furnace with an Ar-H (96 – 4%) ambient.

RBS, cross-sectional transmission electron microscopy (XTEM), SIMS, and PAS characterized the interaction of these complementary excess defect regimes within the implanted material. Three of the analysis techniques, RBS, XTEM, and PAS, were used to directly characterize the damage following SPEG of the amorphous layer. RBS/channeling measurements were performed using a 2.3 MeV He^{++}-ion beam and a standard surface-barrier detector positioned at 160 degrees to detect the backscattered ions. The samples were subsequently examined in cross section using a Phillips EM400T transmission electron microscope operated at 100 kV. Through RBS/channeling and

XTEM, the quality of the regrowth in the sample was observed and residual defect complexes were identified. PAS was used to profile open-volume defects in this near-surface region, where recombination was anticipated, as a function of annealing temperature. Finally, SIMS analysis profiled a boron distribution that was implanted completely within the amorphous layer prior to SPEG of the amorphous layer. The diffusion of boron was investigated as a probe for residual excess interstitials present below or within the regrown layer that might induce enhanced diffusion of the dopant.

Results

Removal of EOR defect band

RBS/channeling analysis was performed on dual MeV- and keV-implanted samples following SPEG of the amorphous layer at 800° C for 20 minutes. A control sample irradiated using only the medium-energy, keV ions implant was regrown following annealing at 800°C for 20 minutes, as is seen in figure 46. Figure 47 displays a typical RBS/channeled spectrum of dual-implanted material. The virgin, control, and random spectra are added for reference. The aligned yield matches that from a virgin sample, except near the original a-c interface where a defect band is clearly visible. This band is visible with RBS/channeling due to the interstitial nature of the defects. The interaction of the excess vacancies from the high-energy implant with the interstitial band following amorphization was determined by comparing the magnitude of damage residual below the a-c interface following SPEG of the amorphous layer of dual implanted samples with the defect band from the control sample. An RBS spectrum of a virgin or unimplanted sample was added for reference.

Damage was obtained from the RBS/channeled spectra utilizing the damage

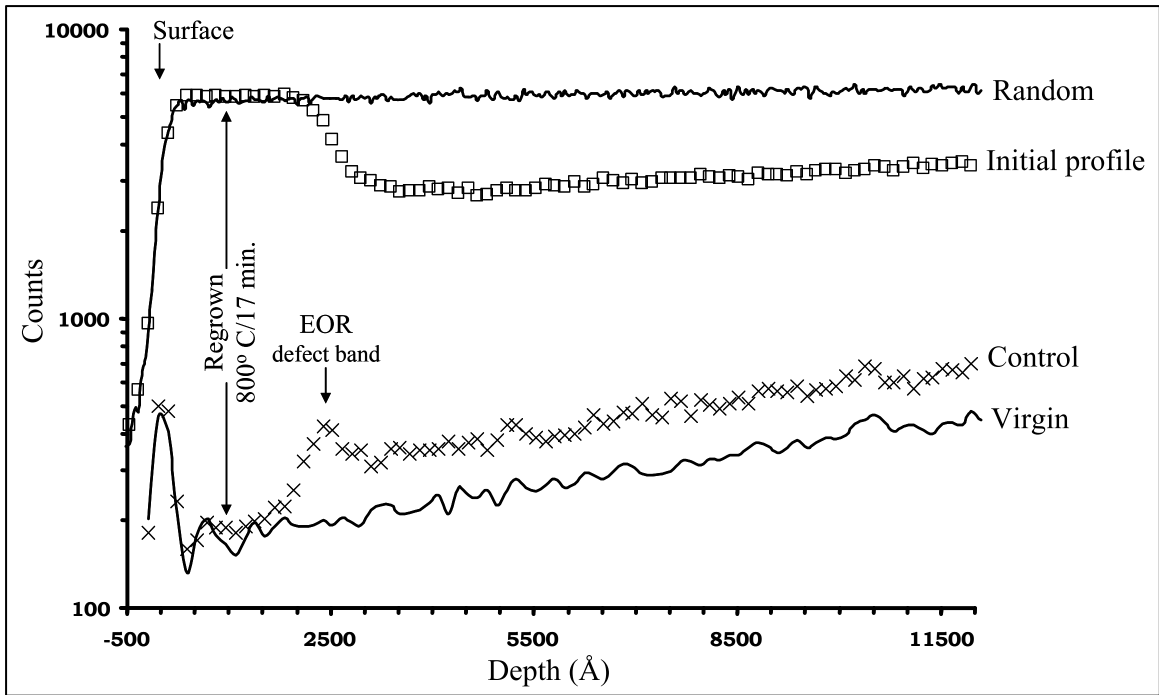

Figure 46. RBS/channeling spectra of both the initial and 800° C annealed Si samples amorphized-only. The continuous amorphous layer matches the random height the entire width of the layer and is regrown following the anneal at 800° C for 17 minutes; the scattering yield is consistent with the virgin spectrum. A residual defect band is left beyond the a-c interface upon regrowth of the layer.

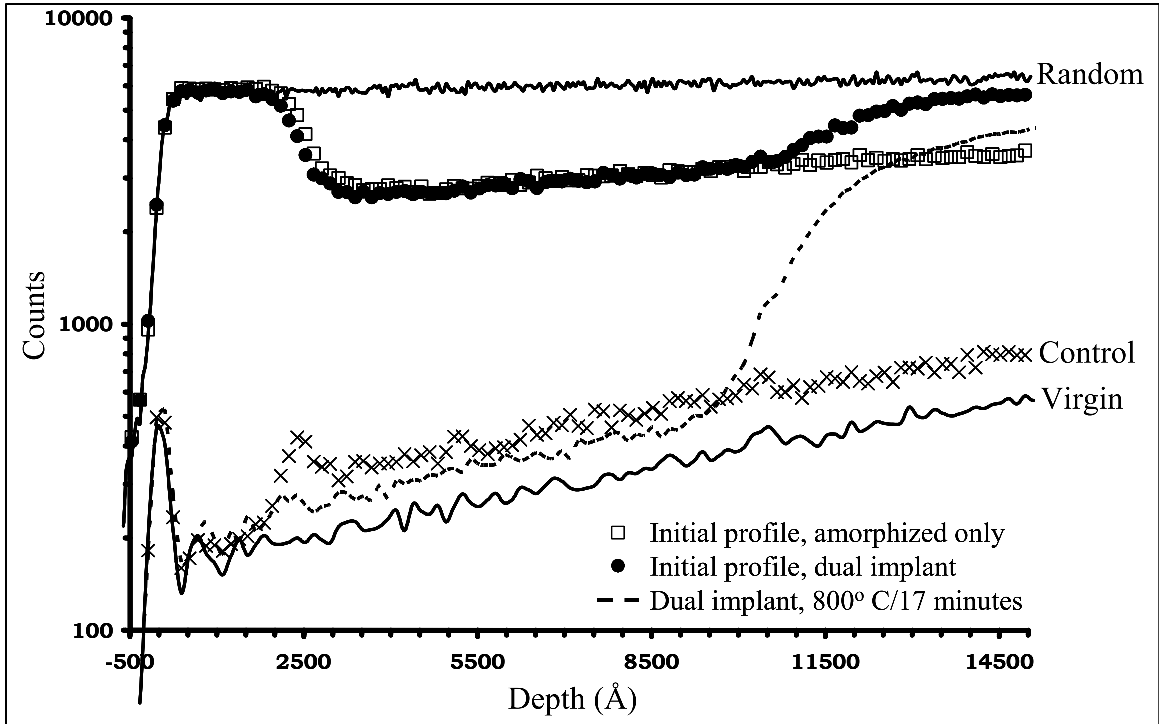

Figure 47. RBS/channeling spectra of the initial and 800° C annealed profiles of a sample amorphized only and dual implanted, with the random and virgin spectra added for reference. The EOR defect band is reduced for the dual implanted sample following annealing indicating recombination between the interstitials within the defect band following amorphization and MeV vacancies. The high scattering yield at R_p of the MeV implant is evident at a greater depth in the dual-implanted sample.

extraction routine shown in appendix I. For increasing fluence of the MeV implant, the data reveal a consistent decrease in the amount of residual damage below the original a-c interface within the lattice following annealing. This gradual decline in the ion-induced damage for increasing implant fluence continued until all of the damage at the a-c interface was removed; that is, no damage remained to the visibility of RBS. This indicates a synergistic effect between the two different implantations which suggests that the vacancies injected by 1.25 MeV ions recombine with the interstitial-type defects below the a-c interface.

The implants performed at 100° C show a trend of diminishing damage at the EOR. Two fluences, 5 and $6 \times 10^{16}/cm^{2}$, of MeV Si^{+}-ions implanted at 100° C prior to amorphization were analyzed with both RBS and XTEM following recrystallization of the amorphous layer. The material was pre-damaged with $5 \times 10^{16}/cm^{2}$, 1.25 MeV Si^{+}-ions at 100° C which corresponds to injecting a vacancy concentration of about $1 \times 10^{20}/cm^{3}$ (determined from TRIM[24]) into that near-surface layer. The MeV implanted sample was amorphized and annealed at 800° C for 20 minutes. In figure 48, the profile of the $5 \times 10^{16}/cm^{2}$ implanted sample (△), following annealing, exhibits regrowth of the amorphous layer along with a defect band which remains, although significantly reduced from that found below the a-c interface in the control sample. The implant of $5 \times 10^{16}/cm^{2}$, 1.25 MeV Si^{+}-ions did not produce a vacancy supersaturation sufficient to completely eliminate the excess interstitials below the a-c interface. However, increasing the implant fluence and, thus, increasing the relative vacancy concentration of 1.25 MeV Si^{+}-ions 20 % to $6 \times 10^{16}/cm^{2}$ produced a more successful result. The backscattered yield from the sample implanted with 1.25 MeV, $6 \times 10^{16}/cm^{2}$ Si^{+}-ions, amorphized and

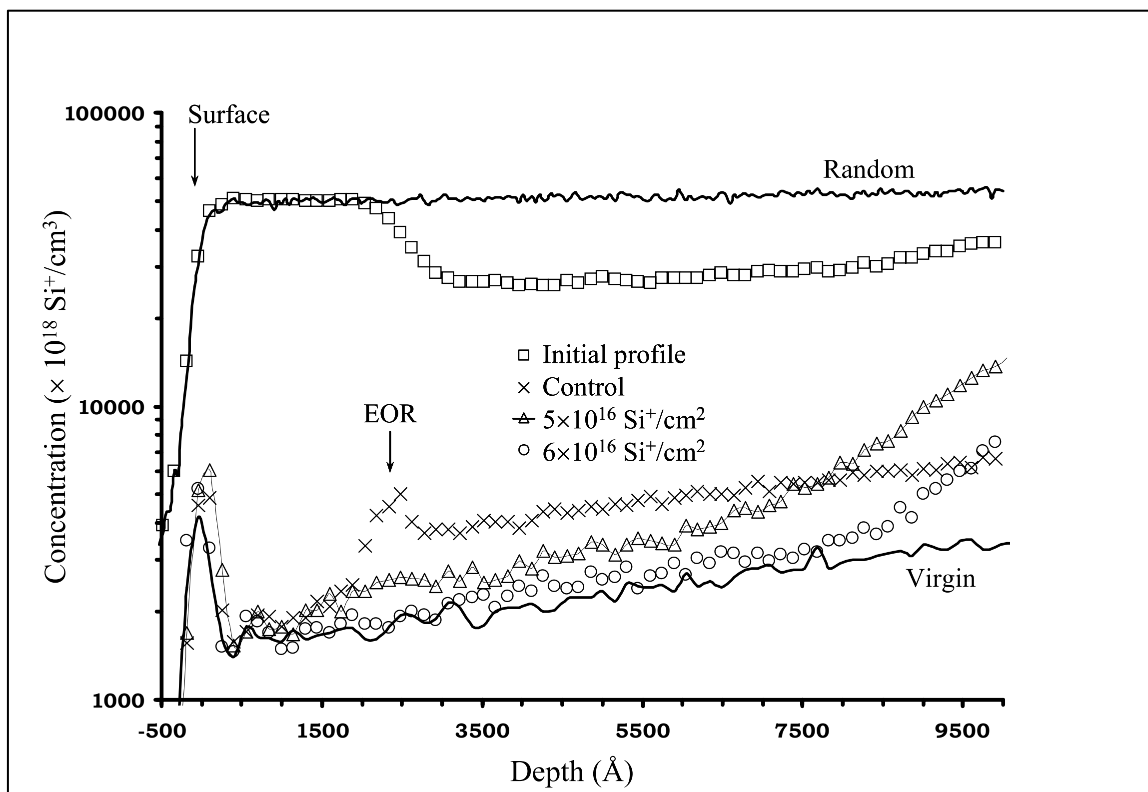

Figure 48. <100> aligned RBS/channeling of 1.25 MeV, 5 and 6×10^{16}/cm^2 Si$^+$-ions implanted in Cz-Si(100) at 100° C prior to an amorphizing implant of 70 and 140 keV, 10^{15}/cm^2 Si$^+$-ions at RT. The samples were annealed at 800° C for 20 minutes and compared to a control sample that has seen the amorphizing implant only with the same annealing conditions. The initial control profile, virgin, and random spectra are added for reference. Reprinted with permission from E. G. Roth, O. W. Holland, and J. L. Duggan in *Application of Accelerators in Research and Industry* (Proceedings of the Fifteenth International Conference on the Application of Accelerators in Research and Industry, 1998, Woodbury, NY), Jerome L. Duggan and I. L. Morgan, Editors, p. 804, Copyright 1999, American Institute of Physics.

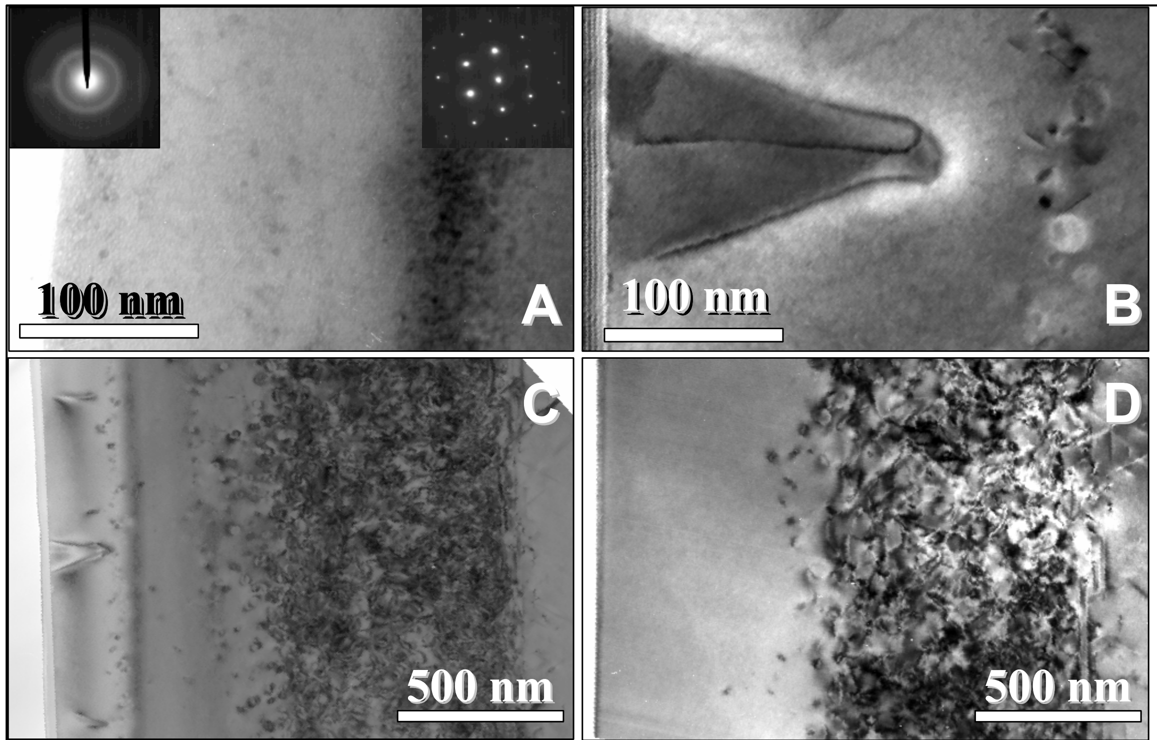

Figure 49. (a) Cross-section TEM image illustrating amorphization of Si by $10^{15}/cm^2$ Si^+-ions implanted at energies of 70 and 140 keV at RT. In (b) the sample of (a) was annealed for 20 minutes at 800° C: The dislocation band that forms upon recrystallization of the amorphous layer appears at the interface. In (c), the sample was pre-implanted with 1.25 MeV, $5\times10^{16}/cm^2$ Si^+-ions at 100° C, and subsequently implanted and annealed under the same conditions as in (b). Finally, (d) was produced with the same conditions as (c) except the initial high-energy implant fluence was increased to $6\times10^{16}/cm^2$. Reproduced from E. G. Roth, O. W. Holland, and A. Meldrum in *Silicon Materials Science and Technology 1998*, Proceedings of the Eighth International Symposium on Silicon Materials Science and Technology, PV 98-1, edited by H. R. Huff, H. Tsuya, and U. Gösele (NJ: Pennington, 1998), p. 938 by permission of The Electrochemical Society, Inc.

regrown was nearly identical to the aligned yield from a virgin sample [fig. 48]. Thus, to the sensitivity of the RBS/channeling technique, the excess defects residual below the a-c interface were successfully eliminated with the vacancy excess from high-energy implantation of $6 \times 10^{16}/cm^2$ Si^+-ions.

The RBS/channeling results for 5 and $6 \times 10^{16}/cm^2$ Si^+-ions implanted at 100° C (fig. 48) were confirmed with bright-field cross-sectional TEM (fig. 49). Figure 49a contains an XTEM image of the amorphous layer in a control sample without any prior MeV implant, and figure 49b is an image of the same sample after annealing at 800° C for 20 minutes. The amorphous layer was completely recrystallized with a dislocation band marking the location of the original a-c interface, as witnessed following RBS/channeling analysis (fig. 46 or 48). In addition, V-shaped threading dislocations extend to the surface of the control sample [fig. 49b]. In figure 49c, the sample was implanted with 1.25 MeV Si^+-ions at 100° C to a fluence of $5 \times 10^{16}/cm^2$, and then amorphized and annealed under the same conditions as the control sample in figure 49b. The band of dislocations at the a-c interface and the associated threading dislocations were clearly observed, although the defect density at the interface was lower than in figure 49b. The defects produced by the initial high-energy implant, centered near the projected range, extend from a depth of 6000 Å to over 1 μm. Finally, the sample in figure 49d was produced under the same conditions as the one in figure 49c except that the initial high-energy implant dose was increased to $6 \times 10^{16}/cm^2$. Notice the absence of any defect structure ahead of the damage at the projected range of the high-energy ions (about 1 μm) in figure 49d. Both the interfacial defects as well as threading dislocations (seen in fig. 49c) were successfully eliminated. Surprisingly, increasing the fluence of

high-energy ions by just 20 % increased the vacancy supersaturation sufficiently, such that the defects at the a-c interface were completely eliminated. XTEM data supported the above RBS/channeling data, such that the initial implant of 1.25 MeV, $6 \times 10^{16}/cm^2$ Si^+-ions prior to amorphization completely eliminated the defect band typically found below the a-c interface.[129]

RBS/channeling spectra from each fluence, between 1 and $6 \times 10^{16}/cm^2$, implanted at temperatures 100, 250, and 450° C are illustrated in figure 50, 51, and 52, respectively. Results of the RBS/channeling measurements of the dual implanted material show that an EOR defect band below the original a-c interface was removed by implanting a sufficient fluence of MeV Si^+-ions or by injecting a sufficient concentration of excess vacancy defects. As the fluence of the high-energy ions was increased, the resulting concentration of vacancy defects was increased. Increasing the vacancy concentration enhances the number of vacancies that interact with the EOR defects below the regrown amorphous layer. After the defect band is removed, the dual-implanted material returns to the virgin level, as seen in figure 48. Removal of the defect band typically found below the a-c interface occurred at different fluences for each of the implant temperatures.

The EOR damage extracted from the RBS analyses of the dual implants is plotted versus the implant fluence of MeV Si^+-ions for each implant temperature in figure 53. Note that the data have not been fitted. The lines connecting the data points are simply meant as a guide. The data exhibit a somewhat complicated trend for increasing implant temperature and dose. The results observed for the implant fluence of 1×10^{16} Si^+/cm^2 indicate a decreasing amount of residual damage with increasing implant temperatures.

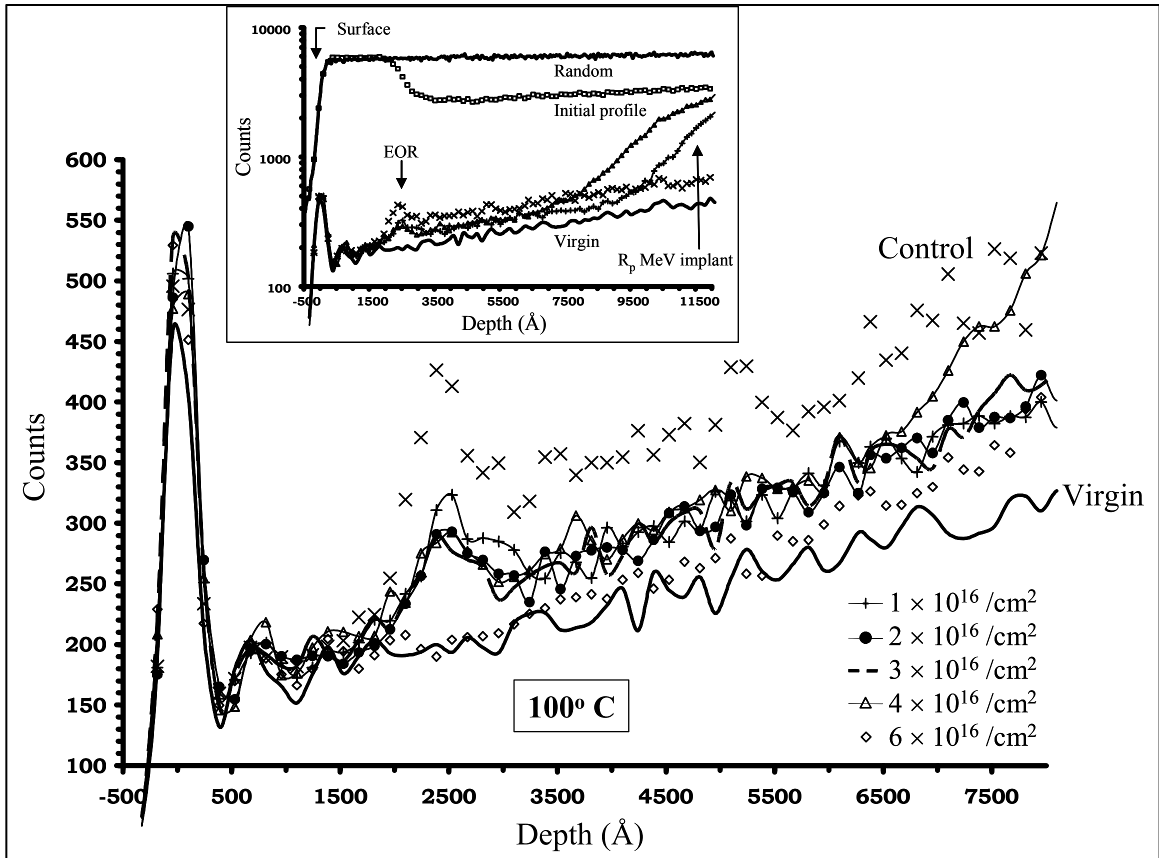

Figure 50. RBS/channeling spectra of Si implanted with 1.25 MeV Si^+-ions over a range of fluence 1 to $6\times10^{16}/cm^2$ at 100° C and amorphized with 70 and 140 keV, $10^{15}/cm^2$ Si^+-ions at RT. The EOR damage at the original amorphous-crystal interface is reduced for increasing MeV Si^+-ion implant fluence compared to the control. However, the defect band is not completely removed until a fluence of $6\times10^{16}/cm^2$ is implanted. The inset shows some typical characteristics including the EOR defect band, random, initial profile, virgin, and R_p of the MeV implant.

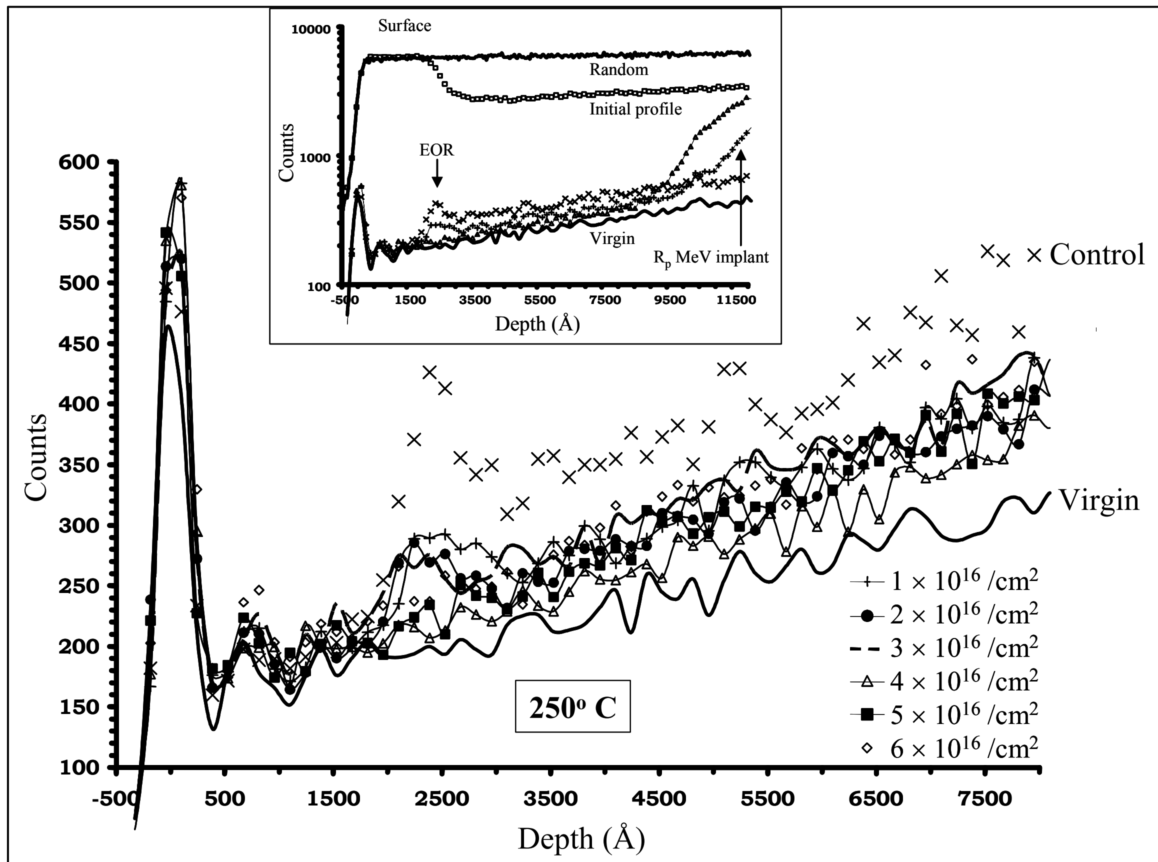

Figure 51. RBS/channeling spectra of Si implanted with 1.25 MeV Si^+-ions over a range of fluence 1 to $6\times10^{16}/cm^2$ at 250° C and amorphized with 70 and 140 keV, $10^{15}/cm^2$ Si^+-ions at RT. The EOR damage at the original amorphous-crystal interface is reduced for increasing MeV Si^+-ion implant fluence compared to the control. However, the defect band is not completely removed until a fluence of $4\times10^{16}/cm^2$ is implanted. The inset shows some typical characteristics including the EOR defect band, random, initial profile, virgin, and R_p of the MeV implant.

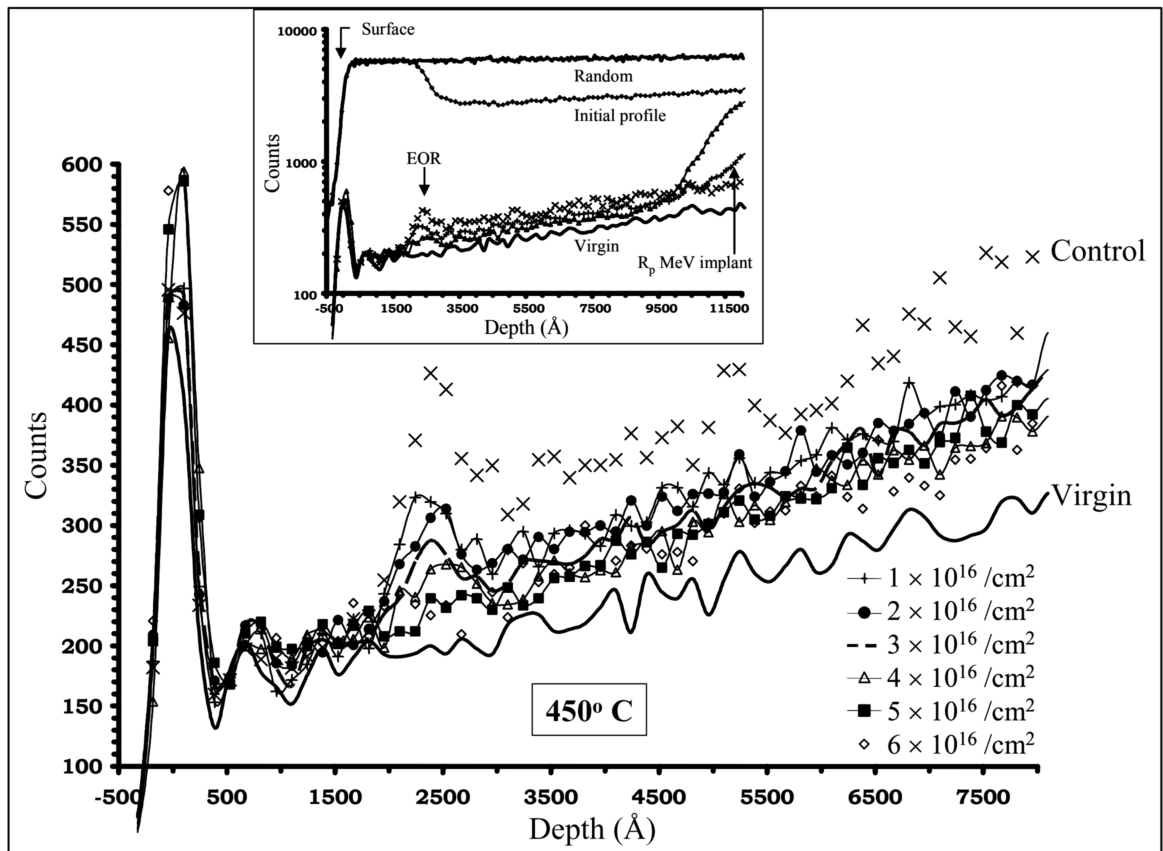

Figure 52. RBS/channeling spectra of Si implanted with 1.25 MeV Si^+-ions over a range of fluence 1 to $6\times10^{16}/cm^2$ at 450° C and amorphized with 70 and 140 keV, $10^{15}/cm^2$ Si^+-ions at RT. The EOR damage at the original amorphous-crystal interface is reduced for increasing MeV Si^+-ion implant fluence compared to the control. However, the defect band is not completely removed until a fluence of $5\times10^{16}/cm^2$ is implanted. The inset shows some typical characteristics including the EOR defect band, random, initial profile, virgin, and R_p of the MeV implant.

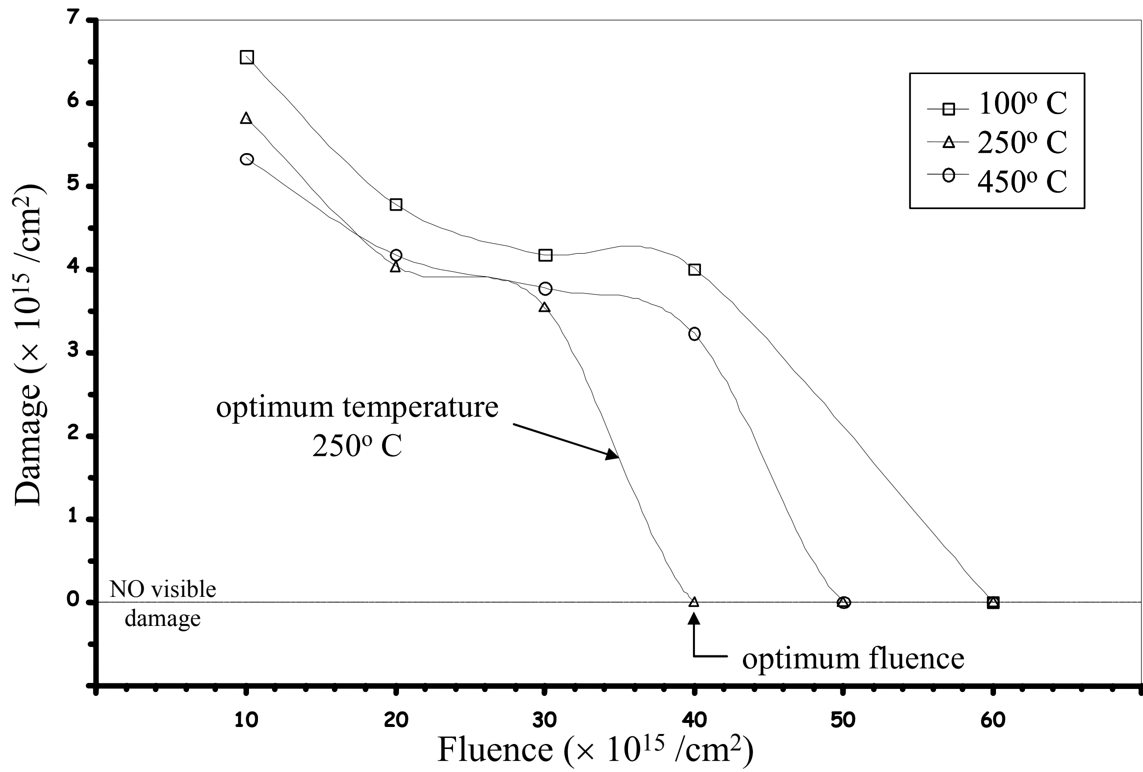

Figure 53. Damage from dual implants at 100, 250, and 450° C versus fluence of 1.25 MeV Si^+-ion implant.

TABLE V Damage visible following dual implantation.				
		Damage visible in RBS spectra Implant temperature (^{o} C)		
Fluence($\times 10^{16}/cm^2$)		100	250	450
actual	% increase			
3	50%	yes	yes	yes
4	33%	yes	no	yes
5	25%	yes	no	no
6	20%	no	no	no

However, as the fluence is increased from 2 to 6 × 10^{16} Si^{+}/cm^{2}, dual implants at 250° C [fig. 51] result in a lower damage yield than implants at both 100° C in figure 50 and 450° C in figure 52. Implants produced at 450° C reveal values of damage that are lower than those found for implantation at 100° C, but higher than the 250° C implants until the damage is removed with the dual implant process. No damage was detected following dual implantation with 4 × $10^{16}/cm^{2}$, 1.25 MeV Si^{+}-ions at 250° C and subsequent annealing. RBS spectra of samples implanted with 4 × $10^{16}/cm^{2}$, 1.25 MeV Si^{+}-ions at temperatures of 100, 250, and 450° C prior to the amorphizing implant illustrate this event in figure 54. A similar removal of the entire defect band at the a-c interface is achieved with a fluence of 6 × $10^{16}/cm^{2}$ MeV Si^{+}-ions implanted at 100° C and 5 × $10^{16}/cm^{2}$ MeV Si^{+}-ions implanted at 450° C. A synopsis of the damage found for all implanted fluences and temperatures of the MeV implant is included in table V. While it is clear that vacancy injection from implantation of high-energy ions provides a source of complementary-type defects to eliminate the interstitial defects at the a-c interface, the subtleties of the temperature and dose dependence are not obvious.

The quality of the regrown layer was studied by XTEM to image the sample implanted with 1.25 MeV Si^{+}-ions at 250° C to a fluence of 5 × $10^{16}/cm^{2}$ and annealed at

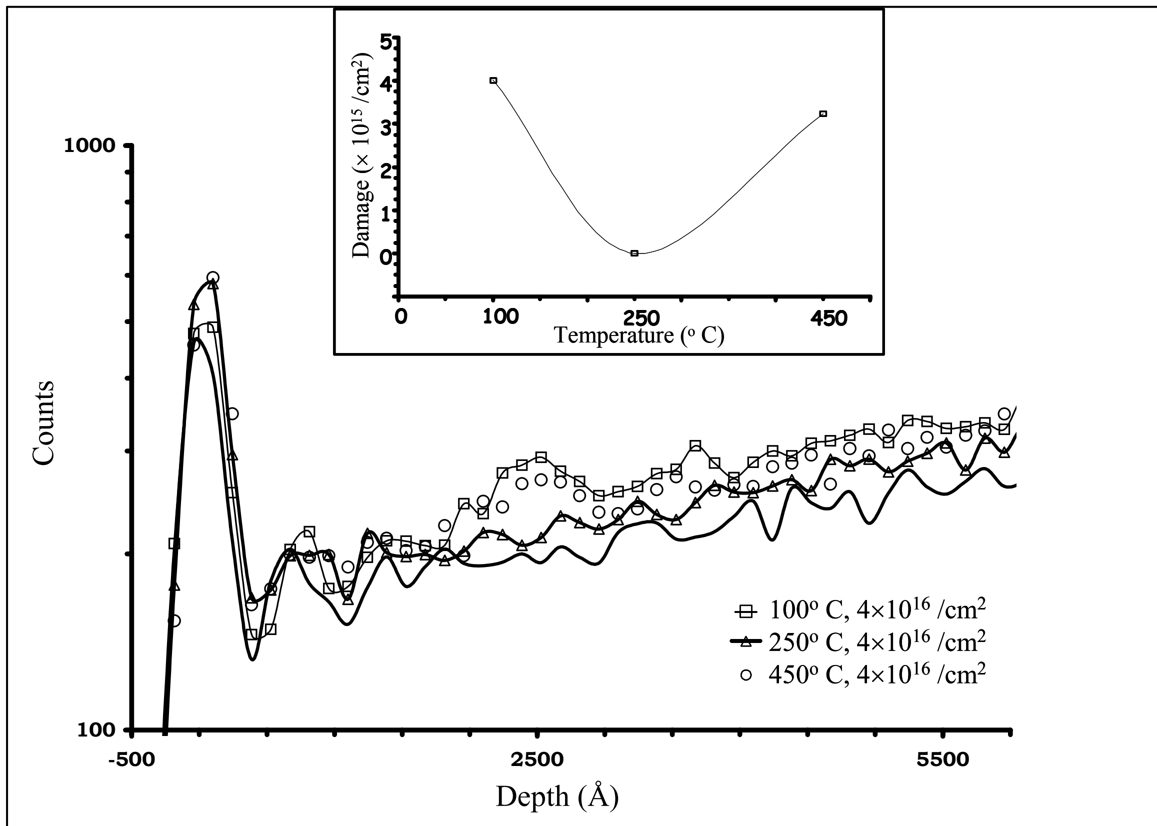

Figure 54. RBS/channeling spectra showing samples dual implanted at 100, 250, and 450° C where the scattering yield returned to the virgin level following SPEG of the amorphous layer generated in the sample pre-implanted with $4\times10^{16}/cm^2$.

800° C for 20 minutes. The area ahead of the interstitial-defect band at the projected range of the high-energy implant is completely void of any visible defects, i.e. no defect band is present, consistent with the RBS/channeling results. In addition, the samples with the same implant and annealed at 600° C led to an interesting discovery. The dual implantation technique effectively reduced the density of threading dislocations in the recrystallized region. The density of threading dislocations in a sample that had only seen the amorphizing implant (i.e., a control sample) had an approximate density of $4 \times 10^{13}/cm^3$ following SPEG. The density of threading dislocations in the dual implanted sample is reduced by at least an order of magnitude from that number. An upper limit to the density of threading dislocations found in the dual implanted sample is $8 \times 10^{11}/cm^3$. This result is somewhat surprising, since the accepted model for forming threading dislocations assumes they originate from dislocation loops intersected by the a-c interface.[94] As the amorphous layer is regrown, dislocations propagate from each segment of the half loop ultimately forming threading dislocations or hairpins that intersect the surface. The absence or reduced density of these threading dislocations in the MeV-implanted samples implies these intersected or half loops at the a-c interface are dissolved by the vacancy supersaturation prior to SPEG. Presumably, vacancies are released from complexes below SPEG temperatures and migrate to the half loops where they recombine at the edge of the loop.

PAS was used to profile the open-volume defects in the dual implanted Cz-Si samples in both the as-implanted state and following annealing at 600 and 800° C for 20 minutes. The S-parameter profiles are reported in Figure 55. The positron analysis results revealed some unexpected characteristics of the defect profiles within the SPEG

Si^+ (1.25 MeV, $5\times10^{16}/cm^2$) IMPLANTED INTO Cz-Si + AMORPHIZED

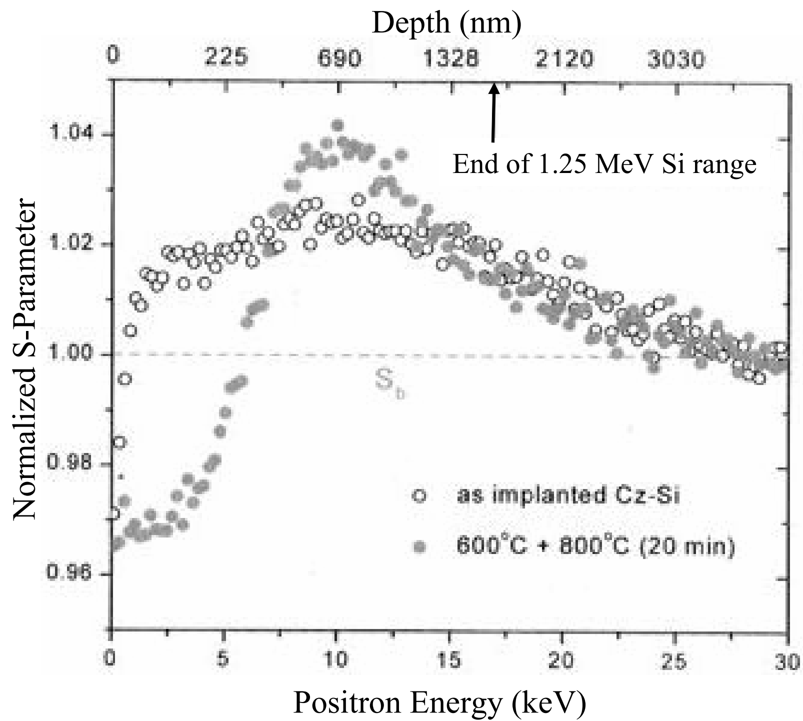

Figure 55. PAS data of dual-implanted Cz-Si both before and after annealing at 600 and 800° C for 20 minutes. Presence of vacancies illustrated over the entire near-surface layer until R_p of the MeV implant was reached. Upon annealing, the defects coarsen forming higher order vacancy defects. The pull-down in the S-parameter just below the surface is indicative of vacancy-impurity complexes.

layer following the thermal annealing process. The as-implanted sample produced a typical result. The open volume defects extend from the surface throughout the sample at an essentially constant level until a decrease in the open-volume defects occurs at R_p of the MeV implant where an interstitial excess is certain to exist. Incidentally, this result is further verification that TRIM responsibly simulates an effective model for the defects that are excess following ion implantation.

Below the original a-c interface and approximately mid-way to the EOR of the high-energy implant, the S-parameter increases above that observed in the as-implanted sample. The profile did not change significantly near the EOR, an indication much of the recombination of the spatially correlated defects (vacancies and interstitials) occurred during the implant process itself. This increase in the S-parameter is attributed to the ripening of the open-volume defects into larger clusters that are more stable and survive up to higher anneal temperatures. Lifetime measurements determined these defects are indicative of larger-size vacancy clusters containing between 5-8 atomic vacancies.[130,131] It is assumed the vacancy clusters have V_6 characteristics, thus, consist of 6 vacancies, since that vacancy aggregate is more stable in Si than other size vacancy clusters.[132]

Continuing towards the surface, the S-parameter did not reduce to 1 in the regrown layer, which would indicate that the regrown layer was returned to a highly crystalline state. However, the S-parameter exhibited an anomalous decline below the normalized value of 1 within the SPEG layer. The magnitude of the S-parameter may decline if either annihilation of the open-volume defects or interaction of the vacancy defects with impurities, e.g. oxygen, occurs within the lattice. V_nO_m complexes are known to pull the S-parameter down even below the value for virgin Si (1).[35] Note that n

and m represent the number of vacancies and atoms contained within the vacancy-oxygen complex. Lifetime measurements of the SPEG layer are about the same as the divacancy lifetime. The lowering of the S-parameter coupled with the lifetime data suggests divacancy-impurity complexes (V_2O_m) are formed within the regrown region.[131]

A surface oxide-native to any material left in air, was considered as a possible source of the oxygen that may be initializing V_nO complexes. The possibility of some of the oxygen being 'knocked in' from the surface to the amorphized layer during the implant process was considered. Prior to implantation, the samples were etched in a concentrated Hydrofluoric (HF) (5:1) solution before their introduction into an evacuated implant chamber. The HF etch was necessary to ensure the native oxide was etched off prior to the implant process. Consequently, careful sample preparation, maintained throughout this experiment, eliminated the surface oxide as a possible source of oxygen responsible for the behavior of the S-parameter following thermal annealing.

Several variations of the experiment were conducted to investigate this significant drop in the S-parameter. It was thought that perhaps the phenomenon was a result of impurity-vacancy complexes as stated above. Similar implants were performed in both Cz- and fz-Si to determine if intrinsic oxygen within the original Cz-Si material was responsible for forming the V_nO complexes necessary to generate the PAS results. The profiles from either substrate Cz- or fz-Si were essentially identical, thus, the decrease observed in the S-parameter could not be completely attributed to the impurity-vacancy, V_nO, complexes.

The conclusion drawn from this series of experiments was that the anomalous drop in the S-parameter within the regrown layer seen in both Cz- and fz-Si (100) does

not appear to be due to impurity levels within the regrown layer. Eliminating the sources of oxygen did not reverse this trend in the S-parameter. Interestingly, further analysis of these PAS results suggested the synergism between the high-energy implant and the amorphizing implant produced a regrown layer of higher crystalline quality than material amorphized only and regrown consistent with the XTEM study of the density of threading dislocations.

TED of boron: Defect probe

Implantation of boron was again utilized as a probe to test the effectiveness of the dual implant process in eliminating the excess interstitials residual below the a-c interface. If the dual implantation process is successful in eliminating the defects below the a-c interface, then no TED of boron should occur. The dual-implanted material consisted of Cz-Si (100) pre-damaged with 1.25 MeV, $6 \times 10^{16}/cm^2$ Si^+-ions at 100° C and subsequently amorphized with $10^{15}/cm^2$ Si^+-ions at both 70 and 140 keV at RT. As previously shown from RBS and TEM analysis, no defect band exists below the a-c interface. Boron was then implanted at 40 keV, $10^{14}/cm^2$ B^+-ions within the amorphous layer of the dual implanted material at RT. The boron distribution within the damaged layers was profiled with SIMS; following annealing performed in a conventional quartz-tube furnace under a flowing Ar-H (96-4%) ambient.

SIMS profiles of boron both before and after annealing are shown in figure 56. When compared to the initial profile, it is clear the distribution of boron within the amorphous layer of the dual implanted sample underwent little or no movement following an anneal at 800° C for 20 minutes for SPEG and dopant activation. This is compared to B implanted into a sample amorphized only (×), where significant TED (i.e.,

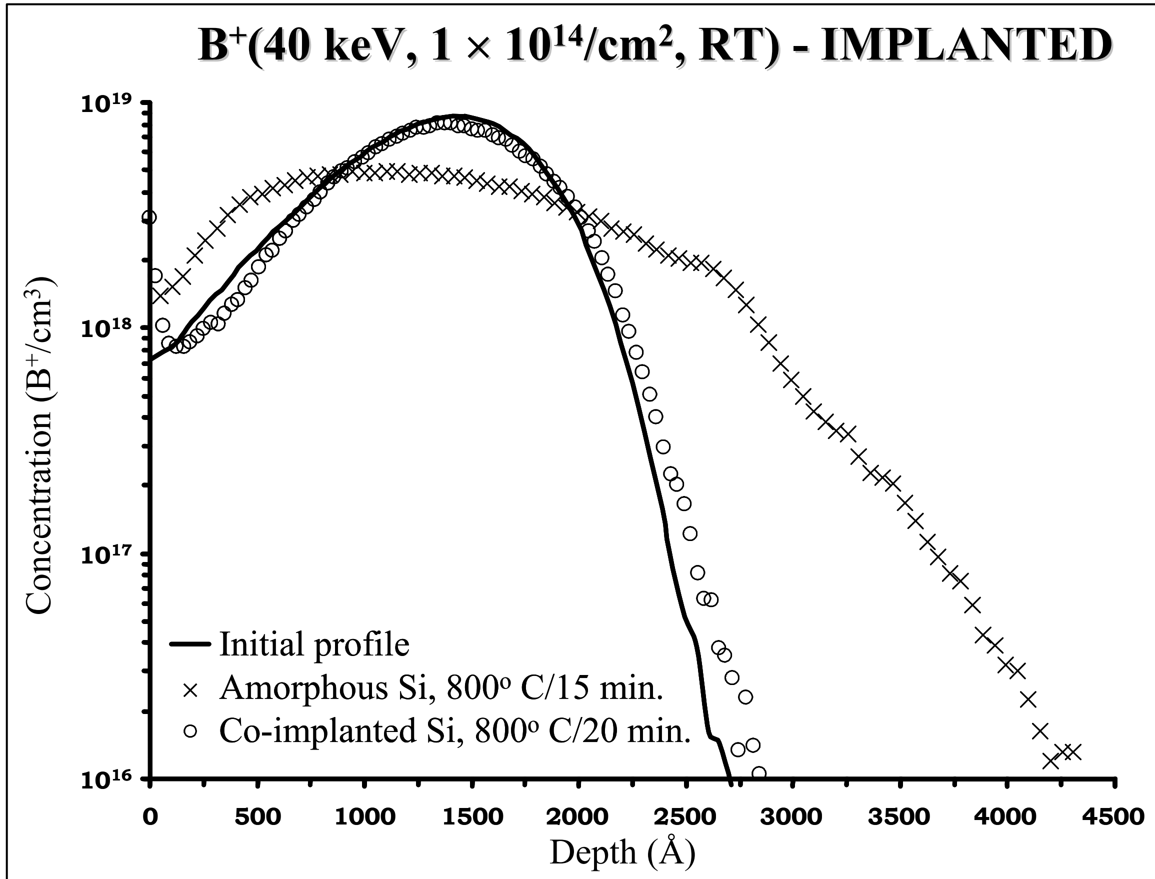

Figure 56. SIMS profiles of 40 keV, $10^{14}/cm^2$ B^+ implanted into amorphous Si at RT and annealed at 800° C for 15 minutes. The amorphous Si was pre-damaged with 1.25 MeV, $6\times10^{16}/cm^2$ Si^+-ions at 100° C and annealed at 800° C for 20 minutes. The initial profile is added for reference. Reprinted with permission from E. G. Roth, O. W. Holland, and J. L. Duggan in *Application of Accelerators in Research and Industry* (Proceedings of the Fifteenth International Conference on the Application of Accelerators in Research and Industry, 1998, Woodbury, NY), Jerome L. Duggan and I. L. Morgan, Editors, p. 804, Copyright 1999, American Institute of Physics.

a 1000 × enhancement) was observed following annealing at 800° C for 15 minutes.[108] This result confirms the elimination of interstitial defects below the a-c interface and thus corroborates the physical evidence provided by XTEM and RBS.

The above study reveals a dual implant process that may be used to substantially modify defect distributions and implanted profiles following post-implant thermal processing. This dual implant process involved pre-damaging the surface layer of a Si lattice with 1.25 MeV Si^+-ions prior to amorphizing the top layer. MeV ions inject a high concentration of vacancies in the vicinity of the EOR defects from the subsequent amorphizing implant. These resultant defect regimes, from the MeV implant, serve as a tool to promote artificial recombination of excess defects within the lattice. The synergism of the co-implants was exploited in an attempt to specifically remove interstitial defects below the a-c interface, known to drive TED of B implanted within an amorphous layer.[22,108,109,124]

The interstitials from the EOR loops below the interface recombine with vacancy defects released from small vacancy clusters during the implant or these interstitials in the EOR loops dissociate during the first few seconds of a post-implant thermal process and recombine with vacancies from dissociating vacancy clusters. The successful removal/reduction of EOR defects would prevent/limit extended defect formation, e.g. stable loops, threading dislocations, hairpins, etc, at the a-c interface and within the regrown layer. The elimination of these defects is shown to have a marked impact upon the quality of the SPEG. The density of threading dislocations, which span the region between the original a-c interface and the surface following SPEG, is reduced by this dual implant method. Removing excess defect complexes that contribute to the formation

of such defects enables the control over deleterious processes such as enhanced diffusion of a dopant species.

Further examinations of the order of implantation would provide insight concerning the nature of the defect clusters and their impact on dissociative mechanisms necessary for recombination to occur. Also, additional quantification data might be achieved with plan-view transmission electron microscopy (PTEM) to identify the size of the defect complexes in the near surface region of interest. Analysis of the magnitude of damage left at the amorphous crystal interface might validate RBS/channeling measurements contained in this work.

Summation

Three unique experiments explored methodologies to engineer excess defect populations left following ion implantation. High-energy ion implantation is a valuable tool for defect engineering because an excess vacancy population may be generated over an extended portion of the ion track, and it precedes the excess interstitials at R_p. It is in this near surface region where defects and processes must be managed to develop complex integrated circuit products. These vacancies injected in the near surface layer by high-energy ion implantation may be used as recombination sites for interstitial defects. Both attempts: The buried amorphous layer in SOI material and dual implants of MeV and keV ions, removed interstitial EOR defects on the crystalline side of the a-c interface. The original a-c interface was located in proximity of the excess vacancy population and recombination between the complementary defects was observed.

Pre-amorphization as a means of encompassing B^+ induced defects within the amorphous phase and controlling TED depended upon the implant parameters. However,

a substantial defect presence may be found below the a-c interface and the quality of the regrowth of the amorphous layer must be examined. If the implant parameters generated an amorphous layer where the EOR defects formed a perfect sink capturing all interstitials released, TED of boron was thus prevented. Pre-amorphization of the Si lattice in this study was not successful in creating a perfect sink and completely eliminating TED of boron implanted within an amorphous layer. Although the movement of the boron profile was impacted by varying the amorphizing implant conditions, such that a reduction of 1000 Å in the junction depth was achieved. In addition, the quality of the regrown surface layer was enhanced by removing the interstitial defect band at the a-c interface. The density of threading dislocations that spans the layer from the original a-c interface to the surface was reduced.

Co-implantation of high-energy ions and a boron implant moderately controlled the junction depth following thermal processing, but reported anomalies leave the mechanism for the co-implantation scheme in doubt. Anomalous out, and some inward diffusion were observed. Also, clustering of the boron and an aggressive channeling tail remained prevalent in the co-implanted samples due to B^+ implantation into a crystalline phase. Pre-amorphization is advantageous in addressing both of the latter concerns.

TED of the dopant ion, yielding increased junction depths, and threading dislocations that stretch from an a-c interface to the surface providing sources for leakage currents in a device are both significant phenomena that have been controlled through engineering of the ion-induced defects.

CHAPTER 7

CONCLUSIONS

A new paradigm in explaining final ion-induced defect distributions is shown with a simple model detailing defects that survive implantation processing and post-implant thermal cycling. An imbalance is found in regions where the concentration of one defect exceeds the concentration of the complementary defect. This preponderance of one defect over its complement is considered an excess within the lattice. Sources of excess defects include spatially uncorrelated Frenkel pairs, plus-one interstitial defects generated by the implanted ions, and vacancies due to sputtering at the surface during implantation. The majority of Frenkel pairs recombine immediately upon being created, but a small portion will become spatially separated due to the momentum transferred to interstitials during the collision. Therefore, a vacancy surplus is left in the near surface layer and extends to an interstitial excess that forms at the projected range of the implanted ions. The excess defect model contends deleterious effects attributed to ion induced damage residual in the implanted material are not caused by the total number of displacements following ion implantation, but rather the defects which remain in excess over their complementary defect are of concern.

Transport of ions in matter (TRIM)[24] simulations was used to model implantation into a variety of materials. The TRIM code is useful because it yields full damage cascades resulting from ion bombardment of a particular substrate with a high degree of accuracy without large processing time or hardware commitments. TRIM generates damage profiles without any dynamicity known to exist in an actual implanted sample. However, a subtraction routine was applied to TRIM profiles, more specifically, the

vacancy profile was taken from the interstitial distribution, generating a final defect distribution more closely related to a distribution that results following ion implantation at elevated temperatures or a post-implant anneal. This subtraction procedure simulates recombination amongst the spatially correlated defects leaving a bifurcated defect profile of vacancies preceding the interstitials beyond R_p of the implanted species or the excess defect profile within an implanted volume.

The most significant validation of the excess defect model is provided upon comparison of implants of 150 keV Si^+-ions at liquid nitrogen (LN_2) and 300° C temperatures to different fluences with TRIM simulations. Damage extracted from the implanted samples showed the total number of displacements from TRIM modeled the damage from the LN_2-implanted sample, while the excess defects detailed the damage observed in the sample implanted at 300° C. At colder temperatures, defects are less mobile and recombination between the Frenkel defects is not a priority. The total number of displacements generated by TRIM describes the disorder resultant from implants at colder temperatures. The excess defect model is applicable for implantation at room temperature (RT) or elevated temperatures. Furthermore, the experimental values of damage from an amorphizing As^+-implant were compared to TRIM calculations. The damage of the recoils added to the plus-one beyond the depth of the amorphous-crystalline (a-c) interface matched the experimental values of damage extracted from Rutherford backscattering spectrometry (RBS)/channeling spectra on samples amorphized with 120 keV, As^+-ions and regrown. Incidentally, the plus-one damage considered alone is greatly reduced from the damage extracted from the implanted

samples. The presence of excess defect regions was confirmed and modeling of these excess defects was successfully achieved through TRIM.

The defect study following dual implantation of high- and medium-energy Si^+-ions confirms the bifurcation in the damage distribution illustrating a vacancy-rich region exists ahead of an interstitial excess at R_p of the implant. Damage annealing was evident following implantation of high-energy Si^+-ions and medium-energy (200 keV) ions. These vacancies or “holes” left by the high-energy implant were filled with the excess interstitials (plus-one) from the subsequent keV implant. Once the holes were filled, damage from the implant of 200 keV Si^+-ions begins to grow, but it remained less than the damage residual in a sample implanted with 200 keV Si^+-ions only. It is also shown that the mechanism behind the defect interactions changes for implants of reversed order (keV ions implanted prior to MeV ions) once a critical concentration of interstitials is reached, anomalous damage growth results. The suggestion was that defects formed more stable configurations, thereby resisting recombination. Further study of these defect interactions will illuminate the mechanism of subsequent implantation on existing defect structures within the implanted volume.

A defect model delivers if it accurately describes or anticipates the source and locale of resultant defects. Upon validation, the excess defect model was applied to affect defect engineering on ion-induced defects within an implanted material. The concept of defect engineering involves reducing or eliminating ion-induced defects through secondary implants or timely thermal procedures. For instance, excess defect populations are overlapped where recombination between complementary defects or annealing of the

implant damage might occur. Dual implantation scenarios and amorphization were applied for the purpose of engineering defects and impacting the final defect distribution.

Transient enhanced diffusion (TED) of implanted boron was observed with or without pre-amorphization of Si. It has been argued that the enhanced diffusion in pre-amorphized samples is either attributed to excess interstitial-type defects located beyond the a-c interface or properties inherent with the regrown material. Silicon-on-insulator (SOI) material was used in a unique approach to control these defects and clarify the mechanism for diffusion of marker layers within amorphized regions. The presence of a buried Si/SiO_2 interface in the SOI material allowed the sample to be amorphized completely to this interface. However, the implant conditions were manipulated to leave a crystalline region at the surface to seed crystallization of the amorphous layer from the surface into the bulk.

The interstitial defects on the crystalline side of the a-c interface were consumed by the vacancy excess residual from high-energy ion implantation, thereby eliminating the only remaining source of interstitial defects that might contribute to the enhanced diffusion of the boron dopant. An RBS/channeling profile of the regrown material shows the backscattered yield of the implanted specimen was reduced to a level similar to unimplanted material. Enhanced diffusion of boron previously observed in pre-amorphized Si was completely eliminated. The creation of a buried boron marker layer by ion implantation was possible through this front amorphization technique using SOI material. This result confirms the mechanism for enhanced diffusion of B marker layers encompassed completely within an amorphous layer is the flux of interstitial defects from

the end-of-range (EOR) beyond the a-c interface and not an intrinsic property of the regrown layer.

Different amorphizing conditions were used to investigate how alteration of the magnitude and configuration of EOR defects impacted TED of a B marker within a traditional amorphous layer. Amorphizing silicon with $^{30}Si^{+}$-self ions prior to implantation of boron eliminated both ion-channeling effects and clustering of the implanted boron, which immobilizes boron near the peak of the implanted profile. While amorphization of the Si layer did not eliminate TED of boron, even though the plus-one interstitials were incorporated within the amorphous layer, the transient was reduced by a factor of two over that in a B^{+}-only implanted sample. It is interesting to note the degree of enhanced diffusion may be affected by simply adjusting the amorphization parameters. In addition, a second technique included co-implanting a sufficient dose of high-energy Si^{+}-self ions with B^{+}-ions. TED of boron was contained so that the junction depth was not altered. However, the particular mechanism involved in the recombination of the vacancies with the plus-one state and the anomalous out-diffusion of boron towards the surface requires further study to understand. The second technique of engineering defects was more successful in mediating TED of boron.

Enhanced diffusion within a traditional amorphous layer is attributed to the defects typically found beyond the original a-c interface following regrowth of an amorphous layer continuous to the surface. Furthermore, in the front amorphization experiment, TED was eliminated upon the removal of this EOR defect band. Synergism between initial high-energy implants and subsequent medium-energy implants was used to develop a novel implant process to eliminate the interstitial defect band following

regrowth of a traditional amorphous layer. This defect band contributes to TED of a B marker implanted within the amorphous layer. The high-energy ions pre-formed a vacancy-rich layer in the region of the a-c interface which provided recombination sites for ion-induced interstitial defects from subsequent implants. From RBS and TEM measurements, it is clear that the overlap of complementary-type defects reduced and for higher implant fluences of the high-energy ions eliminated the defect band typically formed at the a-c interface following annealing at 800° C for 20 minutes. Vacancies injected into the near-surface layer by MeV implantation were used to promote the recombination with interstitial defects residual below the a-c interface following SPEG. The removal of this defect band was confirmed with SIMS analysis of a B marker implanted within the amorphous layer of the dual implanted sample where the EOR defects were eliminated. No movement of the B distribution was observed following a diffusion anneal at 800°C for 20 minutes. This confirmed the absence of any source of interstitial defects left below the a-c interface to drive enhanced diffusion following a thermal process.

It would appear that the implant temperature of the high-energy implant did not dominate the elimination of the interfacial defect band. Changing the implant temperature from 250 to 100° C only required a 20 % increase in dose to produce the equivalent result. The crystalline quality of the regrown layer was improved with the removal of the defect band. Cross-sectional TEM images indicated that the mechanism of using high-energy ion implantation to eliminate interfacial defects also reduced the density of threading dislocations found within the recrystallized layer by approximately an order of magnitude.

A simplified perspective of ion-induced defects following implantation at room or elevated temperatures or a post-implant thermal process resulted with an excess defect model. This model was supported through the successful comparison of TRIM simulations and damage observed from ion implantation procedures. The predictive capability of the excess defect model was shown by manipulating ion-induced damage through defect engineering schemes. These techniques either control or eliminate defective regions and the final defect distribution, in order to achieve a more defect free lattice or reduce the defects prior to their stabilization.

APPENDIX A

Damage extraction routine for RBS/channeling

The use of ion channeling in conjunction with Rutherford backscattering spectrometry (RBS) enables both compositional and structural information to be extracted from the interaction of ions with atoms in a solid. In general, the energy spectrum of the backscattered ions can be calibrated so that the each channel within the spectrum is correlated to either the backscattered ion energy or the scattering depth of the ion. In an ion channeling spectrum, the rise in the backscattered ion yield from a damaged region within a single-crystal sample above that from a virgin crystal provides a measure of the numbers of displaced or interstitial-type atoms within the lattice. This increase in the backscattered yield is localized, in the case of ion-induced damage, to a disordered zone within the crystal, which spans the range of the ions.

The damage concentration and distribution can be extracted from an RBS/channeling spectrum as follows. First, the incident flux is assumed to comprise two parts: the random fraction of the beam, $\chi_R(x)$, and the channeled fraction, $(1-\chi_R(x))$. As the names imply, the channeled fraction comprises those ions channeled within the crystal while the random ones are not channeled and are scattered by the lattice atoms as if they were randomly located. It is assumed that the channeled ions are scattered only by the displaced atoms. The normalized scattering yield of the channeled ions is thus given by;

$$(1-\chi_R(x))\frac{N_d(x)}{N} \qquad [1.1]$$

where $(1-\chi_R(x))$ is the channeled fraction and $N_d(x)$ is the damage distribution, and both are measurable parameters.[30] N is the bulk density in atoms/cm^3. The total

normalized yield, $\chi_T(x)$, thus contains two components: the contribution from the channeled fraction given by equation [1.1] and that from the random component, $\chi_R(x)$. Thus, the total yield may be written as;

$$\chi_T(x) = (1 - \chi_R(x))\frac{N_d(x)}{N} + \chi_R(x) \qquad [1.2]$$

The above equation may be solved for either $N_d(x)$ or $\chi_R(x)$, depending on given or known information. The above equation, [1.2], has been solved for $N_d(x)$ below,

$$N_d(x) = N\frac{(\chi_T(x) - \chi_R(x))}{(1 - \chi_R(x))} \qquad [1.3]$$

However, this equation can not be used to calculate the depth distribution of the displaced atoms, $N_d(x)$, until a method of determining the random fraction is devised. The random fraction is not constant but depends upon the penetration depth of the ions due to dechanneling. Small angle collisions of the channeled ion with the displaced atoms within the lattice can result in sufficient scattering of the ions to remove them from the channels. Thus, as the channeled ions penetrate the damage region, they are continuously transferred into the random fraction as a result of small-angle scattering with the displaced atoms. This should be contrasted with the direct scattering peak given by equation [1.1]. Thus, the depth dependent dechanneling, i.e. the increase in $\chi_R(x)$, must be determined before equation [1.3] can be used to determine $N_d(x)$.

A computer routine was written in visual basic for applications (VBA) to extract the damage profile from the channeled ion spectrum. It accurately determines the ion-induced lattice damage[29,30] by utilizing a routine which extracts the dechanneled fraction from the spectral data.[29,30] The method is as follows. First, the region of interest where

damage should be extracted from a profile containing damage is identified. The direct scattering yield, given by equation [1.1], is initially determined using a linear (trapezoidal) approximation for dechanneling. The endpoints used to generate this line were by the scattering yield located just below the damaged region, and the minimum yield from a virgin crystal, $\chi_{\min}$. The minimum yield is defined as the aligned yield from the near surface of a target. Thus, the straight-line interpolation from $\chi_{\min}$ to a point just below the damage curve of the implanted sample provides the initial estimate of $\chi_R(x)$ used to calculate $N_d(x)$. If the scattering yield and location of the endpoints are given, respectively, by y_i and x_i, then the slope of the straight-line approximation is given by;

$$m = \frac{(y_2 - y_1)}{(x_2 - x_1)} \qquad [1.4]$$

and the straight line approximation of $\chi_R(x)$

$$y_n = m(x_n - x_1) + y_1 = \frac{(y_2 - y_1)}{(x_2 - x_1)}(x_n - x_1) + y_1 . \qquad [1.5]$$

The code is given in the following.

```
        slope = ((Raw(Pnt2) - Raw(Pnt1)) / (Depth(Pnt2) - Depth(Pnt1)))
        Cells(1049, ColDepth).Offset(0, 1) = slope
  For f = (Pnt2 + 1) To (Pnt1 - 1)
            Background(f) = ((slope * (Depth(f) - Depth(Pnt1))) + Raw(Pnt1))
            Damage(f) = Raw(f) - Background(f)
            Cells(f, CR).Offset(0, 2) = Background(f)
            Cells(f, CR).Offset(0, 3) = Damage(f)
        Next f
```

An example of the straight-line may be seen in figure 57, profile B. From this straight line, $N_d(x)$ is calculated.

$N_d(x)$, calculated from the straight-line approximation, is then used in a reiterative cycle to generate an improved value for $\chi_R(x)$ (which is then used to calculate a better estimate of $N_d(x)$). In this process, $\chi_R(x)$ is still constrained by the yield at the endpoints, which establishes its values at the boundaries of the damaged zone. The variation between the endpoints is then determined by requirement that it be proportional to $N_d(x)$. This is a reasonable and only assumes that the damage morphology is similar over the entire distribution. A more accurate value of $N_d(x)$ is figured and the reiterative process continued until $N_d(x)$ approaches a stationary value.[30]

```
            'Proportionality Factor:
    Proportion_Factor = ((Raw(Pnt2) - Virgin(Pnt2)) / Total_Damage)
            'Damage counts in 1 channel divided by the total integrated
            damage_counts.
   For K = StartAtChan To (Pnt2 + 1) Step Increment
            'First, must average height of Random spectrum
            'Calculating damage in channel (row) k.  Dechanneling...
    Dechan_Yield = Dechan_Yield + (Damage(K) * Proportion_Factor)
            'Direct scattering yield -- arbitrary units (counts)
    Extract_DirSc(K) = ((Raw(K) - Background(K)) / Channeled_Fraction)
    Cells(K, CR).Offset(0, 5) = Extract_DirSc(K)
            'Integrating direct scattering counts
```

```
Extract_ScCnts = Extract_ScCnts + Extract_DirSc(K)

Cells(1051, ColDepth).Offset(0, 5) = Extract_ScCnts

        'Concentration of damage in units of atoms/cm3

Extract_Damage(K) = ((AtomicDensity / Random_height) * Extract_DirSc(K))

        'Damage concentration extracted will have units: 1 × 18 atoms/cm3

Cells(K, CR).Offset(0, 6) = (Extract_Damage(K) / 1E+18)

        'Integrating damage, units:  atoms/cm2

ChgDep = ((Depth(K - 1) - Depth(K)) * 0.00000001)          'Convert Å to cm

        'Depth over which integrating damage (units:  cm).

New_Total_Damage = New_Total_Damage + (Extract_Damage(K) * ChgDep)

Cells(1051, ColDepth).Offset(0, 3) = New_Total_Damage

        'Calculate dechanneling in channel k-1, including effect of damage in
        channel k.

o = K – 1                                                  'Channel k-1

Background(o) = Dechan_Yield + Virgin(o)

If o >= (Pnt2 + 1) Then

Cells(o, CR).Offset(0, 4) = Background(o)

Else: GoTo 21

End If

21      If Random_height > 0 Then

            Channeled_Fraction = (1 - (Background(o) / Random_height))

        Else

            Channeled_Fraction = 1
```

```
        End If
    Next K
```

The dechanneled profile is shown in figure 57, profile C as the background trace (○), along with the RBS profile of the implanted Si (-) and the straight-line approximation [fig. 57, profile B]. The resulting damage profile (hatched area in fig. 57) is plotted in figure 58.

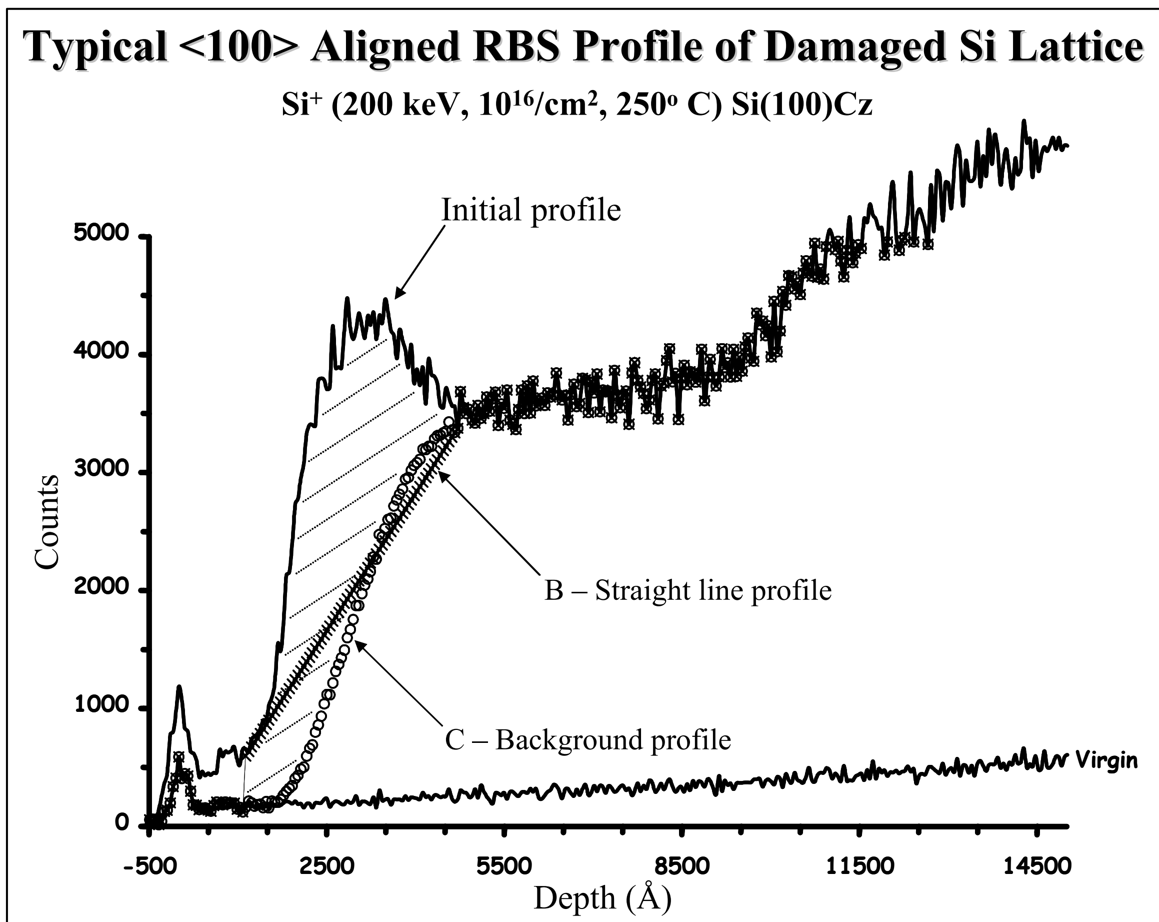

Figure 57. RBS/channeled spectrum containing the different profiles, straight-line, profile B, and background, profile C, generated through the damage extraction routine. The damage is represented by the hachured area.

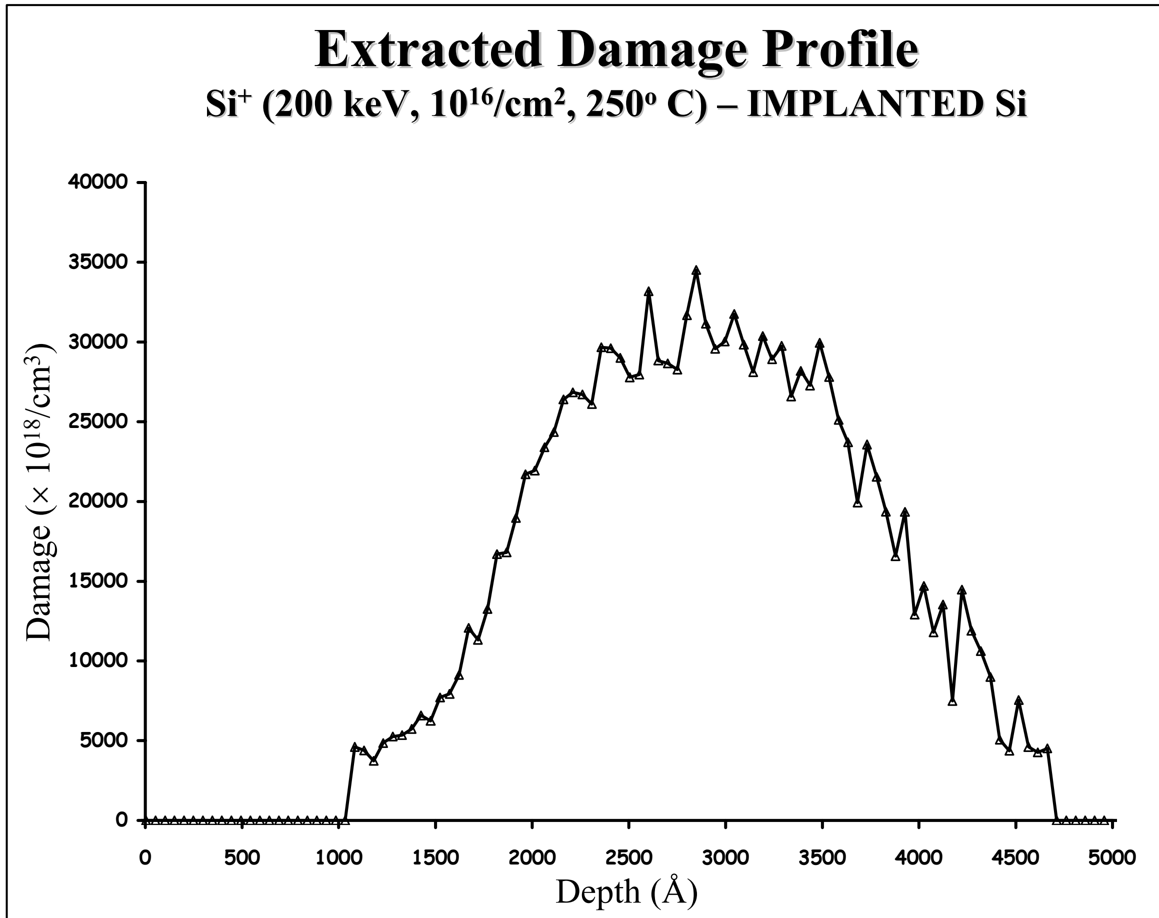

Figure 58. Damage extracted from RBS/channeled spectrum in figure 57 (hachured area).

APPENDIX B

Physics of stopping cross sections for particles traversing a solid

The penetration of the ions in a target is described according to two component, either nuclear or electronic scattering, both separate and distinct. When an ion with an initial energy of E_o traverses a target, the ion's energy is reduced through collisions with target nuclei (elastic scattering) and target electrons (inelastic scattering). The probability of scattering with a target nucleus is governed by nuclear stopping cross-sections. The nuclear component is treated separately because the heavy recoiling target nucleus is presumed unconnected to the lattice throughout the passage of the ion. The elastic energy transferred to the target nucleus may then be treated as simple kinetic scattering of two heavy screened particles.[2,9]

The elastic scattering problem may be solved in either of two coordinate systems: center-of-mass (CM) system or laboratory frame. A relationship exists (equation [2.4]) between the scattering angle linking the two frames of reference. The energy transferred in the CM coordinate system has a $\sin^2\frac{\theta}{2}$ dependence on the scattering angle, θ. The energy transferred is contained in equation [2.1],

$$T = \frac{4M_1M_2}{(M_1+M_2)^2}E_o\sin^2\frac{\theta}{2} = \frac{4E_CM_C}{M_2}\sin^2\frac{\theta}{2} \qquad [2.1]$$

where M_1 and M_2 are the masses of atoms. The right hand side of the equation may be written for the energy transferred following the substitution of the reduced mass defined in CM coordinates,

$$M_C = \frac{M_1M_2}{(M_1+M_2)} \qquad [2.2]$$

and the initial kinetic energy in the CM coordinate system,

$$E_C = \frac{1}{2} M_C v_o^2. \qquad [2.3]$$

Note that the scattering angle in CM coordinates is related to the laboratory frame through

$$\vartheta = \arctan\left[\frac{\sin\theta}{(\cos\theta + \frac{M_1}{M_2})}\right] \qquad [2.4]$$

A relationship for the scattering angle may be devised by simplifying the problem of a two-body collision to a particle in a single central-force scattering to a two-body, central-force scattering event. This interpretation is possible only if two conditions are satisfied. The first condition is that the potentials of each are spherically symmetric and do not vary with time or either particle's velocity, and the second condition is the conservation of energy and angular momentum throughout the entire system. With these conditions, restating E_C in polar coordinates yields $E_C = \frac{1}{2} M_C (\dot{r}^2 + r^2\dot{\theta}^2) + V(r)$. The conservation of angular momentum, $J_C = M_C r^2 \dot{\theta}$, is derived in polar coordinates. Solving these equations for the conservation of energy and momentum culminates into a relationship for the scattering integral, θ, as a function of dr. This allows the direct calculation of the energy transferred for any central force potential, $V(r)$. The conservation of energy equation is rearranged to find $\frac{dr}{dt}$,

$$\dot{r} = \frac{dr}{dt} = v_C \left[1 - \frac{V(r)}{E_C} - \left(\frac{p}{r}\right)^2\right]^{1/2}. \qquad [2.5]$$

J_C is eliminated from the conservation of angular momentum equation using the

constant of angular momentum $J_C = M_C v_C p$, where p is the impact parameter. The manipulation results in an equation for $\frac{d\theta}{dt}$,

$$\dot{\theta} = \frac{d\theta}{dt} = \frac{v_C p}{r^2} \qquad [2.6]$$

Combining equations [2.5] and [2.6] produces the relationship $\frac{d\theta}{dr}$,

$$\frac{d\theta}{dr} = \frac{d\theta}{dt} \cdot \frac{dt}{dr} = \frac{p}{r^2\left[1 - \frac{V(r)}{E_C} - \left(\frac{p}{r}\right)^2\right]^{1/2}}. \qquad [2.7]$$

Integrating equation [2.7] gives the desired function of the scattering angle, θ, in terms of dr for the evaluation of the final scattering angle in terms of the potential, $V(r)$, the initial energy, E_C, in the CM coordinate system, and the impact parameter, p:

$$\theta = \pi - \int_{-\infty}^{\infty} \frac{pdr}{r^2\left[1 - \frac{V(r)}{E_C} - \left(\frac{p}{r}\right)^2\right]^{1/2}} \qquad [2.8]$$

or

$$\theta = \pi - 2\int_{r_{\min}}^{\infty} \frac{pdr}{r^2\left[1 - \frac{V(r)}{E_C} - \left(\frac{p}{r}\right)^2\right]^{1/2}}, \qquad [2.9]$$

where $r_{\min}$ is the distance of closest approach during the collision. The energy transferred to a target atom is now a function of p and E and is determined by substituting the solution of equation [2.9] into equation [2.1] for T.

Many statistical approaches to the interatomic interaction have been applied to

calculate the nuclear stopping. The Sommerfield approximation to the Thomas-Fermi potential[75], the Moliere approximation[76], the Lenz-Jensen[77], and the Bohr potential[55] remain most well known of these statistical models. The interatomic potential consists of a Coulombic term $\frac{1}{r}$ multiplied by a "screening" function. For two-atom collisions, the potential is found in equation [2.10],

$$V(r) = \left(\frac{Z_1 Z_2 e^2}{r}\right)\Phi \qquad [2.10]$$

The coulombic term represents the positive point nucleus and the electronic screening reduces its value for all atomic radii. The search for an accurate interatomic potential has extended over 80 years and is reviewed in ref. 78. A good interatomic potential may be calculated using a universal screening potential of

$$\Phi_{Universal} = .1818e^{-3.2x} + .5099e^{-.9423x} + .2802e^{-.4028x} + .02817e^{-.2016x}, \qquad [2.11]$$

where $x = \frac{r}{a_u}$ and $a_u = \frac{.8854a_o}{(Z^{2/3} + Z^{2/3})}$.[78] The universal screening potential is an improvement over the Moliere approximation[76] to the Thomas-Fermi potential found by Wilson, et al.[61] in 1977 to be more suitable for nuclear stopping than treatments by Bohr[55] or Sommerfield[75]. The original paper for the simulation of ion transport, TRIM, by Biersack and Haggmark[24] applied the Moliere approximation for nuclear stopping and energy loss at low energies. In fact, application of the universal screening potential for low energies maintains the accuracy of MARLOWE[63], and when combined with other computer efficiencies reduces computation time by one order of magnitude.[70]

An accurate universal screening potential has been identified, equation [2.10], with the screening function found in equation [2.11]. In order to assess the scattering

angle collectively and independent of ion, target parameters or individual atomic variables, Z_1, Z_2, M_1, and M_2, the equation for the scattering angle, θ, is converted to equation [2.12]:

$$\theta = \pi - 2\int_{r_o/a}^{\infty} \frac{bdx}{x^2\left[1 - \frac{\Phi(x)}{x\varepsilon} - \left(\frac{b}{x}\right)^2\right]}, \qquad [2.12]$$

with substitutions of $x = \frac{r}{a}$, $b = \frac{p}{a}$, $\varepsilon = \frac{E_C}{\left(Z_1 Z_2 e^2 / a\right)}$, and $V(r) = \left(\frac{Z_1 Z_2 e^2}{r}\right)\Phi\left(r/a\right)$.

The energy loss per unit length is $\frac{dE}{dR}$. This energy loss is related to the nuclear stopping cross-section by

$$\frac{dE}{dR} = NS_n(E), \qquad [2.13]$$

where N is the atomic density of the target. The nuclear stopping power, $S_n\left(E\right)$, is the average energy transferred when summed over all impact parameters

$$S_n(E) = \int_0^{\infty} T(E,p) 2\pi p dp. \qquad [2.14]$$

Employing equation [2.1] for T yields

$$S_n\left(E\right) = 2\pi \frac{4M_1M_2}{(M_1+M_2)^2} E_o \int_0^{p_{\max}} \sin^2\frac{\theta}{2} pdp = 2\pi\gamma E_o \int_0^{p_{\max}} \sin^2\frac{\theta}{2} pdp, \qquad [2.15]$$

where a substitution of the CM transformation factor $\gamma = \frac{4M_1M_2}{(M_1+M_2)^2}$ generates the final right-hand equality. In addition, the upper limit, $p_{\max}$, is the addition of the two atomic radii. This simplification is possible because the interatomic potential is zero for values

greater than $p_{\max}$, as well as no transfer of energy.

Equation [2.15] is the nuclear stopping power in physical units. Lindhard, et al.[59,136] in their calculation of nuclear stopping using Thomas-Fermi atoms suggested a reduced coordinate system for nuclear stopping. Their formalism was applied to TRIM simulations and a nuclear stopping cross-section as a function of a reduced energy unit

$$\varepsilon = \frac{a_u M_2 E_o}{Z_1 Z_2 e^2 \left(M_1 + M_2\right)} \qquad [2.16]$$

was defined:

$$S_n(\varepsilon) = \frac{\varepsilon}{\pi a_u^2 \gamma E_o} S_n(E).^{54} \qquad [2.17]$$

Equation [2.16] converts the nuclear stopping power to LSS reduced units.[133] The universal nuclear stopping is then calculated by redefining equation [2.15] in reduced LSS units with a reduced impact parameter of $b = \frac{p}{a_I}$:

$$S_n(\varepsilon) = \varepsilon \int_0^{\infty} \sin^2 \frac{\theta}{2} d(b^2). \qquad [2.18]$$

So, for practical calculations, the universal nuclear stopping cross section becomes

$$S_n(E_o) = \frac{8.462 \times 10^{-15} Z_1 Z_2 M_1 S_n(\varepsilon)}{(M_1 + M_2)(Z_1^{.23} + Z_2^{.23})} eV/(atom/cm^2), \qquad [2.19]$$

with reduced energy, ε, determined to be

$$\varepsilon = \frac{32.53 M_2 E_o}{Z_1 Z_2 (M_1 + M_2)(Z_1^{.23} + Z_2^{.23})} \qquad [2.20]$$

and the reduced nuclear stopping calculated at

$$S_n(\varepsilon) = \begin{pmatrix} \dfrac{\ln(1+1.1383\varepsilon)}{2\left[\varepsilon + .01321\varepsilon^{.21226} + .19593\varepsilon^{.5}\right]} & For, \varepsilon \leq 30 \\ \\ \dfrac{\ln(\varepsilon)}{2\varepsilon} & For, \varepsilon > 30 \end{pmatrix}. \quad [2.21]$$

For higher energies, nuclear stopping must become like Rutherford scattering. Therefore, for reduced energies above 30, a shift is devised to an unscreened nuclear stopping power.[133] It is necessary to understand the energetic transfer between ions and target atoms for nuclear interactions. Although electronic energy loss is higher than nuclear energy loss, the nuclear collisions yield lattice damage.[8]

The second component of energy loss to the ion along its trajectory through a target occurs upon interaction with the target electrons, referred to as the electronic stopping power or cross-section. The energy loss is related to the distance L:

$$L = \frac{0.02\left[1+(M_1/M_2)\right]^2}{4\pi a^2 N} \frac{\varepsilon^2 + 0.052\varepsilon^{1.32}}{\ln(1+\varepsilon)} \quad [2.22]$$

with $\varepsilon = \dfrac{E_C}{\left(Z_1 Z_2 e^2 / a\right)}$ [24], traveled between collisions by

$$\Delta E_e = LNS_e(E). \quad [2.23]$$

$S_e(E)$ is the electronic stopping cross section. At low energies $S_e(E)$ equals

$$S_L = kE^p, \quad [2.24]$$

where k is the velocity independent stopping parameter and $p = \dfrac{1}{2}$. The Lindhard-Scharff[134] formula for k in equation [2.24] is used.

$$k = k_L = \frac{1.212 Z_1^{7/6} Z_2}{(Z_1^{2/3} + Z_2^{2/3})^{3/2} M_1^{1/2}} eV^{1/2} \text{Å}^2 \quad [2.25]$$

For high, nonrelativistic energies, the Bethe-Bloch electronic stopping theories become valid and

$$S = \frac{8\pi Z_1^2 e^4}{I_o \varepsilon_B} \ln \varepsilon_B \qquad [2.26]$$

and

$$\varepsilon_B = \frac{2 m_e v^2}{Z_2 I_o}, \qquad [2.27]$$

where m_e is the electron mass and $Z_2 I_o$ is the mean excitation energy. The Bloch constant I_o [135] may be written as

$$I_o = \begin{pmatrix} 12 + 7Z_2^{-1}, & for, Z_2 < 13 \\ 9.76 + 58.5Z_2^{-1.19} & for, Z_2 \geq 13 \end{pmatrix}. \qquad [2.28]$$

To bridge the electronic stopping from the low to high energy regimes, an interpolation scheme developed by Biersack[80,81] reported in equation [2.29] is employed.

$$S_e = (S_L^{-1} + S_B^{-1})^{-1} \qquad [2.29]$$

S_L in equation [2.24] is used along with an expression for S_B, modified slightly from equation [2.26] to achieve an overall fit to experimental data within this transition region,

$$S_B = \frac{8\pi Z_1^2 e^4}{I_o \varepsilon_B} \ln(\varepsilon_B + 1 + \frac{C}{\varepsilon_B}), \qquad [2.30]$$

where $C = 5$ except for $Z_1 < 3$, $C = \frac{100 Z_1}{Z_2}$ to better fit experimental data.

This formalism is used in transport of ions in matter (TRIM)[24] simulations to generate implant profiles and resulting damage distributions due to those procedures. Modeling by TRIM produces accurate profiles to first order. TRIM is an athermal model,

recall, so no defect interactions are considered upon their production.

REFERENCES

1. G. Dearnaley, J. H. Freeman, R. S. Nelson, and J. Stephen, *Ion Implantation* (Amsterdam: North-Holland Publishing Company, 1973).

2. *Ion Implantation Science and Technology*, edited by J. F. Ziegler (Orlando: Academic Press, Inc., 1984).

3. E. Chason, S. T. Picraux, J. M. Poate, J. O. Borland, M. I. Current, T. Diaz de la Rubia, D. J. Eaglesham, O. W. Holland, M. E. Law, C. W. Magee, J. W. Mayer, J. Melngailis, and A. F. Tasch, *J. Appl. Phys.* **81**(10), 6513 (1997).

4. J. W. Mayer, L. Eriksson, and J. A. Davies, *Ion Implantation in Semiconductors* (New York: Academic, 1970).

5. C. S. Nichols, C. G. Van de Walle, and S. T. Pantelides, *Phys. Rev. B* **40**(8), 5484 (1989).

6. Ulrich M. Gösele and Teh Y. Tan, *November MRS Bulletin*, p. 42 (1991).

7. T. E. Seidel, Chapter 6 in *Ion Implantation in VLSI Technology*, edited by S. M. Sze (New York: McGraw-Hill Book Co., 1983), p. 219 and references within.

8. J. F. Gibbons, *Proc. IEEE* **60**, 1062 (1972).

9. J. F. Ziegler, "Ion Implantation Physics", in *Handbook of Ion Implanation Technology*, ed. J. F. Ziegler (The Netherlands: North-Holland, 1992).

10. H. J. Stein, F. L. Vook, D. K. Brice, J. A. Borders, and S. T. Picraux, *Radiat. Eff.* **6**, 19 (1970).

11. F. L. Vook and H. J. Stein, *Radiat. Eff.* **2**, 23 (1969).

12. Lewis T. Chadderton, *Radiat. Eff.* **8**, 77 (1971).

13. G. F. Cerofolini, L. Meda, and C. Volpones, *J. Appl. Phys.* **63**(10), 4911 (1988).

14. M. L. Swanson, J. R. Parsons, and C. W. Hoelke, *Radiat. Eff.* **9**, 249 (1971).

15. M. D. Matthews and S. J. Ashby, *Philos. Mag.* **27**, 1313 (1973).

16. James W. Corbett, James P. Karins, and Teh Y. Tan, *Nucl. Instr. and Meth.* **182/183**, 457 (1981).

17. T. Motooka, F. Kobayashi, P. Fons, T. Tokuyama, T. Suzuki, and N. Natsuaki, *Extended Abstracts of the 1991 International Conference on Solid State Devices and Materials*, Yokohama, p. 44 (1991).

18. Teruaki Motooka, *Phys. Rev.* B **49**(23), 16367 (1994).

19. O. W. Holland, Bent Nielsen, and J. D. Budai, *Mater. Res. Soc. Symp. Proc. 396* (Pittsburgh, PA: Mater. Res. Soc., 1996), p. 15.

20. O. W. Holland, Ling Xie, Bent Nielsen, and D. S. Zhou, *J. Electron. Mater.* **25**, 99 (1996).

21. D. J. Eaglesham, T. E. Haynes, H.-J. Gossmann, D. C. Jacobson, P. A. Stolk, and J. M. Poate, *Appl. Phys. Lett.* **70**(24), 3281 (1997).

22. E. G. Roth, O. W. Holland, and D. K. Thomas, *Appl. Phys. Lett.* **74**(5), 679 (1999).

23. M. D. Giles, *J. Electrochem. Soc.* **138**, 1160 (1991).

24. J. Biersack and L. Haggmark, *Nucl. Instr. and Meth.* **174**, 257 (1980).

25. O. W. Holland, D. S. Zhou, and D. K. Thomas, *Appl. Phys. Lett.* **63**(7), 896 (1993).

26. O. W. Holland, J. D. Budai, and Bent Nielsen, *Mat. Sci. and Eng.* A**253**, 240 (1998).

27. O. W. Holland, D. Fathy, J. Narayan, and O. S. Oen, *Radiat. Eff.* **90**, 127 (1985).

28. Zhong-lie Wang, Bo-xu Zhang, Qing-tai Zhao, Qi Li, J. R. Liefting, R. J. Schreutelkamp, and F. W. Saris, *J. Appl. Phys.* **71**(8), 3780 (1992).

29. Wei-Kan Chu, James W. Mayer, and Marc-A Nicolet, *Backscattering Spectrometry* (New York: Academic Press, 1978).

30. O. W. Holland and E. G. Roth, "Damage Measurement" in *Materials and Process Charaterization of Ion Implantation*, edited by Michael I. Current and C. B. Yarling (Texas: Ion Beam Press, 1997), p. 262.

31. Charles Evans and Associates, 301 Chesapeake Drive, Redwood City, CA 94063. Phone: (415) 369-4567. Fax: (415) 369-7921.

32. P. M. Fahey, P. B. Griffin, and J. D. Plummer, *Rev. Mod. Phys.* **61**(2), 289 (1989).

33. G. D. Watkins, in *Radiation Damage in Semiconductors* (Paris, 1964), p. 97.

34. Peter J. Schultz and K. G. Lynn, *Rev. Mod. Phys.* **60**(3), 701 (1988).

35. M. Fujinami, *Phys. Rev.* B**53**, 13047 (1996).

36. E. Rutherford, *Phil. Mag.* **21**, 212 (1911); ibid, 21, 699 (1911).

37. J. J. Thomson, *Phil. Mag.* **6-23**, 449 (1912).

38. N. Bohr, *Phil. Mag.* **25**, 10 (1913).

39. H. A. Bethe, *Ann. Physik* **5**, 325 (1930).

40. H. A. Bethe, *Z. f. Physik* **76**, 293 (1932).

41. H. A. Bethe and W. Heitler, *Proc. Roy. Soc.* A**146**, 83 (1934).

42. F. Bloch, *Ann. Physik* **16**, 287 (1933).

43. F. Bloch, *Z. f. Physik* **81**, 363 (1933).

44. Claude Cohen-Tannoudji, Bernard Diu, and Franck Laloë, *Quantum Mechanics Volume One*, (Toronto: John Wiley & Sons, 1977).

45. N. Bohr, *Phys. Rev.* **58**, 654 (1940).

46. N. Bohr, *Phys. Rev.* **59**, 270 (1941).

47. W. F. G. Swann, *J. Frank. Inst.* **226**, 598 (1938).

48. J. Knipp and E. Teller, *Phys. Rev.* **59**, 659 (1941).

49. W. E. Lamb, *Phys. Rev.* **58**, 696 (1940).

50. E. Fermi and E. Teller, *Phys. Rev.* **72**, 399 (1947).

51. J. Lindhard, *Mat. Fys. Medd. Dan. Vid. Selsk.* **28**, No. 8 (1954).

52. J. Neufeld and R. H. Ritchie, *Phys. Rev.* **98**, 1632 (1955).

53. U. Fano, *Phys. Rev.* **103**, 1202 (1956).

54. J. F. Ziegler, "Ion Implantation Physics", in *Handbook of Ion Implanation Technology*, ed. J. F. Ziegler (The Netherlands: North-Holland, 1992), p. 1.

55. N. Bohr, *Mat. Fys. Medd. Dan. Vid. Selsk.* **18**(8), (1948).

56. O. B. Firsov, *Zh. EKsp. Teor. Fiz.* **34**, 447 (1958).

57. O. B. Firsov, *JETP* **7**, 308 (1958).

58. L. C. Northcliffe, *Phys. Rev.* **120**, 1744 (1960).

59. J. Lindhard, M. Scharff, and H. E. Schiott, *Mat. Fys. Medd. Dan. Vid. Selsk.* **33**, No. 14 (1963).

60. C. C. Rousseau, W. K. Chu, and D. Powers, *Phys. Rev.* A**4**, 1066 (1970).

61. W. D. Wilson, L. G. Haggmark, and J. P. Biersack, *Phys. Rev.* **15**B, 2458 (1977).

62. W. Brandt and M. Kitagawa, *Phys. Rev.* **25**B, 5631 (1982).

63. M. T. Robinson and O. S. Oen, *Appl. Phys. Lett.* **2**, 30 (1963).

64. K. Guttner, H. Ewald, and H. Schmidt, *Radiat. Eff.* **13**, 111 (1972).

65. M. T. Robinson and I. M. Torrens, *Phys. Rev.* B**9**, 5008 (1974).

66. S. J. Morris, . Obradovic, S.-H. Yang, and A. F. Tasch, *IEDM Technical Digest*, (1996).

67. M. Posselt, *Radiat. Eff. and Defects in Solids* **130-131**, 87 (1994).

68. I. Chakarov and R. Webb, *Radiat. Eff. and Defects in Solids* **130-131**, 447 (1994).

69. B. J. Mulvaney, W. B. Richardson, and T. L. Crandle, *IEEE Transact. on Computer-Aided Design* **8**(4), 336 (1998).

70. H. Glawischnig, "Process Simulation and Ion Implantation", in *Handbook of Ion Implanation Technology*, ed. J. F. Ziegler (The Netherlands: North-Holland, 1992), p. 226.

71. J. F. Ziegler, "Ion Implantation Physics", in *Handbook of Ion Implanation Technology*, ed. J. F. Ziegler (The Netherlands: North-Holland, 1992), p. 44.

72. P. Loftager, F. Besenbacher, O. S. Jensen, and V. S. Sorensen, *Phys. Rev.* A**20**, 1443 (1979).

73. J. P. Biersack and P. Mertens, "Charge States and Dynamic Screening of Swift Ions in Solids", p. 131, *Oak Ridge Rpt. No. CONF-820131*, Oak Ridge (1983).

74. W. N. Lennard, H. R. Andrews, I. V. Mitchell, D. Phillips, and D. Ward, ibid, p. 136 (1983).

75. A. Sommerfeld, *Z.f. Physik* **78**, 283 (1932).

76. G. Moliere, *Z. Naturforschung* A**2**, 133 (1947).

77. W. Lenz, *Z.f. Physik* **77**, 713 (1932).; H. Jensen, *Z.f. Physik* **77**, 722 (1932).

78. J. F. Ziegler, J. P. Biersack, U. Littmark, "The Stopping and Range of Ions in Solids", Vol. **1** (New York: Pergamon Press, 1984).

79. O. B. Firsov, *Zh. EKsp. Teor. Fiz.* **33**, 696 (1957) [*Sov. Phys.-JETP* **6**, 534 (1958)].

80. J. P. Biersack and D. Fink, in *Ion Implantation in Semiconductors*, ed. S. Namba (New York: Plenum Press, 1974), p. 211.

81. J. P. Biersack and D. Fink, in *Atomic Collisions in Solids*, Vol. **2** (New York: Plenum Press, 1975), p. 737.

82. James F. Ziegler, *Nucl. Instr. And Meth.* B**219/220**, 1027 (2004).

83. A. M. Stoneham, *Radiat. Eff.* **9**, 165 (1971); E. Bogh, *Can. J. of Phys.* **46**, 653 (1968); J. W. Corbett and J. C. Bourgoin, *Radiat. Eff.* **30**, 255 (1976); and L. Csepregi, E. F. Kennedy, S. S. Lau, J. W. Mayer, and T. W. Sigmon, *Appl. Phys. Lett.* **29**(10), 645 (1976).

84. G. H. Kinchin and R. S. Pease, *Rep. Prog. Phys.* **18**, 1 (1955).

85. P. Sigmund, *Radiat. Eff.* **1**, 15 (1969).

86. M. J. Norgett, M. T. Robinson, and I. M. Torrens, *Nucl. Eng. Design* **33**, 50 (1974).

87. Donald R. Olander, *Fundamental Aspects of Nuclear Reactor Fuel Elements* (Oak Ridge: ERDA Technical Information Center, 1976), p. 374.

88. D. J. Eaglesham, P. A. Stolk, H.-J. Gossmann, T. E. Haynes and J. M. Poate, *Nucl. Inst. and Meth.* B**106**, 191 (1995).

89. O. W. Holland, C. W. White, M. K. El-Ghor, and J. D. Budai, *J. Appl. Phys.* **68**, 2081 (1990).

90. F. F. Morehead, Jr. and B. L. Crowder, *Radiat. Eff.* **6**, 27 (1970).

91. O. W. Holland, M. K. El-Ghor, and C. W. White, *Appl. Phys. Lett.* **53**(14), 1282 (1988).

92. L. Csepregi, E. F. Kennedy, T. J. Gallagher, J. W. Mayer, and T. W. Sigmon, J. *Appl. Phys.* **48**, 4234 (1977).

93. J. A. Lambert and P. S. Dobson, *Philos. Mag.* A**44**, 1043 (1981).

94. K. S. Jones, S. Prussin, and E. R. Weber, *Appl. Phys.* A **45**, 1 (1988).

95. V. C. Venezia, D. J. Eaglesham, T. E. Haynes, Aditya Agarwal, D. C. Jacobson, H.-J. Gossman, and F. H. Baumann, *Appl. Phys. Lett.* **73**, 2980 (1998).

96. V. Raineri, R. J. Schreutelkamp, F. W. Saris, K. T. F. Janssen, and R. E. Kaim, *Appl. Phys. Lett.* **58**(9), 922 (1991).

97. Bent Nielsen, O. W. Holland, T. C. Leung, and K. G. Lynn, *J. Appl. Phys.* **74**(3), 1636 (1993).

98. O. W. Holland and C. W. White, *Nucl. Inst. and Meth.* B**59/60**, 353 (1991).

99. O. W. Holland, T. P. Sjoreen, D. Fathy, and J. Narayan, *Appl. Phys. Lett.* **45**(10), 1081 (1984).

100. J. F. Ziegler, Nucl. Instr.and Meth. B**6**, 270 (1985).

101. Qing-tai Zhao, Zhong-lie Wang, Tian-bing Xu, Pei-ran Zhu, and Jun-si Zhou, *Appl. Phys. Lett.* **62**(24), 3183 (1993); Qing-tai Zhao, Zhong-lie Wang, Tian-bing Xu, Pei-ran Zhu, and Jun-si Zhou, *Appl. Phys. Lett.* **64**(2), 175 (1994).

102. Zhong-lie Wang, Qing-tai Zhao, Ke-Ming Wang, and Bo-Rong Shi, *Nucl. Instr. and Meth.* B**115**(1-4), 421 (1996).

103. D. Venables, K. S. Jones, and F. Namavar, *Appl. Phys. Lett.* **60**(25), 3147 (1992).

104. S. M. Hu, *J. Appl. Phys.* **45**, 1567 (1974).

105. D. J. Eaglesham, P. A. Stolk, H.-J. Gossmann and J. M. Poate, *Appl. Phys. Lett.* **65**(18), 2305 (1994).

106. L. H. Zhang, K. S. Jones, P. H. Chi, and D. S. Simons, *Appl. Phys. Lett.* **67**(14), 2025 (1995).

107. H. S. Chao, P. B. Griffin, and J. D. Plummer, *Appl. Phys. Lett.* **68**, 3570 (1996).

108. E. G. Roth, O. W. Holland, V. C. Venezia, and Bent Nielsen, *J. Electon. Mater.* **26**(11), 1349 (1997).

109. K. S. Jones, R. G. Elliman, M. M. Petravic, and P. Kringhøj, *Appl. Phys. Lett.* **68**, 3111 (1996).

110. A. E. Michel, R. H. Kastl, S. R. Mader, B. J. Masters, and J. A. Gardner, *Appl. Phys. Lett.* **44**, 404 (1984).

111. B. L. Crowder, J. F. Ziegler, and G. W. Cole, *Ion Implantation in Semiconductors and Other Materials* (New York: Plenum Press, 1973), p. 257.

112. O. W. Holland and J. Narayan, *Nucl. Instr. and Meth.* B**40/41**, 537 (1989).

113. P. A. Stolk, H.-J. Gossmann, D. J. Eaglesham, D. C. Jacobson, J. M. Poate, and H. S. Luftman, *Appl. Phys. Lett.* **66**, 568 (1995).

114. T. E. Haynes, D. J. Eaglesham, P. A. Stolk, H.-J. Gossmann, D. C. Jacobson, and J. M. Poate, *Appl. Phys. Lett.* **69**, 1376 (1996).

115. O. W. Holland, *Appl. Phys. Lett.* **54**, 798 (1989).

116. L. Pelaz, M. Jaraiz, G. H. Gilmer, H.-J. Gossmann, C. S. Rafferty, D. J. Eaglesham, and J. M. Poate, *Appl. Phys. Lett.* **70**(17), 2285 (1997).

117. J. Narayan, O. W. Holland, and B. R. Appleton, *J. Vac. Sci. Technol.* B**1**(4), 871 (1983).

118. S. Solmi, R. Angelucci, F. Cembali, M. Servidori, and M. Anderle, *Appl. Phys. Lett.* **51**, 331 (1987).

119. S. J. Pennycook, J. Narayan, and O. W. Holland, *J. Appl. Phys.* **55**, 837 (1984).

120. S. J. Pennycook, J. Narayan, and O. W. Holland, *J. Cryst. Growth* **70**, 597 (1984).

121. Craig R. Barrett, William D. Nix, and Alan S. Tetelman, *The Principles of Engineering Materials* (Englewood Cliffs, NJ: Prentice-Hall, Inc., 1973), p. 260.

122. E. P. EerNisse, *Ion Implantation in Semiconductors and Other Materials*, ed. B. L. Crowder (New York: Plenum Press, 1973), p. 531.

123. S. Peterström and B. G. Svensson, *J. Appl. Phys.* **68**, 3570 (1996).

124. T. O. Sedgwick, A. E. Michel, V. R. Deline, S. A. Cohen, and J. B. Lasky, *J. Appl. Phys.* **63**, 1452 (1988).

125. J. Amano, *Radiat. Eff.* **61**, 195 (1982); I. Golecki, H. L. Glass, and G. Kinoshita, *Appl. Phys. Lett.* **40**(8), 670 (1982); and S. S. Lau, S. Matteson, J. W. Mayer, P. Revesz, J. Gyulai, J. Roth, T. W. Sigmon, and T. Cass, *Appl. Phys. Lett.* **34**(1), 76 (1979).

126. O. W. Holland, D. Fathy, T. P. Sjoreen, J. Narayan, and K. More, in *Advanced Applications of Ion Implantation 1985*, SPIE-The International Society for Optical Engineering, Bellingham, WA, 1985, edited by M. I. Current and D. K. Sadana, 530, 255 (1985).

127. John R. Dennis and Edward B. Hale, *J. Appl. Phys.* **49**(3), 1119 (1978).

128. J. C. C. Tsai, in *VLSI Technology*, edited by S. M. Sze (New York: McGraw-Hill, 1983), pp. 193-194.

129. E. G. Roth, O. W. Holland, and A. Meldrum, in *Silicon Materials Science and Technology 1998*, Proceedings of the Eighth International Symposium on Silicon Materials Science and Technology, PV 98-1, edited by H. R. Huff, H. Tsuya, and U. Gösele (NJ: Pennington, 1998), p. 938.

130. Jun Xu, A. P. Mills, Jr., Ryoichi Suzuki, E. G. Roth, and O. W. Holland, *Appl. Surf. Sci.* **149**, 193 (1999).

131. Jun Xu, E. G. Roth, O. W. Holland, A. P. Mills, Jr., and Ryoichi Suzuki, *Appl. Phys. Lett.* **74**(7), 997 (1999).

132. J. L. Hastings, S. K. Estreicher, and P. A. Fedders, *Phys. Rev.* B**56**, 10215 (1997).

133. J. F. Ziegler, "Ion Implantation Physics", in *Handbook of Ion Implanation Technology*, ed. J. F. Ziegler (The Netherlands: North-Holland, 1992), p. 41.

134. J. Lindhard and M. Scharff, *Phys. Rev.* **124**, 128 (1961).

135. W. H. Barkas and M. J. Berger, Studies in penetration of charged particles in matter, NAS-NRC Publication 1133, *Nuclear Science Series Report* **39**, 103 (1964); R. M. Sternheimer, *Phys. Rev.* **145**, 247 (1966).

136. J. Lindhard, V. Nielsen, and M. Scharff, *Mat. Fys. Medd. Dan. Vid. Selsk.* Vol. **36**.